Technical Physics Letters, Vol. 28, No. 2, 2002, pp. 102–104. Translated from Pis'ma v Zhurnal Tekhnicheskoĭ Fiziki, Vol. 28, No. 3, 2002, pp. 42–48.

A Few-Mode Optical Fiber Retaining Optical Vortices

A. V. Volyar and T. A. Fadeeva

Tauric National University, Simferopol, Crimea, Ukraine

Received June 29, 2001

Abstract—The ability of an optical fiber with axial losses to selectively suppress the fundamental HE_{11} mode, as well as the *TE* and *TM* waveguide modes, and, simultaneously, to transmit optical vortices with almost zero energy losses is considered. The attenuation coefficients for the corresponding eigenmodes and vortices are determined. It is shown that such a fiber operates as a mode filter for the feeding beam. © *2002 MAIK "Nauka/Interperiodica".*

Unique properties of the optical vortices representing a special form of the optical field have been studied in many recent works [1, 2]. The ability of optical vortices to capture microparticles and to transfer angular momentum to these objects is not only of great importance in basic science but also enables the development of a special class of devices for microelectronics and genetic engineering [3]. Moreover, guided optical vortices in a few-mode fiber gain new properties not typical of the free-space vortices and similar to those of a mechanical gyroscope [4]. This, in turn, allows utilizing these structures in single-pass fiber gyroscopes and thus abandoning complex ring interferometric schemes introducing substantial errors in the measurement procedure.

At the same time, it is well known that small external perturbations of a few-mode fiber cause the transfer of a part of the energy of guided vortices existing in this fiber [the so-called *CV* vortices representing a linear combination of an even (e) and odd (o) hybrid mode: $CV \Rightarrow HE_{21}^{(e)} \pm iHE_{21}^{(o)}$] to other guided modes [5]. In particular, the energy is most efficiently transferred to the *IV* vortex (a linear combination of the transverse electric and a transverse magnetic modes: $IV \Rightarrow TE_{01} \pm iTM_{01}$) and to the fundamental HE_{11} mode. It should be noted that, since the *CV* vortex and the TE_{01} and TM_{01} modes have identical cutoff frequencies [6], it is extremely difficult to excite an isolated *CV* vortex in a fiber. Obviously, developing sensors of physical parameters based on the properties of guided optical vortices is inseparably linked with developing few-mode optical fibers capable of transmitting an isolated guided optical vortex.

The purpose of this work was to study the properties of optical fibers capable of selectively suppressing both the instable *IV* vortex and the fundamental HE_{11} mode, while transmitting the *CV* vortex with almost zero losses.

First of all, let us consider the fact that transverse components of the wave function of the fundamental HE_{11} mode exhibit extrema at the optical axis [6], whereas similar components of the *CV* and *IV* vortices vanish at this axis. On the other hand, the longitudinal field component of the *CV* vortex also vanishes at the axis, whereas magnitudes of the *z* components of the magnetic field of the *TE* mode and the electric field of the *TM* mode are maximal.

Let the paraxial region of the fiber be lossy along the whole length, which causes absorption of the energy of guided modes. Assume also that there is no birefringence caused by anisotropic properties of the fiber material or by deformations of the fiber cross section. Then we may use the reciprocity theorem for fields in an optical fiber [6].

1. First, we estimate the attenuation coefficients of the fiber eigenmodes. To do this, we write the wave equation for transverse components of the electric field $\mathbf{e}_t$ in a lossless fiber with axisymmetric distribution of refractive index $n(r)$ [6] assuming that the fiber is weakly guiding. Neglecting the right-hand side of the wave equation, we obtain

$$(\nabla_t^2 + k^2\tilde{n}^2(r) - \tilde{\beta}^2)\tilde{\mathbf{e}}_t = 0, \qquad (1)$$

where $\tilde{\beta}$ is the mode propagation constant, ∇_t^2 is the transverse Laplacian, and k is the wave number. If the fiber is lossy, the refractive index is a complex quantity: $n^2(r) = n_R^2(r) + in_I^2(r)$, where n_R and n_I are real quantities. Moreover, the mode propagation constant also becomes complex: $\beta = \beta_R + i\beta_I$. As a result, the wave equation for a lossy fiber takes the form

$$(\nabla_t^2 + k^2n^2(r) - \beta^2)\mathbf{e}_t = 0. \qquad (2)$$

Now let us calculate dot products of Eq. (1) and $\mathbf{e}_t^*$ (the asterisk designates the complex conjugate) and the complex conjugate of Eq. (2) and vector $\tilde{\mathbf{e}}_t$. Next, we integrate the difference of the dot products over an infinite area S of the fiber cross section. In so doing,

we take into account that $\int_S (\mathbf{e}_t^* \nabla_t^2 \tilde{\mathbf{e}}_t - \tilde{\mathbf{e}}_t \nabla_t^2 \mathbf{e}_t^*) dS = \oint_L (\mathbf{e}_t^* \nabla_t \tilde{\mathbf{e}}_t - \tilde{\mathbf{e}}_t \nabla_t \mathbf{e}_t^*) dl = 0$ due to finite values of the fields and their first derivatives at infinity. After separating the real and imaginary parts, we obtain

$$\beta_I \approx \frac{k^2}{2\tilde{\beta}} \frac{\int_S n_I^2(r) |\tilde{\mathbf{e}}_t|^2 dS}{\int_S |\tilde{\mathbf{e}}_t|^2 dS}. \quad (3)$$

Deriving expression (3), we assumed that $n_R \gg n_I$, $\tilde{n} \approx n_R$, and $\tilde{\mathbf{e}}_t \approx \boldsymbol{e}_t$, which is quite reasonable in view of small losses.

Estimate the obtained expression for the fiber with a parabolic index profile: $n^2 = n_0^2(1 - 2\nabla R^2)$, where $R = r/\rho$, ρ is the characteristic radius of the fiber, and Δ is the height of the refractive index profile. Then the absolute value of the wave function of the optical vortex can be written in the following form [7]: $|\tilde{\mathbf{e}}| = F_l = R^l \exp(-1/2VR^2)$, where V is the waveguide parameter. Let the imaginary part of the refractive index be given by the formula $n_I^2 = n_{0I}^2 \exp(-\alpha R^2)$, where α describes the steepness of the absorption profile. Then expression (3) can be written as

$$\beta_I^{(l)} \approx n_{0I} \frac{k}{2n_0} \left(\frac{V}{V + \alpha} \right)^{l+1}. \quad (4)$$

From this it follows that the greater the topological charge l of an optical vortex, the smaller the attenuation of the vortex in the fiber. The fundamental HE_{11} mode with $l = 0$ exhibits the greatest losses.

Figure 1 presents the ratios of the absorption coefficients $\beta_I^{(l)}/\beta_I^{(0)}$ of an optical vortex with the topological charge l and the fundamental HE_{11} mode. For example, if the loss of an optical vortex with $l = 1$ is 2 dB/km and the steepness α of the absorption profile is 3×10^4, the loss of fundamental mode amounts to 6×10^4 dB/km.

Thus, the losses introduced into the fiber core so as to be concentrated near the optical axis cause a selective absorption of the energy of the fundamental HE_{11} mode, while virtually not affecting the energy of the optical vortex. However, expression (3) shows that both the *CV* vortex and the *TE* and *TM* modes exhibit equal losses, which is generally not true. Evidently, the method used to derive expression (3) cannot solve the problem. The matter is that, in the above calculations, we assumed that the fiber is a weakly guiding structure and neglected the longitudinal field components responsible for the absorption of *TE* and *TM* modes. In order to take into account this effect, we should return to the original equations.

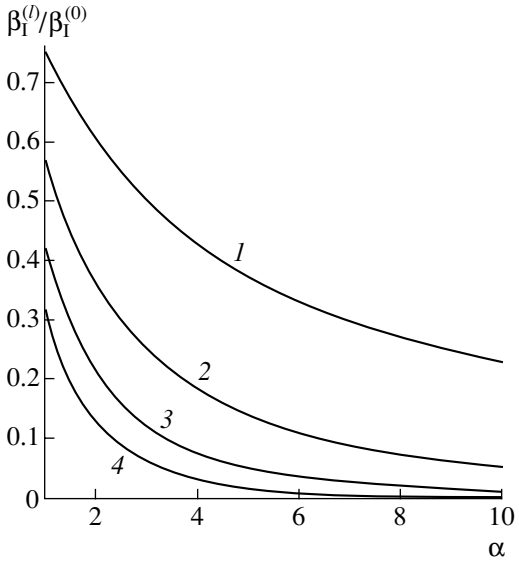

Fig. 1. The ratios of the imaginary parts of the propagation constants of the optical vortex and the fundamental HE_{11} mode $\beta_I^{(l)}/\beta_I^{(O)}$ versus the coefficient α appearing in the imaginary part of the index profile n_I^2: $l = 1$ (*1*), 2 (*2*), 3 (*3*), and 4 (*4*).

2. The translational invariance of the fields existing in an optical fiber allows us to write independent equations for the longitudinal and transverse field components [6]. In particular,

$$\{\nabla_t^2 + k^2 n^2(r) - \beta^2\} e_z = -i\beta \mathbf{e}_t \nabla_t \ln n^2(r),$$

$$\{\nabla_t^2 + k^2 n^2(r) - \beta^2\} h_z = (\nabla_t h_z - i\beta \mathbf{h}_t) \nabla_t \ln n^2(r).$$

For a weakly guiding fiber, we can neglect the right-hand sides of these equations. Then we immediately arrive at Eq. (2) with $\mathbf{e}_t$ replaced with either e_z or h_z. In addition, we should remember that, in this case, ∇_t^2 is a scalar operator. Then, after transformations described in Section 1, equations for e_z (the *TM* mode) and h_z (the *TE* mode) give the following expression for the imaginary part of the propagation constant:

$$\beta_I^{\begin{Bmatrix} TM \\ TE \end{Bmatrix}} \approx \frac{k^2}{2\tilde{\beta}} \int_S n_I^2(r) \begin{Bmatrix} |\tilde{e}_z|^2 \\ |\tilde{h}_z|^2 \end{Bmatrix} dS \Big/ \int_S \begin{Bmatrix} |\tilde{e}_z|^2 \\ |\tilde{h}_z|^2 \end{Bmatrix} dS. \quad (5)$$

The profiles of the longitudinal components of the *TE* and *TM* modes are specified by the formula $G_1 = \frac{dF_1}{dR} + \frac{1}{R} F_1 = (1 - VR^2) \exp\left(-\frac{1}{2} VR^2\right)$. Substituting this expression into (5), we obtain the relationship

$$\beta_I^{(TE)} = \beta_I^{(TM)} \approx n_{01} \frac{k}{2n_0} \left(\frac{V}{V + \alpha} \right), \quad (6)$$

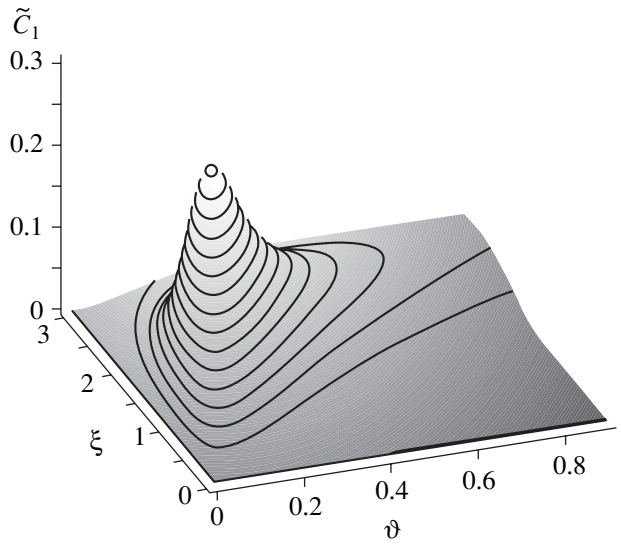

Fig. 2. The normalized excitation coefficient $\tilde{C}_1$ of an optical vortex with $l = 1$ versus the angle of incidence ϑ of the feeding beam and the ratio ξ of the radii of the feeding beam and the guided vortex.

which formally coincides with expression (4) for $l = 0$. Consequently, the HE_{11}, *TE*, and *TM* modes exhibit equal losses substantially exceeding those of the *CV* vortices.

The results obtained indicate that, irrespective of the way of excitation of an optical fiber with axial energy losses, the major part of the output energy will be concentrated in a guided optical vortex.

3. Let us estimate the efficiency of excitation of the *CV* vortices in a parabolic fiber fed with a right-hand circularly polarized fundamental Gaussian beam whose axis makes an angle ϑ with the fiber axis. We will use the power excitation coefficients for the fiber modes [6]:

$$C_l = \frac{\rho^2 n_0}{2\pi}\sqrt{\frac{\varepsilon_0}{\mu_0}} \times \left|\int_0^{2\pi} d\varphi \int_0^{\infty} \Psi_x^{(in)} F_l(R)\exp(\pm il\varphi) R dR\right|^2 \Big/ \int_0^{\infty} F_t^2(R) R dR, \quad (7)$$

where $\Psi_x^{(in)} = \exp\left(-\frac{r^2}{w^2}\right)\exp(ik\vartheta\sin\varphi)$ is the x-component of the fundamental Gaussian beam at the waist $z = 0$ and w is the waist radius. Due to a small angle of incidence, the x- and y-components will be excited with equal efficiencies; therefore, it would suffice to estimate only one of these components. For the *CV* vortices, we obtain the following expression:

$$\tilde{C}_l = \frac{4}{l!}(kn_0 w\vartheta)^{2l}\left[\frac{\xi}{1+\xi^2}\right]^{2(l+1)}\exp\left\{-\frac{(kw\xi\vartheta)^2}{1+\xi^2}\right\}, \quad (8)$$

where $\tilde{C}_l$ is the C_l value normalized to the power of the incident beam, $\xi = \tilde{\rho}/w$, and $\tilde{\rho} = \rho/V$. Figure 2 shows the coefficients $\tilde{C}_l$ as functions of the excitation angle ϑ and the ratio ξ of the mode radius (for a *CV* vortex with unit topological charge $l = 1$) to the beam radius. The curves exhibit maxima at matched values of the mode and beam radii ($\xi = 1$) for an optimum angle $\vartheta^{(opt)} = \sqrt{1+\xi^2}/(kw\xi)$. In calculations, we took into account that the Gaussian beam arrives from the medium with $n = 1$ and assumed that $V = 4$. For these values, the optimum excitation coefficient $\tilde{C}_1^{(opt)} \approx 0.3$. It should be noted that the Gaussian beam excites vortices with $l = +1$ and -1 with equal efficiency. However, the vortex with the right-hand circular polarization and a negative topological charge is an instable *IV* vortex which decays during propagation. Hence, the optimum excitation coefficient is half as small: $\tilde{C}_1^{(opt)} \approx 0.15$.

Thus, an optical fiber with axial losses not only can retain a guided optical vortex but also operates as a mode filter for the exciting field.

Acknowledgments. The authors are grateful to K.N. Alekseev for fruitful discussion.

REFERENCES

1. J. F. Nay, *Natural Focusing and Fine Structure of Light. Caustics and Wave Dislocations* (Inst. of Physics Publ., Bristol, 1999).
2. M. S. Soskin and M. V. Vasnetsov, *Horizons in World Physics*, Ed. by M. Vasnetsov and K. Staliunas (1999), Vol. 228, pp. 1–35.
3. L. Allen, M. J. Padget, and M. Babiker, Prog. Opt. **39**, 291 (1999).
4. A. V. Volyar, T. A. Fadeyeva, and V. G. Shvedov, Proc. SPIE **4403**, 155 (2000).
5. A. V. Volyar and T. A. Fadeeva, Opt. Spektrosk. **85** (2), 295 (1998) [Opt. Spectrosc. **85**, 272 (1998)].
6. A. W. Snyder and J. D. Love, *Optical Waveguide Theory* (Chapman and Hall, London, 1983; Radio i Svyaz', Moscow, 1987).
7. A. V. Volyar, V. Z. Zhilaĭtis, and V. G. Shvedov, Pis'ma Zh. Tekh. Fiz. **24** (20), 87 (1998) [Tech. Phys. Lett. **24**, 826 (1998)].

Translated by A. Kondrat'ev

Technical Physics Letters, Vol. 28, No. 2, 2002, pp. 105–107. Translated from Pis'ma v Zhurnal Tekhnicheskoĭ Fiziki, Vol. 28, No. 3, 2002, pp. 49–53.

The Ultrasonic Wave Damping in the Region of a Magnetic Phase Transition in Manganese–Zinc Spinels

L. N. Kotov[a,*] and S. N. Karpachev[b]

[a] *Syktyvkar State University, Syktyvkar, Komi Republic, Russia*

** e-mail: kotov@ssu.komi.com*

[b] *Moscow State University, Moscow, Russia*

Received July 5, 2001

Abstract—Data on the damping of ultrasonic waves in the vicinity of the point of inversion of the first anisotropy constant are reported for manganese–zinc spinel crystals grown by various methods. A low-frequency maximum in the ultrasonic wave damping caused by the magnetoelastic interaction in the region of a magnetic phase transition in the spinel is observed for the first time. A difference in the acoustic properties of crystals of various types observed in the region of the phase transition is explained by the difference of internal fields related to differences in the degree of macroscopic disorder and in the arrangement of Fe^{2+} and Fe^{3+} ions in the spinel crystal lattice. © *2002 MAIK "Nauka/Interperiodica".*

Magnetic phase transitions are usually accompanied by anomalies in the acoustic properties of crystals [1–2]. In particular, the spin-reorientation phase transitions (SRPTs) lead to a change in shape of the magnon-phonon spectra, which is determined by the efficiency of the magnetoelastic coupling and by the magnetization relaxation parameter [2].

The cubic crystals of a nonstoichiometric manganeze-zinc spinel $Mn_aZn_bFe_{2+c}O_4$ ($a + b + c = 1$) are characterized by the existence of a temperature interval in which the first magnetic anisotropy constant K_1 changes sign while the second constant K_2 remains negative, which is manifested by a change in the easy magnetization direction from [100] to [111] with decreasing temperature [3]. The transitions from one magnetic phase to another must be first-order phase transitions possessing a jumplike character. However, the presence of a domain structure results in that the SRPT, involving the growth of a new phase from the domain walls, is smeared in a certain temperature interval $\Delta T = T_r' - T_r''$. Featuring a transition domain structure, two magnetic phases with the easy axes oriented in the [100] and [111] directions (below, [100]- and [111]-phases, respectively) coexist in the interval between T_r' and T_r''.

It was previously established that the manganeze-zinc spinel crystals grown by the Verneuil method (type A samples) exhibit a sharp increase in the damping of longitudinal ultrasonic waves in the frequency interval from 15 to 40 MHz [1], while the crystals of a close composition grown by the Bridgman method (type B samples) showed a much less pronounced peak of damping, which was sometimes observed only after a high-temperature annealing [4]. For this reason, it was concluded [4] that no SRPTs take place in the unannealed spinel crystals of type B.

In order to explain this behavior of the ultrasonic wave damping, we have studied the manganeze-zinc spinel crystals of types A and B in the 2.5–40 MHz frequency range at temperatures from 100 to 350 K in the absence of an external constant magnetic field. The crystal samples had a cubic shape with an edge length of 1 cm. The experiments were performed by a standard method [3] employing pulsed excitation and measurement of the ultrasonic wave amplitude in the samples.

Figure 1 shows the temperature variation of the damping coefficient $\alpha(T)$ measured at various frequencies of the longitudinal ultrasonic waves propagating in a crystal of the A type (sample composition: $a = 0.57$, $b = 0.37$, $c = 0.06$; saturation magnetization, $M_s = 318$ G). For this crystal, the damping exhibited a jump with decreasing temperature at all frequencies. The jump amplitude decreases when the cyclic frequency of the wave ω_a deviates from the intrinsic ferromagnetic resonance frequency $\omega_0 \approx \gamma H_{in}$, where γ is the gyromagnetic ratio and H_{in} is the internal magnetic field strength (representing a sum of the anisotropic and demagnetizing fields at the domain walls). At very low frequencies, the conditions $\omega_a < \omega_0$ and $\omega_r < \omega_a$ (ω_r is the magnetization relaxation frequency) are obeyed on both sides of the transition region. In this case, the oscillations

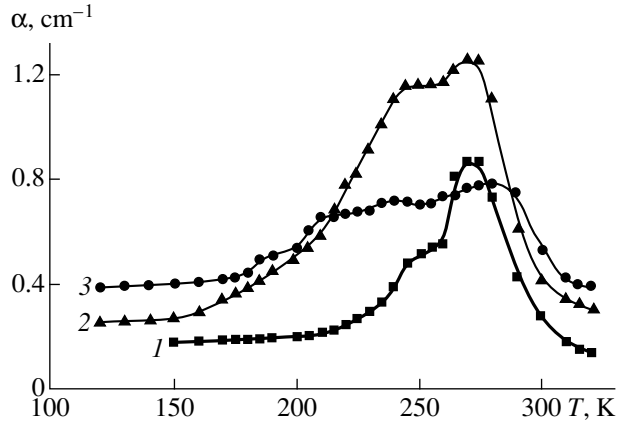

Fig. 1. The temperature variation of the damping coefficient $\alpha(T)$ for the longitudinal ultrasonic waves of various frequencies f = 6 (*1*), 22 (*2*), and 39 MHz (*3*) propagating in the [100] direction in a manganese–zinc spinel crystal of type A.

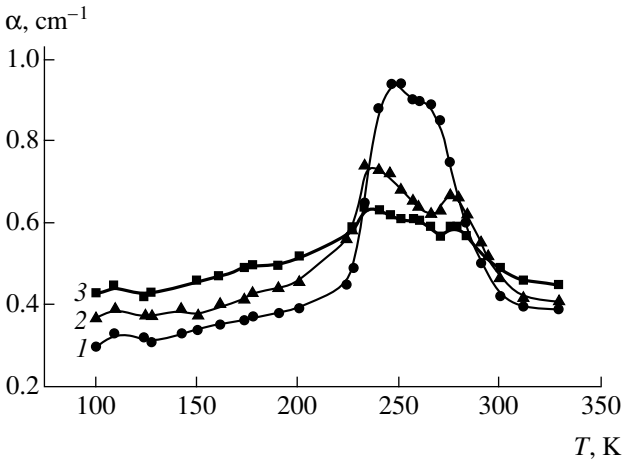

Fig. 2. The temperature variation of the damping coefficient $\alpha(T)$ for the longitudinal ultrasonic waves of various frequencies f = 2.5 (*1*), 5 (*2*), and 11 MHz (*3*) propagating in the [111] direction in a manganese–zinc spinel crystal of type B.

belong to a weakly decaying branch of the magnetoelastic wave spectrum [2]. As the ultrasonic wave frequency increases, the above relationships change to $\omega_a \geq \omega_0$ and $\omega_a < \omega_r$ and the magnetoelastic oscillations acquire a relaxation character leading to a growth in α (Fig. 1, curve *3*). As a result, the high-frequency α values of the [111]-phase are close to those in the transition region. At high temperatures, the **M** vector is directed along the [100] axis. This direction is characterized by a weak magnetoelastic coupling and the oscillations acquire the character of a quasielastic mode.

Analogous temperature dependences were obtained for the spinel crystals of type B (a = 0.57, b = 0.39, c = 0.04; M_s = 382 G). However, the $\alpha(T)$ curves in this case exhibit essential qualitative differences (Fig. 2). In the phase transition region, large peaks of the longitudinal ultrasonic wave damping are observed at lower ultrasonic wave frequencies (f < 6 MHz) as compared to those in the crystal of type A. Averaged over the samples studied, estimates of the internal magnetic field strength determined taking into account that the maximum damping $\alpha(T, \omega)$ is observed at a frequency of $\omega_a \approx \omega_0$ yield $H_{in} \sim 8$ and 0.9 Oe for the samples of types A and B, respectively. These values of the internal magnetic field are confirmed by experimental investigations of the coercive force of analogous samples, which was close to the anisotropic field strength [5]. At higher frequencies (Fig. 2, curve *3*), the maximum of $\alpha(T)$ in the region of inversion of the K_1 sign is poorly distinguishable on the high damping background at temperatures far from the transition temperature. This behavior can be related to the fact that, in comparison with type A crystals, the samples of type B contain a greater number of domains (due to the smallness of K_1 in a broad temperature range) [1] and exhibit a less sharp variation of the anisotropic field with the temperature [5]. This must result in a relatively small change in the angle (averaged over the domains) between the ultrasonic wave propagation direction and the magnetization vector **M** in the regions of the phase transition, which is a factor determining the magnetoelastic interaction efficiency [6].

In order to check for the proposed difference in the properties of type A and B crystals, we have studied these spinels by X-ray diffraction. The results showed that the crystal structures of the two samples were identical, the lattice parameters calculated by the X-ray data being $a_1 = 8.48 \pm 0.02$ Å and $a_2 = 8.50 \pm 0.03$ Å for type A and B crystals, respectively. However, the crystal of type B exhibited a very small deviation from cubic to tetragonal symmetry: $a/c = 1.006 \pm 0.002$. In addition, the diffraction intensity in the sample of type B increased with the angle of diffraction to a greater extent as compared to that in type A, which is evidence of a greater macroscopic disorder of the crystalline substance in the former case. Thus, taking into account the X-ray diffraction data and the values of the saturation magnetization and internal field strengths determined for the crystals of types A and B, we may conclude that the observed difference in the magnetic and magnetoelastic properties of manganeze-zinc spinels with close compositions grown by different methods is explained by a greater macroscopic disorder in the crystals of type B and by the different arrangement of Fe^{2+} and Fe^{3+} ions in the octahedral and tetrahedral voids of the spinel lattice. These distinctions are related to differences in the crystal growth methods.

Acknowledgments. The authors are grateful to Prof. V.G. Shavrov for fruitful discussions and valuable remarks, to S.G. Abarenkova for kindly providing the samples, to M.V. Bazhenov for his help in conducting

experiments, and to E.A. Golubev for the X-ray diffraction analysis of samples.

This work was supported by the Russian Foundation for Basic Research, project no. 00-02-16710.

REFERENCES

1. M. V. Bazhenov and L. N. Kotov, Akust. Zh. **43** (6), 732 (1997) [Acoust. Phys. **43**, 646 (1997)].
2. V. D. Buchel'nikov and V. G. Shavrov, Pis'ma Zh. Éksp. Teor. Fiz. **60** (7), 534 (1994) [JETP Lett. **60**, 548 (1994)].
3. B. A. Goldin, L. N. Kotov, L. K. Zarembo, and S. N. Karpachev, *Spin-Phonon Coupling in Crystals (Ferrites)* (Nauka, Leningrad, 1991).
4. L. N. Kotov and M. V. Bagenov, in *Proceedings of the II Ultrasonics World Congress, Yokohama, Japan, 1997*, p. 240.
5. S. G. Abarenkova, S. A. Kochnov, I. V. Saenko, and M. A. Kharinskaya, Élektron. Tekh., Ser. 6: Mater. **8** (264), 28 (1991).
6. G. A. Smolenskiĭ, V. V. Lemanov, G. M. Nedlin, *et al.*, *Physics of Magnetic Dielectrics* (Nauka, Leningrad, 1974).

Translated by P. Pozdeev

Technical Physics Letters, Vol. 28, No. 2, 2002, pp. 108–109. Translated from Pis'ma v Zhurnal Tekhnicheskoĭ Fiziki, Vol. 28, No. 3, 2002, pp. 54–59.

The Effect of Turbulent Mixing on the Moving Liquid Layer Energy Conversion into the Internal Energy of a Compressed Gas and the Character of the Gas Compression

M. V. Bliznetsov, I. G. Zhidov, E. E. Meshkov, N. V. Nevmerzhitskiĭ, E. D. Sen'kovskiĭ, E. A. Sotskov, and V. A. Til'kunov

Institute of Experimental Physics, Russian Federal Nuclear Center, Sarov, Russia

e-mail: root@gdd.vniief.ru

Received September 10, 2001

Abstract—The compression of a planar heated gas layer by a moving liquid layer and the effect of turbulent mixing at the liquid–gas interface on the character of gas compression were experimentally studied. The gas compression by the liquid layer in the deceleration stage is accompanied by development of the Rayleigh–Taylor instability and the turbulent mixing (TM). The liquid fragmentation in the TM zone leads to a sharp increase in the heat transfer from hot gas to liquid. As a result, the gas compression dynamics significantly differs, both quantitatively and qualitatively, from that observed in the case of a solid piston. The dynamics of a liquid layer featuring the TM was compared to that of an analogous layer in the case when the TM development was fully suppressed by increased layer strength. The level of the gas compression by the liquid layer exceeded (by a factor of up to ~1.5) the compression achieved with a solid piston. *© 2002 MAIK "Nauka/Interperiodica".*

The phenomenon of turbulent mixing (TM) of contacting materials, developed as a result of the acceleration of boundaries between differential density regions, may significantly influence the process of energy accumulation in layered systems [1]. This study is a continuation of the previous model investigations of the effect of TM on the process of energy conversion in a layered system comprising liquid layers separated by gas spacers [2, 3]. The system described below differs from that reported in [3] by a high initial temperature of the compressed gas.

The experiments were performed in a system schematically depicted in Fig. 1. A liquid layer was placed in an open transparent container capable of moving in a vertical cylindrical channel with transparent walls. The channel diameter was 5 cm; the total weight of the container with a sample liquid in all experiments was 45 g. The container separated the channel into two parts, which were filled with different explosive gas mixtures. The bottom part contained an acetylene–oxygen mixture $C_2H_2 + 2.5O_2$ (I), while the top part contained a hydrogen–oxygen mixture $2H_2 + O_2$ (II). The detonation of both mixtures was simultaneously initiated by electric spark discharge gaps.

The explosion of mixture I liberates a greater energy as compared to that evolved from mixture II. Accordingly, the pressure of the products of explosion in the bottom part is higher than that in the top part and the container initially moves with acceleration upward. In this stage, a boundary between the liquid and the products of explosion of mixture II is stable. As the container moves upward, the gaseous products in the top part are compressed. At a certain time instant, the growing pressure begins to decelerate the container (the acceleration is directed from the gas phase to the liquid). This leads to development of the Rayleigh–Taylor instability [4] and the turbulent mixing.

In order to establish the degree of the TM influence upon the dynamics of gas compression, we performed a series of comparative experiments with the liquid layers composed either of water (featuring the TM development) or of a high-strength jelly ("stabilized" layers in which the turbulent mixing is suppressed) The pattern of acceleration and deceleration of the container with a liquid layer was recorded with a high-speed video camera of the VKF-13 type.

The results of our experiments are presented in Fig. 2, showing the container displacement as a function of time $X(t)$ for the liquids of different types and for various initial volumes of the channel part filled with the explosive acetylene–oxygen mixture I. A change in the initial volume of mixture I alters the liquid layer dynamics, the TM development, and the effect of thermal processes in the TM zone on the efficiency of energy conversion in the system. These variations are most clearly manifested when the results are presented in a dimensionless form. In Fig. 2, the experimental data are plotted as $X^*(t^*)$, where $X^* = X/X_{max}$, $t^* = t/T_0$ (X_{max} is the maximum displacement of the stabilized layer, and T_0 is the time corresponding to X_{max} in a series of experiments with the same volume of mixture I). The $X^*(t^*)$ curves

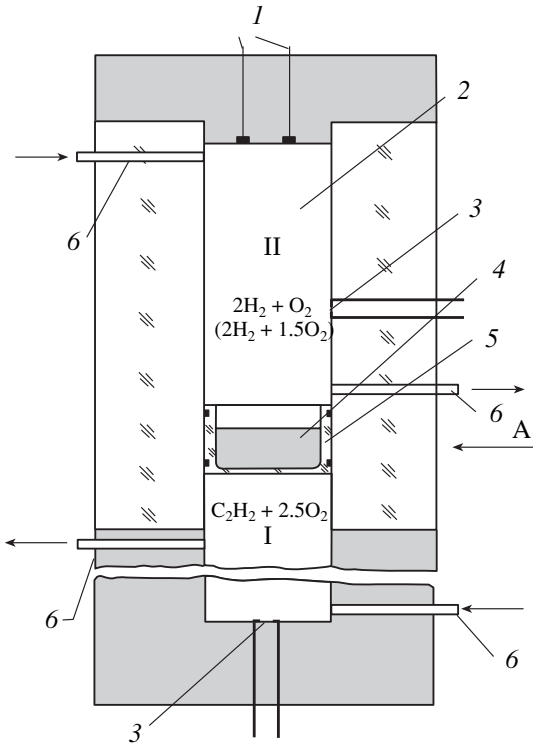

Fig. 1. A schematic diagram of the experiment on the compression of hot gaseous products of explosion of mixture II by a condensed layer accelerated by the hot compressed products of explosion of mixture I: (*1*) pressure sensors; (*2*) acceleration channel; (*3*) spark discharge gaps; (*4*) accelerated liquid layer; (*5*) container; (*6*) gas inlet and outlet channels; (A) video camera viewing direction. During the experiment, the gas channels *6* are blocked.

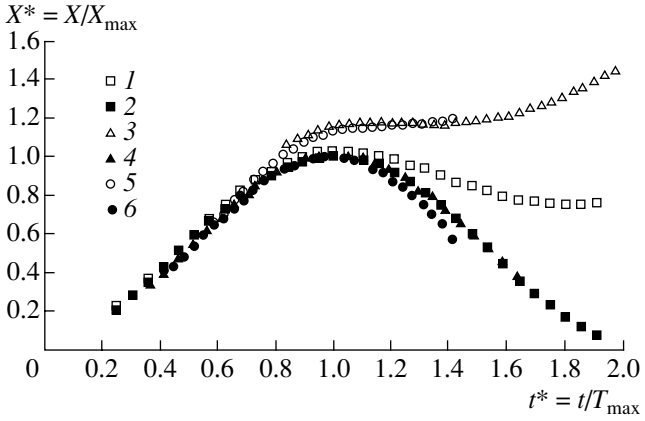

Fig. 2. Time variation of the relative displacement $X^*(t^*)$ in the experiments with (*1*, *3*, *5*) water and (*2*, *4*, *6*) stabilized (TM-free) liquid layer for various initial volumes of the $C_2H_2 + 2.5O_2$ mixture $V_I = 44$ cm^3 (*1*, *2*), 78.5 cm^3 (*3*, *4*), 117.8 cm^3 (*5*, *6*); the initial volume of the $2H_2 + O_2$ mixture was $V_{II} = 165$ cm^3.

for the stabilized layer are similar to that observed for the air compression at room temperature [3]. This behavior is described by a dome-shaped curve, according to which the container with the stabilized liquid layer is decelerated, stopped, and driven back.

Compression of the hot gaseous products of explosion of mixture II by the nonstabilized liquid (water) layer is accompanied by the TM development and by the heat transfer from these gaseous products to particles of the liquid. This leads to qualitative changes in the compression dynamics. Initially, the container with water exhibits deceleration similar to that with the stabilized liquid. However, the acceleration sign is then inverted and the container is accelerated again toward the compressed gas. The depth of the TM zone penetration into water keeps increasing for some time, but then the TM zone ceases to grow. It should be noted that the total width of the TM zone in water continues to increase. An increase in the initial volume of mixture I leads to a growth of the TM zone and of the influence of thermal processes.

The above-described experimental setup for the hot gas compression by a liquid layer ensured good reproducibility of the results. By varying the experimental arrangement, it is possible to change the rate of physical processes accompanying the compression. This is achieved by using various substances in the liquid layer (water versus jelly layers of variable strength), which determines the rate of TM at the unstable gas–liquid boundary, the liquid layer fragmentation, and the intensity of thermal processes. The experiments conducted under various conditions revealed both quantitative and qualitative changes in the motion of the container with the liquid layer.

The above results (i) show the need in describing processes in the turbulent mixing zone in more detail, rather than restricting the consideration to dynamics of the size of this zone; (ii) offer clear illustration of the effect of turbulent mixing on the physical processes encountered in the attempts at obtaining high energy densities in layered cumulative systems; and (iii) provide a basis for the experimental verification of numerical methods for describing multiphase flows accompanied by turbulent mixing and heat transfer. It is important to note that the experimental procedure involves a relatively small number of well-known physical processes and employs substances with known physical characteristics.

Acknowledgments. This study was partly supported by the Los Alamos National Laboratory (USA), contract no. B70040006-35 T3 034.

REFERENCES

1. E. I. Zababakhin, Zh. Éksp. Teor. Fiz. **49** (2), 721 (1965).
2. I. G. Zhidov, E. E. Meshkov, and N. V. Nevmerzhitskiĭ, Vopr. At. Nauki Tekh., Ser. Teor. Prikl. Fiz., Nos. 1–2, 20 (1996).
3. I. G. Zhidov, E. E. Meshkov, N. V. Nevmerzhitskiĭ, *et al.*, in *Proceedings of the VII International Workshop on Physics of Turbulent Mixing of Compressible Media, St. Petersburg, 1999*, p. 36.
4. G. I. Taylor, Proc. R. Soc. London, Ser. A **201**, 192 (1950).

Translated by P. Pozdeev

Technical Physics Letters, Vol. 28, No. 2, 2002, pp. 110–112. Translated from Pis'ma v Zhurnal Tekhnicheskoĭ Fiziki, Vol. 28, No. 3, 2002, pp. 60–65.

Determining the Axis Orientation of an Ultrahigh-Energy Cosmic Cascade Shower

A. D. Filonenko

East-Ukrainian National University, Lugansk, Ukraine

Received August 16, 2001

Abstract—A practical solution is found for the problem of determining the cascade shower axis orientation, which is based on using two lunar modules, each carrying three mutually perpendicular dipoles. The proposed solution supplements the previous results concerning the possibility of determining the electromagnetic cascade energy using the results of measurements of the RF component of radiation generated by the shower δ-electrons. © *2002 MAIK "Nauka/Interperiodica".*

As is known, achievements in the physics of cosmic rays in the ultrahigh energy range ($W_0 > 10^{19}$ eV) were related predominantly to the development of traditional detection methods [1]. However, the upper energy level of these setups will not rise above 10^{20}–10^{21} eV in the nearest future. For example, a giant detector of the *Pierre Auger* project will possess a total working area of 600 km^2 for both hemispheres [2], which corresponds to the frequency of events on the order of 60 particles per year in the energy range $W_0 > 10^{20}$ eV. Data on the cosmic rays of these energies available at present are indicative of an insignificant variation of the energy spectrum index [3]. Taking this fact into account, the frequency of events with $W_0 > 10^{21}$ eV for the aforementioned setup can be expected on the order of one particle per year. In order to obtain reliable information about cosmic rays, the frequency must be at least one order higher. However, in order to retain the registration rate on the level of 60 events per year for cosmic particles with energies $W_0 > 10^{21}$ eV, the detector area has to be increased by almost two orders of magnitude. These estimates show that a detector operating on the traditional principles with an effective area of about 10^6 km^2 cannot be constructed at present.

However, it seems that even now there is a possibility to increase the detector area up to 10^7 km^2 with the aid of a radiodetection method. The solution is based on determining the characteristics of a radiation field generated by δ-electrons of a cascade shower in a gaseous or condensed medium [4–6]. Especially good prospects are offered by a radioastronomic method [7–10] and by the high-energy particle detection on a lunar orbit [11, 12].

The radiodetection of cosmic rays involves a very interesting circumstance. There was only one attempt at experimentally determining the direction of arrival of a cosmic particle [13]. This direction was determined very roughly by measuring the relative delay of an RF signal induced in a radiodetector by the Cerenkov component of radiation from an extensive atmospheric shower. As is known [14], this radiation component is very weak outside a narrow shower radiation cone and cannot be effectively employed in the radiodetection method. Moreover, this technique is practically inapplicable for detecting ultrahigh-energy particles ($W_0 > 10^{21}$ eV) with the aid of lunar modules.

Below, it is demonstrated how the result can be obtained provided that a shower is propagating in a condensed nonconducting medium. In such a case, it is possible not only to determine the direction of the particle arrival, but to estimate the particle energy as well at an accuracy sufficient for practical purposes. Once proved, these facts, together with the previously published results on the mechanism of radioemission from the cascade shower δ-electrons in the wavelength range $\lambda > L$ (where L is the effective cascade length), placed on a principally new ground the method of radiodetection of ultrahigh-energy cosmic rays ($W_0 > 10^{21}$ eV) on a lunar orbit.

Determination of the axis of a cascade shower is performed with the aid of three mutually perpendicular symmetric dipoles. As is known, the directivity pattern of an insulated dipole with a length of $2a$ is described by the expression

$$F(\alpha) = \frac{\cos(ma\cos\alpha) - \cos ma}{(1 - \cos ma)\sin\alpha}, \qquad (1)$$

where $m = 2\pi/\lambda$ and α is the angle between the dipole axis and the observation direction **n** (see, e.g, [15]). The simple antennas (and elements of the complicated systems) usually represent half-wave dipoles. However, from the standpoint of a real detector arranged on a lunar satellite orbit, the use of a half-wave dipole ($a = \lambda/4$) with a length of $2a = 5$ m (for an acceptable frequency of $\nu = 30$ MHz [9, 10]) may present certain technical difficulties. Under these conditions, a solution is offered by a shortened dipole with an inductance serially connected in the circuit to retain the resonance fre-

1063-7850/02/2802-0110$22.00

quency. As can be readily checked, expression (1) in this case can be replaced to within a sufficient practical accuracy by the simplest function $F_1(\alpha) = \sin\alpha$. For example, upon changing the half-wave dipole for a quarter-wave one ($a = \lambda/8$), a difference between the directivity patterns would not exceed 2%.

Below we will use the normalized function $F_1(\alpha) = \sin\alpha$ to describe the directivity pattern of a receiving antenna of the radiodetector. In addition, we will take into account that the radioemission diagram of a shower in the wavelength range $\lambda > L$ is also approximately described by the same $F_1(\alpha)$ function [4–6]. This implies that the radiation field strength at an arbitrary point is $E = E_0\sin\alpha$, where α is the angle between the emission direction **n** and the cascade axis. As is known, the field strength vector **E** lies in the plane containing the shower axis (or the dipole axis) and the observation direction. In the far zone, the field is always perpendicular to the emission direction ($\mathbf{E} \perp \mathbf{n}$).

For determining the cascade axis direction (and, hence, the arrival direction of a cosmic particle), there must be two modules on a lunar orbit, each carrying three mutually perpendicular dipoles, with signal amplifiers and emf meters for each antenna, and equipment determining the position of the modulus relative to a lunar system of coordinates (see the figure). In order to reduce the error of determination of the signal arrival direction for a given orbit altitude h, the distance between the modules must not be much smaller than $S = 2\sqrt{2R_m h}$, where R_m is the radius of the Moon.

A cascade shower, produced in the soil by propagation of a charged ultrahigh-energy particle crossing the surface of the Moon, will induce the emf (u_{1x}, u_{1y}, u_{1z}) and (u_{2x}, u_{2y}, u_{2z}) at the antenna outputs of the first and second lunar modules, respectively. These signals can be expressed (see, e.g., [15]) through the field strength E and the direction cosines of the angles ϕ, ξ, and η. This leads to a system of eight equations for determining the direction cosines of the vectors $\mathbf{E}_1$ and $\mathbf{E}_2$ in the system of coordinates of each modulus:

$$\begin{aligned} u_{ix} &= \frac{kE_i}{R_i}\sin\alpha_i\cos\phi_i, \\ u_{iy} &= \frac{lE_i}{R_i}\sin\alpha_i\cos\xi_i, \quad i = 1, 2, \\ u_{iz} &= \frac{lE_i}{R_i}\sin\alpha_i\cos\eta_i, \\ \cos^2\phi_i + \cos^2\xi_i + \cos^2\eta_i &= 1, \end{aligned} \tag{2}$$

where l is the effective dipole length, i is the modulus number, R_i is the distance from the ith modulus to shower, and α_i is the angle between the shower axis and the vector $\mathbf{R}_i$.

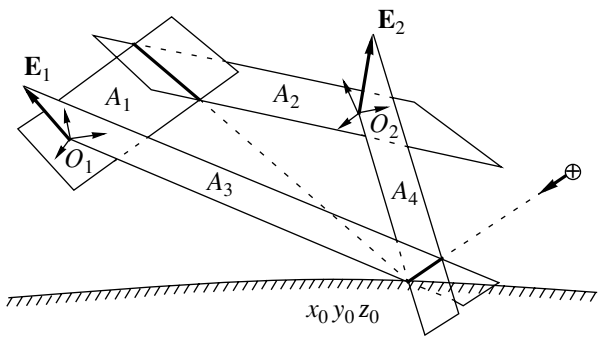

A schematic diagram illustrating determination of a cascade shower axis.

Consider a straight line determined by intersection of the planes A_1 and A_2 drawn through the origin of the system of coordinates of each modulus. The direction vectors in these planes are $\mathbf{E}_1$ and $\mathbf{E}_2$, the components of which are proportional to the emf induced in the corresponding antenna:

$$\begin{aligned} u_{1x}x' + u_{1y}y' + u_{1z}z' &= 0, \\ u_{2x}x'' + u_{2y}y'' + u_{2z}z'' &= 0. \end{aligned} \tag{3}$$

If a radiation source is placed at an arbitrary point of the line (3), the radiation directions n_1 and n_2 to each modulus will be perpendicular to $\mathbf{E}_1$ and $\mathbf{E}_2$, respectively, for an arbitrary angle α. In other words, the cascade shower (as a point) for a given set of (u_{1x}, u_{1y}, u_{1z}) and (u_{2x}, u_{2y}, u_{2z}) values can occur only on the line (3). It is known that cascade showers are possible only on the surface of the Moon. Therefore, the point of intersection of line (3) with the sphere $x^2 + y^2 + z^2 = R_m^2$, where R_m is the radius of the Moon, uniquely determines the shower coordinates x_0, y_0, z_0 (see the figure).

According to the above considerations, the shower axis belongs simultaneously to the planes containing vectors $\mathbf{R}_1$, $\mathbf{E}_1$ and $\mathbf{R}_2$, $\mathbf{E}_2$. Thus, the direction of this axis can be determined by drawing (a) the plane A_3 through the coordinate origin $O_1(x_1, y_1, z_1)$ of the first modulus, the point (x_0, y_0, z_0), and the direction $\mathbf{E}_1$; and (b) the plane A_4 through the coordinate origin $O_2(x_2, y_2, z_2)$ of the second modulus, the point (x_0, y_0, z_0), and the direction $\mathbf{E}_2$:

$$\begin{aligned} &\begin{vmatrix} x - x_1 & y - y_1 & z - z_1 \\ x_1 - x_0 & y_1 - y_0 & z_1 - z_0 \\ E_{1x} & E_{1y} & E_{1z} \end{vmatrix} = 0, \\ &\begin{vmatrix} x - x_2 & y - y_2 & z - z_2 \\ x_2 - x_0 & y_2 - y_0 & z_2 - z_0 \\ E_{2x} & E_{2y} & E_{2z} \end{vmatrix} = 0. \end{aligned} \tag{4}$$

The straight line (4) determined by the intersection of these planes coincides with the cascade axis direction.

Using this method for determining the direction of motion of a cosmic particle, it is also possible to solve the problem concerning the number N_0 of electrons at the cascade maximum. According to [4–6], the field strength amplitude in the radiation pulse is $E = BN_0\sin\alpha/R$, where the coefficient B depends only on the known physical constants. Thus, by determining the direction cosines from (3) and the ratio $\sin\alpha/R$ using the above procedure, we can uniquely determine the number of electrons N_0 in the shower and, hence, the energy W_0 of the given cosmic particle.

Concerning the scheme of determining the particle motion direction, it is necessary to note that Eqs. (2) for $i = 1, 2$ determine the components E'_{ix}, E'_{iy}, E'_{iz} of the vector E_i in the coordinate system of the first ($i = 1$) or second ($i = 2$) modules. In order to solve Eqs. (3) and (4), it is necessary to express the projections E'_{ix}, E'_{iy}, E'_{iz} through E_{ix}, E_{iy}, E_{iz} in the lunar coordinate system. This can be done with the aid of a matrix of the vector transformation upon rotation of the Cartesian coordinate system. The components of this matrix at any time instant can be obtained from the system determining the orientation of modules: this technical task is readily solved at present.

REFERENCES

1. V. L. Ginzburg, Usp. Fiz. Nauk **166** (2), 169 (1996) [Phys. Usp. **39**, 155 (1996)].
2. B. Schwarzschild, Phys. Today, No. 2, 616 (1997).
3. M. Takeda, N. Hayashida, K. Honda, *et al.*, Phys. Rev. Lett. **81**, 1163 (1998).
4. P. I. Golubnichiĭ and A. D. Filonenko, Pis'ma Zh. Tekh. Fiz. **20** (12), 57 (1994) [Tech. Phys. Lett. **20**, 499 (1994)].
5. P. I. Golubnichiĭ, A. D. Filonenko, and V. I. Yakovlev, Izv. Akad. Nauk, Ser. Fiz. **58** (12), 115 (1994).
6. P. I. Golubnichiĭ and A. D. Filonenko, Ukr. Fiz. Zh. **41** (7/8), 696 (1989).
7. R. D. Dagkesamanskiĭ and I. M. Zheleznykh, Pis'ma Zh. Éksp. Teor. Fiz. **50** (5), 233 (1989) [JETP Lett. **50**, 259 (1989)].
8. J. Álvarez-Múniz and E. Zas, in *Proceedings of the 25th International Cosmic Ray Conference, 1997*, Vol. 7, p. 309.
9. A. D. Filonenko, Izv. Akad. Nauk, Ser. Fiz. **61** (3), 543 (1997).
10. A. D. Filonenko, Pis'ma Zh. Éksp. Teor. Fiz. **70** (10), 639 (1999) [JETP Lett. **70**, 649 (1999)].
11. A. D. Filonenko, Pis'ma Zh. Tekh. Fiz. **23** (10), 57 (1997) [Tech. Phys. Lett. **23**, 399 (1997)].
12. P. I. Golubnichiĭ and A. D. Filonenko, Kosm. Nauka Tekhnol. **5** (4), 87 (1999).
13. W. E. Hazen, A. Z. Hendel, H. Smith, and N. J. Shah, Phys. Rev. Lett. **24** (9), 476 (1970).
14. V. B. Atrashkevich, O. V. Vedeneev, H. R. Allan, *et al.*, Yad. Fiz. **28** (3), 712 (1978) [Sov. J. Nucl. Phys. **28**, 366 (1978)].
15. A. A. Pistol'kors, *Antennas* (Moscow, 1947).

Translated by P. Pozdeev

Technical Physics Letters, Vol. 28, No. 2, 2002, pp. 113–115. Translated from Pis'ma v Zhurnal Tekhnicheskoĭ Fiziki, Vol. 28, No. 3, 2002, pp. 66–72.

High-Power 1.8-μm InGaAsP/InP Lasers

E. G. Golikova, V. A. Kureshov, A. Yu. Leshko, A. V. Lyutetskiĭ, N. A. Pikhtin, Yu. A. Ryaboshtan, S. O. Slipchenko, Z. N. Sokolova, N. V. Fetisova, A. D. Bondarev, and I. S. Tarasov

Ioffe Physicotechnical Institute, Russian Academy of Sciences, St. Petersburg, Russia

Received September 13, 2001

Abstract—Separately bounded InGaAsP/InP laser heterostructures with two stressed quantum wells emitting at a wavelength of 1.8 μm were obtained by metalorganic vapor-phase epitaxy. The laser diodes with a strip width of 100 μm provide for an output radiation power of 1.2 W in the continuous operation mode at a temperature of 20°C. A minimum threshold current density was 320 A/cm^2 and a differential quantum efficiency was η_d = 28% for a Fabry–Perot resonator length of 1.4 mm. The internal optical losses in the laser heterostructure studied amounted to 5.6 cm^{-1}. © *2002 MAIK "Nauka/Interperiodica".*

Semiconductor lasers emitting in a wavelength region of 1.8–1.9 μm are widely applied in practice. In particular, these devices are used for pumping holmium-doped crystal lasers, in laser diode spectroscopy, and in medicine. Such laser diodes are created and developed in a few laboratories reaching advanced metalorganic-hydride vapor-phase epitaxy (MOVPE) and molecular-beam epitaxy technology levels [1–6]. The laser diodes emitting at 1.8–1.9 μm are obtained using InGaAsP [1–3] and AlGaInAsSb [4, 5] solid solution systems. Possessing better technological properties, the former system is preferred.

This work continues our previous investigations [1–6] devoted to high-power semiconductor lasers based on InGaAsP solid solutions, implementing separately bounded laser heterostructures fabricated by MOVPE [6–10]. The purpose of this study was to develop the MOVPE technology of obtaining InGaAsP heterostructures with stressed quantum wells emitting in the wavelength region of 1.8–1.9 μm and create lasers based on these heterostructures.

The separately-bounded InGaAsP laser heterostructures with two stressed quantum wells (SQWs) were based on *n*-InP substrates. The InGaAsP solid solution composition for SQWs was selected so as to obtain a maximum (1.5%) possible lattice mismatch. This ensured the formation of stressed layers with a high intrinsic quantum yield and provided for a long working life of the laser diodes. [2]. Figure 1 shows an energy band diagram of the laser heterostructure studied. The SQW solid solution composition in the active region corresponded to a bandgap of E_g = 0.68 eV. The SQW width was 90 Å and the intermediate waveguide layer thickness between SQWs was 200 Å. The waveguide layer with a thickness of D = 0.5 μm had E_{gw} = 1.03 eV. Neither the active region nor the waveguide layers were intentionally doped.

The 1.5-μm-thick broadband *n*- and *p*-type emitters were doped to 5×10^{17} cm^{-3}. A contact layer with a thickness of 0.3 μm had a hole concentration of 2×10^{18} cm^{-3}. The insulating SiO_2 layer was photolithographically processed to obtain the strips with a width of W = 100 μm. Finally, the heterostructures were provided with Au/Te and Au/Zn ohmic contacts. Then the structure was divided into laser diodes with a resonator length of L = 500–4000 μm and the resonator edges were coated with Si/SiO_2 high-reflection (HR) layers possessing a reflection coefficient of $R > 0.95$ and with antireflection (AR) layers possessing $R < 0.08$. The laser diode samples were mounted on copper heat exchangers and fixed with the aid of an indium-based solder.

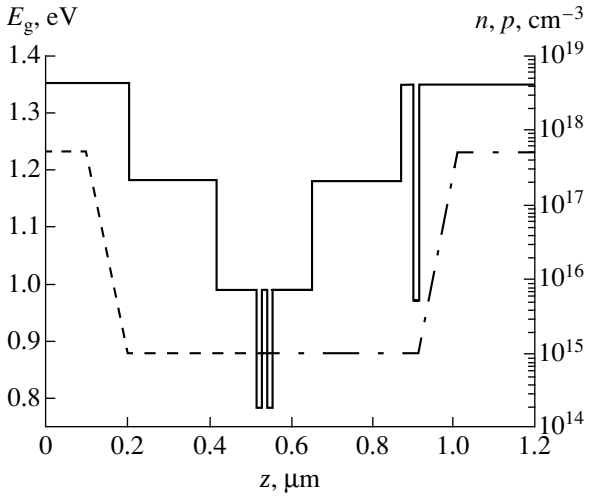

Fig. 1. A schematic energy band diagram of the separately bounded InGaAsP/InP laser heterostructure (solid profile) and the calculated dopant concentration profiles for the donor (Si, dashed line) and acceptor (Zn, dash-dot line) impurities.

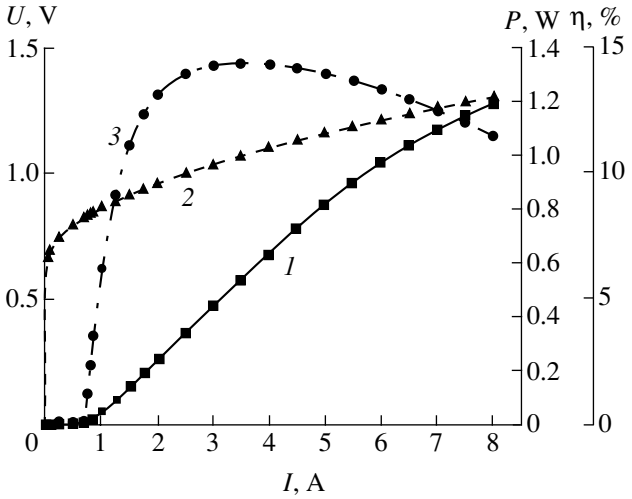

Fig. 2. The plots of (*1*) output power *P*, (*2*) voltage *U*, and (*3*) total efficiency η versus pumping current *I* measured in the continuous operation mode for an InGaAsP/InP laser diode with the strip width $W = 100$ μm, a resonator length of 1.4 mm, and the mirror (HR, $R = 95\%$) and antireflection (AR, $R = 5\%$) dielectric coatings.

The output power–current characteristics of laser diodes of various length, operating in the continuous operation mode at a wavelength of 1.8 μm, were measured at a heat exchanger temperature of $T = 20$°C (Fig. 2). The laser diodes with a resonator length of 1.4 mm yielded a power of 1.2 W with a differential quantum efficiency remaining unchanged ($\eta_d = 28\%$) at a pumping current of up to 4 A. The total efficiency was $\eta = 14.5\%$. Further increase in the resonator length was unexpedient, since this was accompanied (because of considerable internal losses) with a significant drop in η_d. The reduced differential resistivity was 1.2×10^{-4} Ω cm^2. The onset of the power–current characteristic bending related to the active region heating was observed at a pumping current of 8–10 A for all laser diodes with a resonator length of 1.4–2 mm. In our opinion, this was explained by a low level of the intrinsic quantum yield and high internal optical losses. The threshold current density determined in four cleaved samples was on the order of 300–350 A/cm^2, which is two times as great as the value for the laser diodes emitting at 1.3 μm [6, 7].

Figure 3 shows a plot of the experimental inverse quantum efficiency (black circles) versus the Fabry–Perot resonator length. Using a linear approximation of this dependence, it is possible to estimate the intrinsic quantum yield of the laser diode. In our experiments, the induced intrinsic quantum yield for the lasers emitting at 1.8 μm was $\eta_i = 50 \pm 3\%$. The internal optical losses determined for the laser diodes presented in Fig. 3 was $\alpha_i = 5.6$ cm^{-1}. The laser structure design can be optimized so as to reduce the level of internal optical losses in emitters of the *n*- and *p*-type. In particular, a certain increase in the induced intrinsic quantum yield is provided by using a step-divergent waveguide [11].

We have also determined the temperature dependence of the threshold current density in the laser diodes using the output power-current characteristics measured in the temperature interval from 10 to 60°C. The results of these measurements are presented in Fig. 4. The characteristic temperature T_0 varied, depending on the laser diode resonator length, within 50–60°C. This almost coincides with the parameter T_0 determined for the laser diodes operating at a wavelength of 1.5 μm [12].

Thus, we have obtained laser diodes with an output radiation power of 1.2 W in the continuous operation mode at a wavelength of 1.8 μm. The differential quantum efficiency of the diodes with a resonator length of

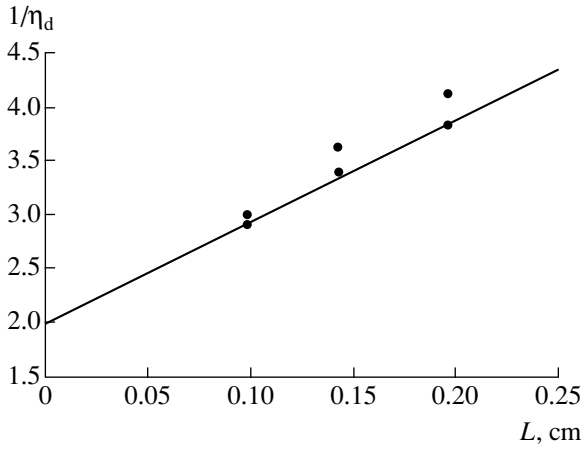

Fig. 3. The plot of experimental inverse differential quantum efficiency $1/\eta_d$ versus the Fabry–Perot resonator length *L* (black circles) of the InGaAsP/InP laser diodes ($\lambda = 1.8$ μm) with a strip width of $W = 100$ μm. The solid line shows a linear approximation of the experimental data.

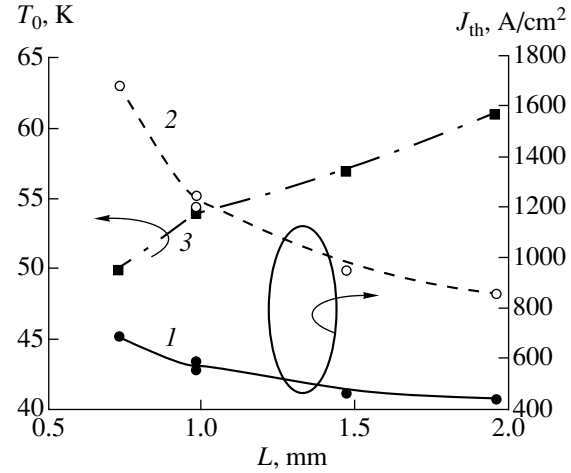

Fig. 4. Temperature dependence of the characteristics of InGaAsP/InP laser diodes ($\lambda = 1.8$ μm) with a strip width of $W = 100$ μm: (*1*, *2*) threshold current density J_{th} measured and 20°C and 60°C, respectively; (*3*) parameter T_0.

1.4 mm was 28% for the internal optical losses not exceeding 5.6 cm^{-1}. Depending on the resonator length, the total laser efficiency varied within 12–16%. The characteristic parameter T_0 determined in the temperature interval from 10 to 60°C was 50–60°C.

Acknowledgments. This study was supported by the Scientific-Technological Program "Physics of Solid-State Nanostructures" (project nos. 99-2037 and 99-2038) and by the Russian Foundation for Basic Research (project no. 01-02-17851).

REFERENCES

1. S. O'Brien, W. Plano, J. Major, *et al.*, Electron. Lett. **31**, 105 (1995).
2. X. He, D. Xu, A. Ovtchinnikov, *et al.*, Electron. Lett. **35**, 1343 (1999).
3. J. S. Major, D. W. Nam, J. S. Osinski, and D. F. Welch, IEEE Photonics Technol. Lett. **5**, 594 (1993).
4. H. K. Choi and S. J. Eglash, IEEE J. Quantum Electron. **QE-27**, 1555 (1991).
5. H. K. Choi and S. J. Eglash, Appl. Phys. Lett. **61**, 1154 (1992).
6. D. A. Livshits, I. V. Kochnev, V. M. Lantratov, *et al.*, Electron. Lett. **36**, 1848 (2000).
7. D. A. Livshits, A. Yu. Egorov, I. V. Kochnev, *et al.*, Fiz. Tekh. Poluprovodn. (St. Petersburg) **35**, 380 (2001) [Semiconductors **35**, 365 (2001)].
8. A. Yu. Leshko, A. V. Lyutetskiĭ, N. A. Pikhtin, *et al.*, Fiz. Tekh. Poluprovodn. (St. Petersburg) **34**, 1457 (2000) [Semiconductors **34**, 1397 (2000)].
9. E. G. Golikova, V. A. Gorbylev, Yu. V. Il'in, *et al.*, Pis'ma Zh. Tekh. Fiz. **26** (7), 57 (2000) [Tech. Phys. Lett. **26**, 295 (2000)].
10. E. G. Golikova, V. A. Kureshov, A. Yu. Leshko, *et al.*, Fiz. Tekh. Poluprovodn. (St. Petersburg) **34**, 886 (2000) [Semiconductors **34**, 853 (2000)].
11. E. G. Golikova, V. A. Kureshov, A. Yu. Leshko, *et al.*, Pis'ma Zh. Tekh. Fiz. **26** (20), 40 (2000) [Tech. Phys. Lett. **26**, 913 (2000)].
12. G. G. Zegrya, N. A. Pikhtin, G. V. Skrynnikov, *et al.*, Fiz. Tekh. Poluprovodn. (St. Petersburg) **35** (8), 1001 (2001) [Semiconductors **35**, 962 (2001)].

Translated by P. Pozdeev

Technical Physics Letters, Vol. 28, No. 2, 2002, pp. 116–118. Translated from Pis'ma v Zhurnal Tekhnicheskoĭ Fiziki, Vol. 28, No. 3, 2002, pp. 73–79.

On the Magnetic-Field-Induced Changes in the Parameters of Phase Transitions

M. N. Magomedov

Institute for Problems of Geothermics, Dagestan Scientific Center, Russian Academy of Sciences, Makhachkala, Dagestan, Russia

e-mail: danterm@datacom.ru

Received August 27, 2001

Abstract—Equations describing a change in the thermodynamic parameters of a first-order phase transition in para- and diamagnetic substances under the action of a homogeneous magnetic field are derived. It is shown that the magnetic field effect on the phase transition parameters is negligibly small in the regions of the phase diagram where the P–T curves vary monotonically. However, the applied magnetic field may significantly change the T_f and P_f values in the regions where either $P_f(T)$ or $T_f(P)$ curves exhibit extrema. Substances in which this effect can be observed are indicated. © *2002 MAIK "Nauka/Interperiodica".*

Let us consider the equilibrium of two phases in an isotropic substance (not possessing ferromagnetic properties) exposed to a homogeneous magnetic field with a strength H. The free Gibbs energy per mole of the ith phase is given by the formula [1]

$$G_i(T, P, H) = G_i(T, P, H = 0) - (\mu_0/2)\chi_i V_i H^2,$$

where $G_i(T, P, H = 0)$ is the free Gibbs energy of the ith phase ($i = 1, 2$) at a temperature T and pressure P in the absence of the magnetic field; μ_0 is the magnetic constant; and χ_i and V_i are the magnetic susceptibility and molar volume of the ith phase, respectively. Therefore, a difference between the free Gibbs energies of the two phases is

$$\Delta G = \Delta G_0 - (\mu_0/2)H^2\Delta(\chi V), \quad (1)$$

where ΔG_0 is free energy difference in the absence of the magnetic field.

A condition of the phase equilibrium for the first-order phase transition is as follows [2]:

$$\Delta G = \Delta(dG/dP)_{T,H}dP + \Delta(dG/dT)_{P,H}dT + \Delta(dG/dH)_{P,T}dH = 0,$$

$$\Delta(dG/dP)_{T,H} = \Delta V \neq 0, \quad (2)$$

$$\Delta(dG/dT)_{P,H} = -\Delta S \neq 0,$$

$$\Delta(dG/dH)_{P,T} = -\Delta M \neq 0.$$

Using these relationships and Eq. (1), we obtain the following expressions for the jumps in the molar volume, entropy, and magnetization upon this phase transition:

$$\Delta V = \Delta V_0 - (\mu_0/2)H^2\Delta[d(\chi V)/dP]_{T,H}, \quad (3)$$

$$\Delta S = \Delta S_0 + (\mu_0/2)H^2\Delta[d(\chi V)/dT]_{P,H}, \quad (4)$$

$$\Delta M = \mu_0 H\Delta(\chi V) + (\mu_0/2)H^2\Delta[\chi(dV/dH)_{T,P}]. \quad (5)$$

Here, ΔV_0 and ΔS_0 are the phase jumps of the molar volume and entropy for $H = 0$.

A simple analysis of Eqs. (2)–(5) shows that the pressure of the isothermal first-order phase transition varies under the action of the applied homogeneous field as follows:

$$(dP_f/dH)_T = (\mu_0 H/\Delta V)\{\Delta(\chi V) + (H/2)\Delta[\chi(dV/dH)_{T,P}]\}. \quad (6)$$

By the same token, the isobaric transition temperature varies according to the equation

$$(dT_f/dH)_P = -(\mu_0 H/\Delta S)\{\Delta(\chi V) + (H/2)\Delta[\chi(dV/dH)_{T,P}]\}. \quad (7)$$

According to Eq. (2), the phase transition temperature as a function of the pressure at any H = const is described by the Clapeyron–Clausius equation [1–4]

$$(dT_f/dP)_H = \Delta V/\Delta S = \{\Delta V_0 - (\mu_0/2)H^2\Delta[d(\chi V)/dP]_{T,H}\}/\{\Delta S_0 + (\mu_0/2)H^2\Delta[d(\chi V)/dT]_{P,H}\}. \quad (8)$$

Neglecting the terms related to the volume magnetostriction effect in Eqs. (6) and (7) and integrating these equations with respect to the field strength from 0 to H, we obtain expressions describing a shift of the phase

transition point as a result of the magnetic field application:

$$P_H - P_0 = -\{\Delta(\chi V)/\Delta[d(\chi V)/dP]_{T,H}\} \times \ln\{|1 + [(\Delta V - \Delta V_0)/\Delta V_0]|\}, \quad (9)$$

$$T_H - T_0 = -\{\Delta(\chi V)/\Delta[d(\chi V)/dT]_{P,H}\} \times \ln\{|1 + [(\Delta S - \Delta S_0)/\Delta S_0]|\}, \quad (10)$$

where P_0 and T_0 are the phase transition pressure and temperature for $H = 0$.

It should be noted that Eqs. (9) and (10) were derived without any restrictions concerning the values of relative differences $(\Delta V - \Delta V_0)/\Delta V_0$ and $(\Delta S - \Delta S_0)/\Delta S_0$ (these quantities were assumed neither small nor infinitely large). Assuming now that both ratios are much smaller than unity and using the expansion $\ln(1 + x) \cong x - x^2/2$, we obtain in the first approximation the results previously derived by Shklyar and Aleksandrov [5]:

$$P_H - P_0 \cong (\mu_0/2)H^2[\Delta(\chi V)/\Delta V_0], \quad (11)$$

$$T_H - T_0 \cong -(\mu_0/2)H^2[\Delta(\chi V)/\Delta S_0]. \quad (12)$$

It should be noted that these formulas were derived in [5] (to within the signs) for the effect of an applied magnetic field on a first-order phase transition of the crystal–liquid type.

Since the magnetic susceptibility of both para- and diamagnetic substances varies very slightly on melting [4], Eqs. (11) and (12) can be rewritten as

$$P_H - P_0 \approx (\mu_0/2)H^2\chi_s, \quad T_H - T_0 \approx -(P_H - P_0)(dT_f/dP)_H, \quad (13)$$

where χ_s is the magnetic susceptibility of the solid phase and dT_f/dP is the slope of the melting curve. For both para- and diamagnetic substances, we may roughly accept that $\chi_s \approx \pm 10^{-(5-6)}$ [1, 3]. For a field strength of $H = 10^3$ kOe, this yields $P_H - P_0 \approx \pm(0.1–0.01)$ bar. The melting curve slope in a first-order crystal–liquid phase transition can be taken approximately equal to $dT_f/dP \approx \pm(1–10)$ K/kbar [6], which leads to a very small change in the melting temperature for $H = 10^3$ kOe: $|T_H - T_0| \approx 10^{-(3-5)}$ K. In the case of normal melting ($dT_f/dP > 0$), the melting temperature will decrease for the paramagnetic substances ($\chi_s > 0$) and increase for the diamagnetic substances [4]. The substances exhibiting anomalous melting will exhibit the opposite trends. Note that, if the function χ exhibits significant changes on melting, the P_f and T_f will no longer be related to the susceptibility by simple expressions (13). Then, the melting behavior has to be described using Eqs. (3) and (10).

In view of the above numerical estimates, the problem of the magnetic field effect on the thermodynamic parameters of the first-order phase transitions in para- and diamagnetic substances might seem to be of little importance. However, as will be shown below, the *P–T* phase diagrams of some substances contain points where the effect of the magnetic field can be very significant. These are the points where either $P_f(T)$ or $T_f(P)$ curves exhibit extrema [7, 8].

When an extremum is present in the $P_f(T)$ curve, this point obeys the conditions $(dT_f/dP)_{H=0} = 0$ and $\Delta V_0 = 0$. Application of the magnetic field to the substance occurring at this extremum point gives rise to a jump in the molar volume, which is determined, according to formula (3), by the formula

$$\Delta V = (\mu_0/2)H^2V_f\Delta[\chi\beta - d(\chi/dP)_{T,H}], \quad (14)$$

where $\beta = -(d\ln V/dP)_T$ is the isothermal compressibility and V_f is the molar volume at the point where $\Delta V_0 = 0$.

Assuming that the susceptibility χ is constant (because of $\Delta V_0 = 0$) at the point of extremum under consideration and the pressure dependence of χ during the phase transition remains the same, the experimentally measured ΔV can be used to estimate the jump in the compressibility and vice versa. For most substances, the isothermal compressibility on melting is positive: $\Delta\beta > 0$ [7, 8]. Therefore, the application of a magnetic field to paramagnetic substances exhibiting an extremum (typically, maximum) on the melting curve $T_f(P)$ must result in a positive jump in the molar volume ($\Delta V > 0$). In this case, the field will shift the extremum on the melting curve toward higher pressures. This effect should be expected in substances such as the alkali metals or barium [6, 9]. In diamagnetic substances with an extremum on the melting curve $T_f(P)$, we can expect that the field application will lead to a decrease in the molar volume ($\Delta V < 0$). This is possible in a series of substances such as graphite, As, Sb, Se, and Te [6, 9], where the extremum on the melting curve $T_f(P)$ will shift toward lower pressures upon the field application.

Judging by Eqs. (6)–(8), the extremum on the first-order phase transition curve $T_f(P)$ must show a strong dependence of the phase transition pressure on the applied magnetic field strength. The effect should be more pronounced in the case of substances where the point of extremum is characterized either by significant changes in the magnetic susceptibility ($\Delta\chi$) and the volume magnetostriction ($\Delta[\chi(dV/dH)_{T,P}]$), or by small jumps in the isothermal compressibility ($\Delta\beta$) and the magnetic susceptibility derivative with respect to the pressure ($\Delta(d\chi/dP)_{T,H}$). If the χ value remains unchanged at the phase transition point where $\Delta V_0 = 0$, Eqs. (6) and (14) yield

$$(dP_f/dH)_T = \{\Delta[d\ln(V)/dH]_{T,P}\}/\{\Delta[\beta - (d\ln(\chi)/dP)_{T,H}]\}. \quad (15)$$

As can be readily seen from this expression, the coordinates of this point on the P–T diagram will not change upon application of the magnetic field provided that the volume magnetostriction exhibits no jump at the extremum of the $T_f(P)$ curve.

When an extremum is present in the $P_f(T)$ curve of the first-order phase transition, this point obeys the conditions $(dP_f/dT)_{H=0} = 0$ and $\Delta S_0 = 0$. Application of the magnetic field to the substance occurring at this extremum point gives rise to a jump in the entropy, which is determined by the formula [4]

$$\Delta S = (\mu_0/2)H^2\Delta[V\chi(\alpha - \eta)], \quad (16)$$

where α is the isobaric thermal expansion coefficient

$$\alpha = [d\ln(V)/dT]_{P,H}; \quad \eta = -[d\ln(\chi)dT]_{P,H}. \quad (17)$$

As can be readily seen from Eqs. (6) and (7), this extremum of the phase diagram may exhibit a strong dependence of the phase transition temperature on the applied field strength H. This dependence will be more pronounced in the substances possessing greater values of the jumps $\Delta(V\chi)$ and $\Delta[\chi(dV/dH)_{T,P}]$ or a smaller entropy change S according to Eq. (16).

Among all monoatomic substances, a minimum on the $P_f(T)$ curve of melting is observed only for the helium isotopes ^{3}He and ^{4}He [6, 10]. As for the molecular crystals, such a minimum was observed in a series of substances indicated previously [7, 8] and in p-H_2, HD, o-D_2 [11], and BN [12]. All these substances can be expected to show a significant magnetic-field-induced shift in the first-order phase transition temperature.

A critical point of the liquid–gas or crystal–crystal type (existing, e.g., in cerium [6]) corresponds to the second-order phase transition and obeys the conditions

$$\Delta V_0 = 0, \quad \Delta S_0 = 0,$$
$$(dP/dV)_T = 0, \quad (dT/dV)_P = 0.$$

Application of the magnetic field to a substance occurring at a critical point of this type may lead to jumps of molar volume, entropy, and magnetization, as well as to a change in the critical parameters (V_c, P_c, T_c). Assuming that $\Delta\chi = 0$ at this critical point and using Eqs. (3)–(8), one can readily obtain the relationships

$$\Delta V = -(\mu_0/2)H^2V_c\Delta[(d\chi/dP)_{T,H}], \quad (18)$$

$$\Delta S = (\mu_0/2)H^2V_c\Delta[(d\chi/dT)_{P,H}], \quad (19)$$

$$\Delta M = (\mu_0/2)H^2\chi\Delta[(dV/dH)_{T,P}], \quad (20)$$

$$(dP_c/dH)_T = -\{\chi\Delta[(dV/dH)_{T,P}]\}/\{V_c\Delta[(d\chi/dP)_{T,H}]\}, \quad (21)$$

$$(dT_c/dH)_P = -\{\chi\Delta[(dV/dH)_{T,P}]\}/\{V_c\Delta[(d\chi/dT)_{P,H}]\}, \quad (22)$$

$$(dT_c/dP)_H = [\Delta(d\chi/dP)_{T,H}]/[\Delta(d\chi/dT)_{P,H}] \neq 0. \quad (23)$$

As is seen from the last inequality, the condition $\Delta[(d\chi/dP)_{T,H}] = 0$ implies that $\Delta[(d\chi/dT)_{P,H}] = 0$ and vice versa. In this case, neither a shift of the critical parameters (V_c, P_c, T_c) nor a change in the volume magnetostriction can take place at the critical point because $\Delta[(dV/dH)_{T,P}] = 0$. In contrast, when a substance at the critical point is characterized by $\Delta[(d\chi/dP)_{T,H}] \neq 0$, the inequality (23) implies that $\Delta[(d\chi/dT)_{P,H}] \neq 0$ as well. In the case of $\Delta[(dV/dH)_{T,P}] \neq 0$, the application of a magnetic field to this substance at the critical point will lead to the appearance of a critical curve on the P–V–T diagram [3, p. 289]; this curve can be described by Eqs. (18)–(23).

In conclusion, it should be noted that the form of equations derived above is retained in the description of a change in the thermodynamic parameters of the first- and second-order phase transitions in an isotropic substance (not possessing ferroelectric properties) under the action of a homogeneous electric field. It is only necessary to change the notation in all formulas (1)–(23) as follows: $H \longrightarrow E$ (electric field strength); $\mu_0 \longrightarrow \varepsilon_0$ (dielectric constant); $\chi \longrightarrow \chi_e$ (electric susceptibility); and $M \longrightarrow \mathcal{P}$ (molar electric polarizability).

Acknowledgments. the author is grateful to Prof. K.M. Magomedov, K.N. Magomedov, and Z.M. Surkhaeva for their help in this study.

REFERENCES

1. B. M. Yavorskiĭ and A. A. Detlaf, *Handbook of Physics* (Nauka, Moscow, 1971).
2. R. Kubo, *Thermodynamics. An Advanced Course with Problems and Solutions* (North-Holland, Amsterdam, 1968; Mir, Moscow, 1970).
3. I. P. Bazarov, *Thermodynamics* (Vysshaya Shkola, Moscow, 1976).
4. A. R. Ubbelohde, *Melting and Crystal Structure* (Clarendon, Oxford, 1965; Mir, Moscow, 1969).
5. V. S. Shklyar and V. D. Aleksandrov, Zh. Fiz. Khim. **62** (7), 1921 (1988).
6. E. Yu. Tonkov, *Phase Diagrams of Elements under High Pressure* (Nauka, Moscow, 1979).
7. M. N. Magomedov, Zh. Fiz. Khim. **69** (2), 351 (1995).
8. M. N. Magomedov, Zh. Fiz. Khim. **74** (9), 1716 (2000).
9. V. K. Grigorovich, *Mendeleev's Periodic Law and the Electronic Structure of Metals* (Nauka, Moscow, 1966).
10. V. P. Peshkov, Usp. Fiz. Nauk **94** (4), 607 (1968) [Sov. Phys. Usp. **11**, 209 (1968)].
11. Yu. A. Freiman, S. M. Tretyak, A. Jezowski, *et al.*, J. Low Temp. Phys. **113** (5/6), 723 (1998).
12. M. I. Eremets, K. Takemura, H. Yusa, *et al.*, Phys. Rev. B **57** (10), 5655 (1998).

Translated by P. Pozdeev

Technical Physics Letters, Vol. 28, No. 2, 2002, pp. 119–122. Translated from Pis'ma v Zhurnal Tekhnicheskoĭ Fiziki, Vol. 28, No. 3, 2002, pp. 80–87.

Anomalous Microwave Emission from a Stationary Plasma Thruster

K. P. Kirdyashev[a], A. I. Efimov[b], and D. S. Lukin[b]

[a] *Fryazino Branch, Institute of Radio Engineering and Electronics, Russian Academy of Sciences, Fryazino, Moscow oblast, Russia*

[b] *Moscow Physicotechnical Institute (State Technical University), Dolgoprudnyi, Moscow oblast, Russia*

Received September 18, 2001

Abstract—The results of ground radio engineering tests on the thruster modules of a combined power unit for Yamal-100 spacecraft are presented. A pulsed electromagnetic radiation component was detected, which is explained by nonstationary processes of the electron emission from plasma of a hollow compensator cathode. *© 2002 MAIK "Nauka/Interperiodica".*

In connection with the use of stationary plasma thrusters (SPTs) on the Yamal-100 geostationary communication satellite [1], the ground tests included evaluation of the possible SPT contribution to the electromagnetic situation around the spacecraft and the interference immunity of receiving channels of the vehicle-borne radio equipment. As is known, the sources of microwave oscillations and electromagnetic radiation of SPTs in the space radio communication frequency range are concentrated in the ionization zone of the acceleration channel, in the near-wall regions, and in the zone of neutralization of the ejected plasma stream [2, 3].

The radio engineering test on the SPTs revealed a pulsed microwave radiation component leading to spikes in the noise background. The noise amplitude was comparable to the useful signal level at the input of receiving channels of the vehicle-borne radio equipment. Such a pulsed microwave noise component is most dangerous from the standpoint of interference immunity of the vehicle-borne radio equipment receiving and retransmitting digital information on board a communication satellite.

In order to elucidate the situation, we have performed experiments on a ground SPT test system of the ENERGIYA Rocket-Spacecraft Corporation. The experiments employed SPT prototypes analogous to those installed in the spacecraft. The individual modules of a combined power unit were based on an SPD-70 thruster model developed by the FAKEL Design Bureau and were operated in a nominal working regime [1]. In these tests, we studied the conditions and possible mechanisms of excitation of the active pulsed noise in the space communication channels. The purpose was to propose justified SPT operation regimes to provide for an electromagnetic compatibility between the power unit and the vehicle-borne radio equipment. The results of our experiments are of special value for the designers of spacecraft intended for interplanetary flights, possessing a relatively low energy potential of the vehicle-borne radio communication lines [4].

We measured the energy and temporal characteristics of a microwave component of the SPT radiation in the 5.7–6.2 GHz frequency band corresponding to the receiver channel frequencies of the retransmitter employed on board the spacecraft. The radio interference signals accompanying the SPT operation were detected both at the output of the vehicle-borne receiver and by standard measuring receivers. In order to monitor the electromagnetic situation related to the frequency spectrum of intrinsic microwave radiation of the SPT, the noise intensity was simultaneously measured in the 2.0–2.3 and 13–14 GHz frequency bands. The experiments with the vehicle-borne receiver allowed SPT noise variations to be measured at a time resolution of up to 1 μs, which was of special importance from the standpoint of digital data transmission.

Possible changes in the electromagnetic situation over a time period of up to 2 h were determined using the measuring receivers with an output time constant on the order of 0.1 s. Therefore, it was necessary to take into account the smoothening action of the measuring equipment on the radiation spike amplitudes in order to obtain correct estimates of the pulsed microwave component of the SPT radiation. The necessary corrections were made using data on the receiver low-frequency transmission band for a certain duration and repetition rate of the radiation spikes. The absolute values of the spectral density of electromagnetic radiation from the SPT were obtained by a specially developed method of calibration measurements using a standard gas-discharge source of noise [3].

The results of our experiments showed that there are various time scales of nonstationary processes responsible for the generation of microwave oscillations and spurious electromagnetic radiation of the SPT. On the microsecond scale, the microwave radiation envelope

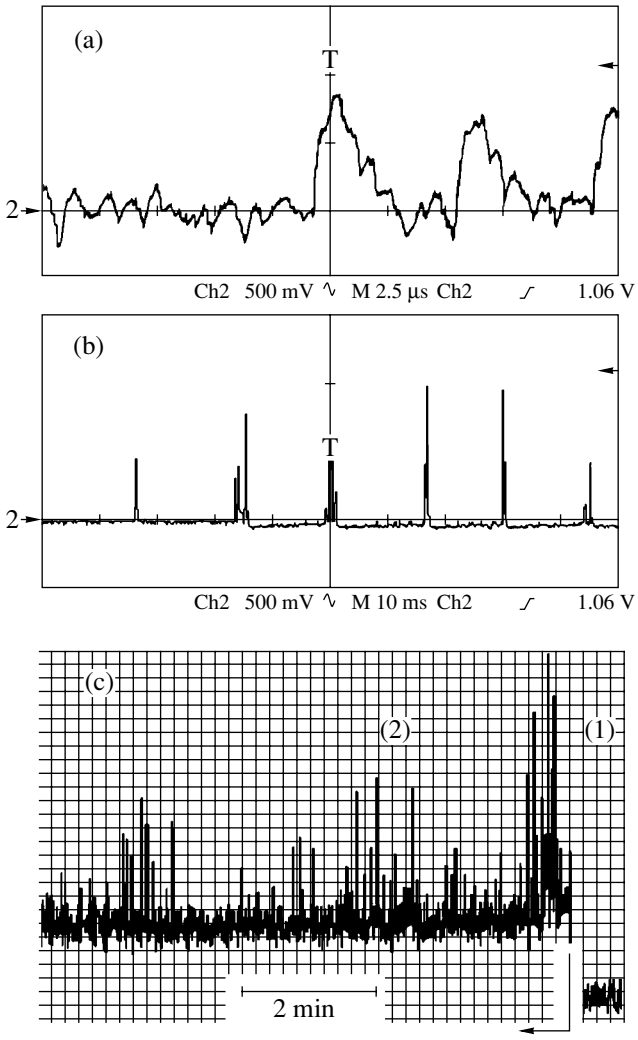

Fig. 1. Envelopes of the spurious microwave radiation from an SPT on various time scales: (a) 25 μs; (b) 100 ms (output signal of a vehicle-borne radio equipment measured by a digital oscillograph); (c) 7.5 min (output signal of a measuring receiver processed by an analog registrator). The arrow indicates the SPT start. Diagrams *1* and *2* show the microwave field intensity in the vacuum chamber of the test setup before and after thruster modulus start, respectively.

represents a limited number of pulses with a duration of up to 1.5–2 μs and a characteristic repetition rate of 10–15 μs (Fig. 1a). It should be noted that the microwave oscillations are predominantly manifested in the SPT regimes with limited electron emission and small gas consumption in the hollow compensator cathode. One of the factors limiting the electron emission in the cathode is the formation of an oxide film on the emitter surface, which was explained by unfavorable technological factors and storage conditions. The presence of such oxide films hinders the electron emission from emitter surface to cathode cavity, increases the cathode potential fall, and gives rise to short-time current spikes 2–5 times the nominal level. This may lead to breakdowns of the discharge regime in the acceleration channel, which requires (according to the technical conditions on the SPT operation) repeated SPT starts.

An characteristic feature was that the microwave radiation pulses appeared almost periodically with a time interval of 10–20 ms (Fig. 1b), which corresponds to the period of the ac current heating the cathode. The observed periodicity in the microwave radiation pulses agrees with the notions about the effect of the magnetic field of the heater current on the electron emission in the cathode region (see, e.g., [5]). According to this concept, the magnetic field of the heater hinders electron emission into the plasma and the microwave generation corresponds to "zeros" of the magnetic field strength. Indeed, for a cathode heater current of 10–12 A and an average potential fall of 20–30 V accelerating the electrons, the magnetic induction amplitude at the heater spiral axis reaches up to 0.005 T and the Larmor radius for electrons amounts to about 2.5 mm, which corresponds to the size of localized plasma regions at the cathode output hole. This mechanism probably accounts for the electrons being "blocked" in the cathode region by the magnetic field of the heater and explains the limited duration of the intensive microwave radiation spikes observed during the SPT test.

It should be noted that the pulsed microwave component is observed on a stationary background related to an equilibrium radiation from the plasma stream ejected from the SPT acceleration channel (Fig. 1c). A nonstationary character of the spurious radiation was previously observed during long-term SPT tests [6]. In our experiments, this effect was manifested in the initial 2-h stage of the test and was different for various cathodes used in the thruster modules. Upon elapse of this time, the pulsed noise generation ceased (Fig. 2) and the SPT began to operate in a regime favorable for the vehicle-borne radio equipment. However, the subsequent SPT starts were also accompanied by the microwave radiation spikes, most typically in the 13–14 GHz frequency band.

As can be seen from the results of our measurements, the intensity of the pulsed microwave radiation component is 6–7 orders of magnitude higher than the equilibrium intensity level, which is evidence of a beam instability development in the SPT plasma, probably with accompanying nonlinear effects. We believe that a source of the microwave radiation in the thruster regimes studied is related to the plasma region localized at the hollow cathode output. This hypothesis was confirmed by the following experimental results and estimates obtained during the SPT test.

The frequency range of microwave oscillations determined from the electromagnetic radiation measurements exceed by far the range of Langmuir oscillations in the acceleration channel and in the ejected plasma stream. Based on the measured discharge current, the cathode output hole size, and the cathode potential fall (20–30 V), the electron concentration at the hollow cathode output can be estimated at 10^{12}–

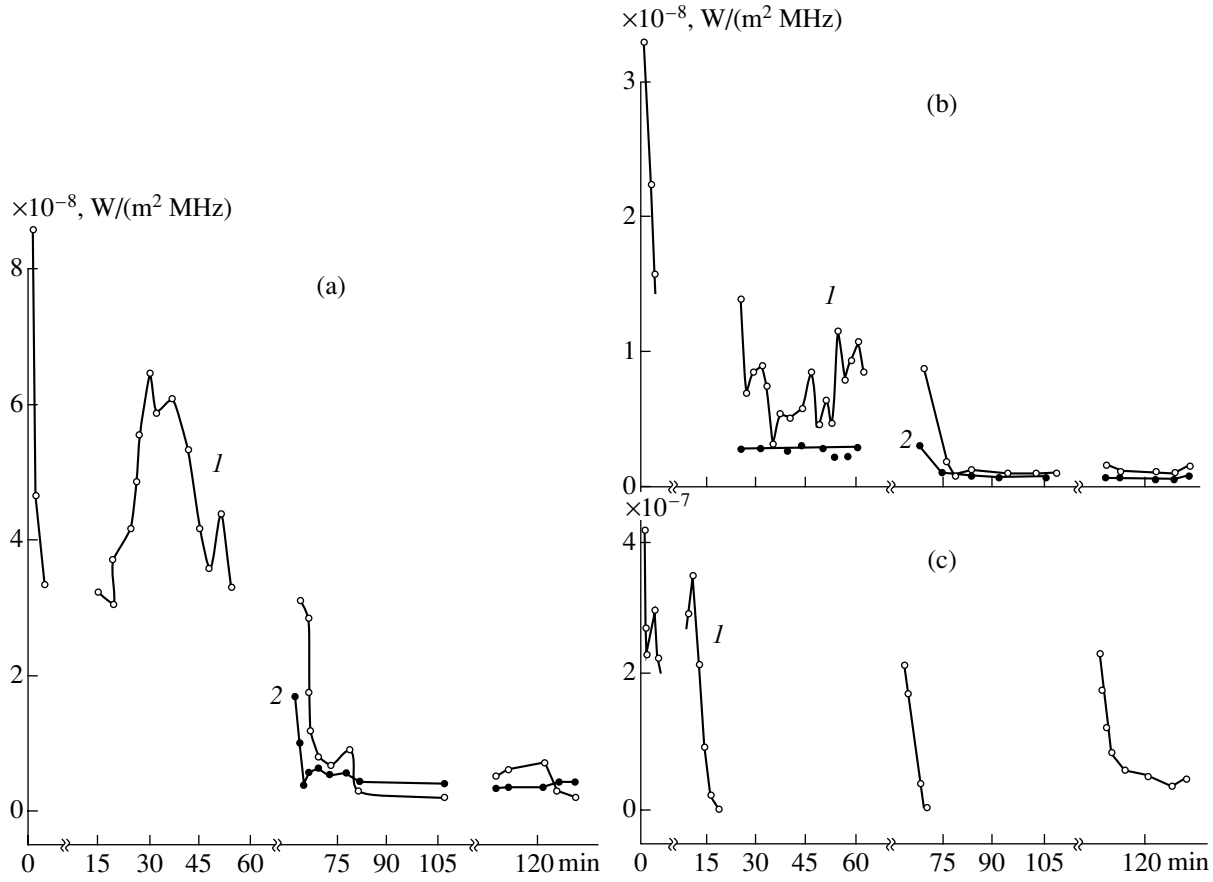

Fig. 2. Time variation of the (*1*) pulsed and (*2*) stationary microwave radiation components in the initial stage of SPT testing. The measurements were performed at a frequency of (a) 5.98, (b) 2.11, and (c) 13.5 GHz.

10^{13} cm^{-3}. This estimate corresponds to a critical electron concentration for the frequency range of the experimentally observed microwave radiation.

The energy and temporal characteristics of the pulsed microwave radiation component agree with the notions about a nonlinear stage of the beam instability development in the cathode region and about the breakdown of oscillations within time intervals corresponding to the Coulomb collision frequency. We proceed from the well-known scenario of the beam instability development in a plasma with electron current, which is accompanied by the process of "thermalization" of the plasma oscillation energy [7, 8] related to the nonlinear effects leading to the transformation of oscillations from longitudinal to transverse with a rapid phase mixing. Apparently, this process is most intense in the regions of "zeros" of the magnetic field generated by the cathode heater.

As is known, the instability development (resulting in that the energy of plasma oscillations reaches the level of the primary energy of accelerated electrons) takes from several tens to hundreds of the oscillations periods. The possibility of such an instability development in the plasma at the hollow cathode output follows from the electric field strength significantly exceeding the critical level $E_D \approx 4.5 \times 10^{-12}(n_e/T_e)$ [9], which is not higher than 10 V/cm. To estimate the field strength in the regime with restricted electron emission into the cathode cavity, let us consider a limiting case when the main cathode fall is concentrated in the region with dimensions on the order of the Larmor radius for electrons in the magnetic field of the cathode heater. Taking the magnetic induction ≤0.001 T (for which the emitted electrons can be injected into the plasma stream), the electric field strength in the cathode regions is estimated at 100–500 V/cm, which significantly exceeds the above critical value.

According to [9], the duration of the electron acceleration is determined by the time interval between two sequential electron–ion collisions, which amounts to 5×10^{-6} to 10^{-5} s. This time also determines the repetition period of the microwave pulses corresponding to "zeros" of the magnetic field strength. Note that, under conditions of the localized plasma region formation at the cathode output, the electron–ion collisions determine the characteristic times of the plasma instability development. Indeed, the ratio of the effective frequency of the electron–ion collisions to that of the electron–neutral collisions is $\nu_{ei}/\nu_{em} \sim 10^{-2} T_e^2 (n_e/n_m) \geq 10$

(here, n_e and n_m are the concentrations of electrons and neutrals at the cathode output).

Acknowledgments. The authors are grateful to N.N. Sevast'yanov and A.V. Shestakov for the problem formulation and permanent interest in this study. Many thanks to V.A. Belov, V.A. Blinov, V.E. Vishnekov, A.G. Orlov, I.V. Smirnov, I.A. Frolov, and the staff of ENERGIYA that participated in the preparation and conduction of the experiment. Special thanks to A.I. Morozov for fruitful discussions of the experimental results.

This study was supported by GAZKOM Joint-Stock company and the ENERGIYA Rocket-Spacecraft Corporation.

REFERENCES

1. G. Popov, V. Kim, V. Murashko, *et al.*, in *Proceedings of the 3rd International Conference on Spacecraft Propulsion, Cannes, 2000,* ESA SP-2000, p. 21.
2. K. P. Kirdyashev and A. I. Morozov, Fiz. Plazmy **25** (4), 326 (1999) [Plasma Phys. Rep. **25**, 293 (1999)].
3. K. P. Kirdyashev, *High-Frequency Wave Processes in Plasmadynamic Systems* (Énergoatomizdat, Moscow, 1982), p. 142.
4. K. P. Kirdyashev, Radiotekhnika, No. 8, 70 (1998).
5. A. I. Morozov, K. P. Kirdyashev, A. I. Bugrova, *et al.*, Fiz. Plazmy **27** (7), 620 (2001) [Plasma Phys. Rep. **27**, 582 (2001)].
6. V. I. Brukhtiĭ, K. P. Kirdyashev, V. I. Zarembo, *et al.*, Zh. Tekh. Fiz. **66** (2), 68 (1996) [Tech. Phys. **41**, 149 (1996)].
7. S. D. Fanchenko, B. A. Demidov, N. I. Elagin, *et al.*, Zh. Éksp. Teor. Fiz. **46** (2), 497 (1964) [Sov. Phys. JETP **19**, 337 (1964)].
8. E. A. Sukhomlin, V. A. Suprunenko, N. I. Reva, *et al.*, in *High-Frequency Properties of Plasma, Series: "Plasma Physics and Controlled Nuclear Fusion Problems"* (1965), pp. 126–133.
9. N. Drieser, Phys. Rev. **117** (2), 329 (1960).

Translated by P. Pozdeev

Technical Physics Letters, Vol. 28, No. 2, 2002, pp. 123–125. Translated from Pis'ma v Zhurnal Tekhnicheskoĭ Fiziki, Vol. 28, No. 3, 2002, pp. 88–94.

The Effect of Light Entrainment Observed in an Optical Disk Interferometer

V. O. Gladyshev, T. M. Gladysheva, and V. E. Zubarev

Egor'evsk Civilian Aviation Technical College, Egor'evsk, Moscow oblast, Russia

e-mail: vgladyshev@mail.ru

Received July 30, 2001

Abstract—We observed a spatial effect of the light entrainment at a wavelength of $\lambda = 0.63299$ μm by an optical disk with a radius of $R_0 = 0.06$ m rotating at a frequency of $\omega = 25$ Hz. A relative shift of the interference pattern, monitored by the time of the interference band motion across the aperture of a photodetector for the disk rotating in the opposite directions, amounts to $\Delta = 0.0094 \pm 0.0025$ of the interference bandwidth. © *2002 MAIK "Nauka/Interperiodica".*

The propagation of electromagnetic radiation in a rotating medium is determined by superposition of the primary wave and the secondary waves appearing as a result of the interaction of the electromagnetic radiation with atoms of the moving medium. By solving a dispersion equation, it is possible to determine the radiation wavevector in any local region of the trajectory with allowance for spatial distribution of the medium velocity [1]. The solution was repeatedly verified in experiment, but the complexity of such investigations allowed only certain particular cases to be studied such as the longitudinal Fizeau effect [2, 3] and the normal velocity break [4, 5], in which the light beam is affected by either normal or tangential components of the medium velocity.

Propagating in a rotating medium, an electromagnetic wave is simultaneously affected by both normal and tangential components of the motion. Therefore, experimental observation of the spatial effect of the light wave entrainment is verification for the total solution of the dispersion equation.

Below we present the results of a series of experiments on the measurement of a shift of the light interference pattern in the scheme of a double-beam two-pass disk interferometer (Fig. 1). In this scheme, the light beam from laser *1* incident on a beam divider *2* was split into two beams. These beams entered the optical disk *3* to be reflected from flat mirror surfaces. The exit beams reflected from angle prism *4* changed paths, passed through the optical disk in the reverse direction, and entered the divider again. Mixed on the divider mirror, the beams passed through an objective lens *5* to display the interference pattern on a screen. The light intensity was measured by photodetector *6* situated at the center of the screen (a photodiode of the FD256 type operating in the generator mode).

The light source was an LGN-302 laser operating at $\lambda = 0.63299$ μm and producing the beam with a power of $P_0 \approx 0.84$ mW for both horizontal and vertical polarization components. The rotating medium was a disk with a diameter of 120 mm and a thickness of 30 mm made of an LK5 grade glass ($n = 1.4766$ for $\lambda = 0.63299$ μm). In order to increase the optical pathlength by multiple reflections, the disk edge surfaces were mirror coated so as to provide for the reflection coefficient $R = 0.9$.

Reversal of the disk rotation direction resulted in inversion of the sign of the phase shift between interfering light beams and, accordingly, of the direction of the

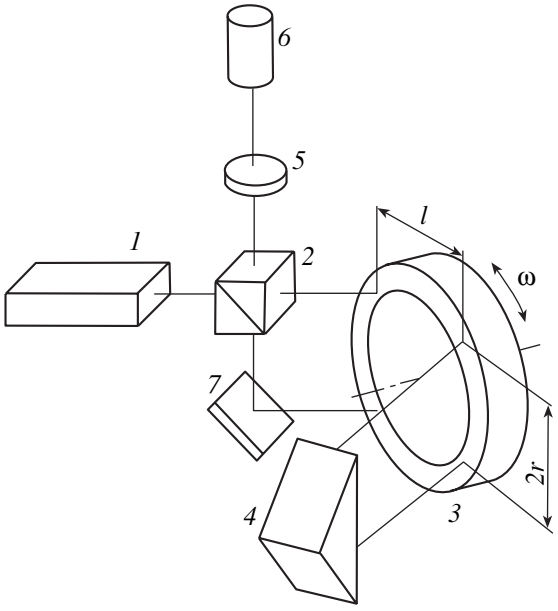

Fig. 1. A schematic diagram of the interferometer with rotating disk. In order to increase the optical pathlength in the rotating medium, a reflecting coating was deposited onto the disk front central part and rear flat edge surfaces.

1063-7850/02/2802-0123$22.00 © 2002 MAIK "Nauka/Interperiodica"

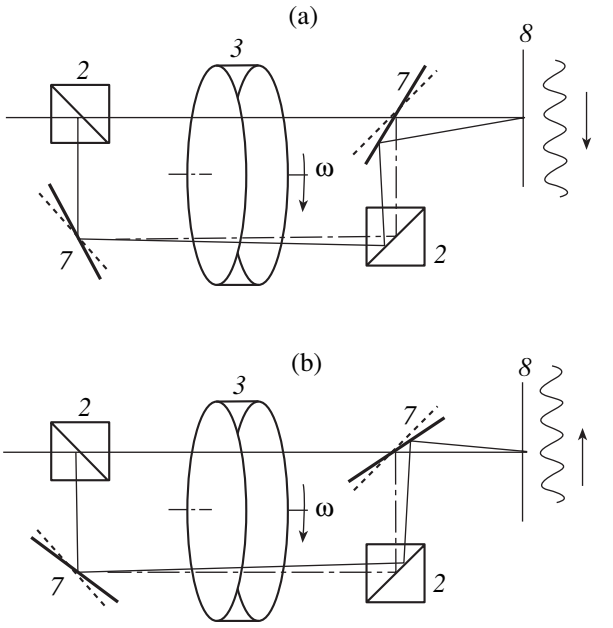

Fig. 2. A schematic diagram of the beam path from divider *2* to screen *8* for different positions of mirror *7* in the scheme of Fig. 1. A change in the mutual arrangement of the interfering beams results in (a) downward or (b) upward shift of the interference pattern for the disk rotating in the same direction.

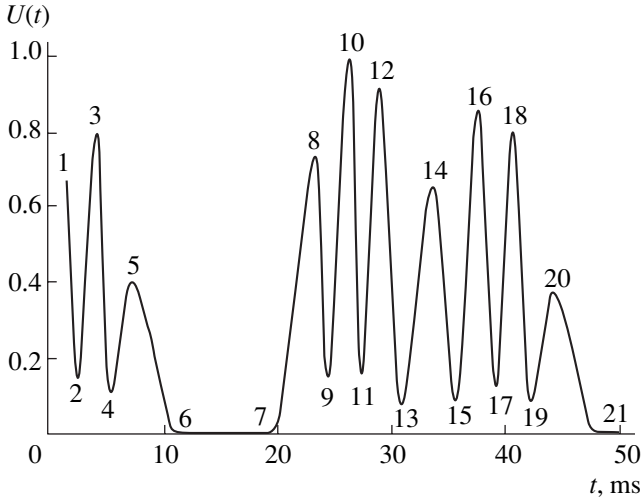

Fig. 3. Time variation of the relative photodetector output signal voltage.

shift of the interference pattern. Since the optical scheme is such that the interfering light beams travel by the same path, the interferometer is not sensitive to vibrations, stationary displacements, elastic deformations, or wedge distortions of the disk.

At the same time, the observed shift of the interference pattern is influenced by the photoelastic effect, which can also change magnitude depending on the disk rotation velocity and direction. In order to exclude this factor, we performed several series of experiments with the disk rotating in the forward and reverse direction for various mutual arrangement of the beams (Fig. 2), which was provided by adjusting the position of mirror *7*. For the disk rotating in one direction, the photoelasticity phenomenon led to a shift of the interference patterns in the same direction, while the spatial light entrainment effect shifted the interference patterns in opposite directions for the alternating relative beam positions.

By adjusting the mirrors and beam divider, it was possible to obtain an interference pattern in the form of contrast parallel fringes of equal inclination. The rotation of the disk produced a shift of the interference bands, whereby three interference bands passed across the photodetector aperture first in one and than in the reverse direction. A shift of the interference pattern related to the phase shift of the interfering light beams (caused by the spatial entrainment effect or by the photoelasticity phenomenon), rather than to the kinematic motion of the disk, has to change the time period between the interference band passages across the photodetector aperture depending on the direction of rotation.

Figure 3 shows the time variation of the photodetector output voltage for the optical disk rotating clockwise and the mutual arrangement of beams such as those depicted in Fig. 2. These patterns were obtained using oscillograms recorded by an S1-118A oscillograph with the temporal instability of sweep not exceeding $0.02(T + 4) \times 10^{-9}$ s, where T is the sweep duration. The oscillograms were digitized with the aid of a Kodak DC240 camera possessing a resolution of 1344×971 pixel. The time coordinates of the points in the oscillogram were determined graphically on a Pentium II PC. The distance between points 13 and 15 in Fig. 3 in various series of measurements corresponded to a conditional time interval t_{15}–$t_{13} \approx$ 800–1000 pixel.

As can be seen from Fig. 3, the region of points 14 and 6, 7 correspond to a moment when the interference pattern shift is suspended (band stop) and the direction of rotation is reversed. This was checked in the regime of manual disk rotation at a 1° step. The signal amplitude difference between points 8 and 20, 10 and 18, and 12 and 16 is explained by rotation of the interference bands, whereby different parts of the same band passed across the photodetector aperture in the forward and reverse directions.

A deviation of the rotation period T_i in each series of measurements, which was monitored by the difference of coordinates between the identical points 3 and 18, 4 and 19, or 5 and 20, did not exceed 0.5% of the stationary value. The experimentally measured quantities were the coordinates t_{13}, t_{15} and t_{12}, t_{16} determining the width, relative position, and shift of the interference band.

In a nonrelativistic limit, a shift of the interference pattern in the scheme employed is given by the formula

$$\Delta = \frac{4lu_l(n^2-1)}{\lambda c}, \quad (1)$$

where l is the projection of the light beam pathlength in the optical beam on the flat edge surface, $u_l = \omega r$ is the projection of the medium velocity onto the l direction, ω is the disk rotation frequency, and r is the distance from the line l to the axis of the disk rotation. For the parameters employed in our experiments (l = 0.087 m, r = 0.0225 m, n = 1.4766, ω = 25 Hz, and λ = 0.63299 μm), formula (1) yields a theoretical estimate for the band shift relative to the immobile disk: Δ = 0.001217.

The method of determining a shift of the interference pattern using variations of the time of the interference band passage across the photodetector aperture significantly increases the experimental accuracy. First, the shift of the interference pattern is measured for the disk rotating in opposite directions, which leads to a twofold increase in the measured Δ value. Second, the experimentally measured quantity t_{15}–t_{13} represents a doubled shift value. Third, the measurements are conducted for various mutual arrangements of the interfering beams, which results in a shift of the interference pattern in opposite directions for the same rotation direction, which also increases the resulting shift of the interference pattern by a factor of 2. Thus, the experiment is expected to give the value $\Delta_p = 8\Delta = 0.0097$ of the bandwidth.

The experimental series included the measurement of $U(t)$ curves at a resolution sufficient for which the t_{12}–t_{16} part of the pattern to fall within each shot; 25 shots were made for each of the two directions of disk rotation and each mutual arrangement of the interfering beams. The quantity $\Delta t_i = t_{13,i} - t_{12,i} + t_{16,i} - t_{15,i}$ gives the time width of the interference band ($i = \overline{1, 25}$). The quantity $\delta t_i = t_{15,i} - t_{13,i}$ determines the time position of the band relative to the instant of band stop at point 14 for a given direction of rotation and mutual arrangement of the beams. The ratio of these values determines the relative position of the interference pattern expressed in fractions of the bandwidth, which eliminates the possible period variations from shot to shot. After calculating the time coordinates δt_i and Δt_i, we determined the relative spatial coordinates characterizing the interference band positions and widths δx_i and Δx_i, respectively.

The relative position of an interference band closest to the instant of band stop at point 14 corresponds to

$$\Delta_i = \frac{\delta x_i}{\Delta x_i}. \quad (2)$$

Upon averaging over 25 shots, we obtain four quantities determining the required shift of the interference band:

$$\Delta_\ni = (\Delta_+^1 - \Delta_-^1) - (\Delta_+^2 - \Delta_-^2), \quad (3)$$

where the subscripts 1 and 2 refer to two different mutual arrangements of the interfering light beams and the signs "+" and "–" refer to the clockwise and counterclockwise directions of rotation, respectively.

The experimental data processing yielded the following value for the relative shift of the interference pattern (at confidence probability of 0.9):

$$\Delta_\ni = 0.0094 \pm 0.0025 \text{ bandwidth.}$$

As can be seen, the above Δ_p value falls within the confidence interval. The results of calculations performed for the given incidence angle ($\vartheta_0 = 67°$) rotation frequency (ω = 25 Hz), disk radius (R_0 = 0.06 m), and refractive index (n = 1.4766), a deviation from Snell's law due to the transverse light entrainment would lead to a shift of the interference pattern about ten times as small as the $\Delta_\ni$ value [6]. The level of sensitivity necessary for the observation of this effect can be provided by increasing ω and/or R_0.

It should be noted that formula (1) was derived assuming that a shift of the interference pattern is determined by the projection of the linear velocity vector of the medium onto the electromagnetic wavevector at each point of a three-dimensional light beam trajectory. The results of our experiments confirmed the validity of this approach. Further increase in the interferometer sensitivity will allow us to study the deviations from formula (1) related to a violation of the law of refraction and to a deviation of the light from rectilinear trajectory in a rotating medium.

REFERENCES

1. V. O. Gladyshev, Pis'ma Zh. Éksp. Teor. Fiz. **58** (8), 593 (1993) [JETP Lett. **58**, 569 (1993)].
2. D'H. Fizeau, Ann. Chim. Phys. **57**, 385 (1959).
3. A. Michelson and E. W. Morley, Am. J. Phys. **31** (185), 377 (1986).
4. O. G. Zagorodnov, Ya. B. Faĭnberg, and A. M. Egorov, Zh. Éksp. Teor. Fiz. **38** (1), 7 (1960) [Sov. Phys. JETP **11**, 4 (1960)].
5. B. M. Bolotovskiĭ and S. N. Stolyarov, Usp. Fiz. Nauk **159** (1), 155 (1989) [Sov. Phys. Usp. **32**, 813 (1989)].
6. V. O. Gladyshev, Zh. Tekh. Fiz. **69** (5), 97 (1999) [Tech. Phys. **44**, 566 (1999)].

Translated by P. Pozdeev

Technical Physics Letters, Vol. 28, No. 2, 2002, pp. 126–128. Translated from Pis'ma v Zhurnal Tekhnicheskoĭ Fiziki, Vol. 28, No. 4, 2002, pp. 1–6.

Contact Stability of C_{60} Molecules on Pure and Doped (100) Tungsten Surface

N. R. Gall', E. V. Rut'kov, and A. Ya. Tontegode

Ioffe Physicotechnical Institute, Russian Academy of Sciences, St. Petersburg, 194021 Russia

e-mail: gall@ms.ioffe.rssi.ru

Received September 25, 2001

Abstract—The influence of the metal surface doping on the contact stability of adsorbed fullerene molecules at room temperature was observed for the first time. The C_{60} fullerene molecules decompose at room temperature both on a pure (100)W surface and on a tungsten surface containing carbide (WC), while the presence of a surface silicide of the same stoichiometry (WSi) produces passivation of the metal surface, thus preventing the fullerene molecules from decomposition. © *2002 MAIK "Nauka/Interperiodica".*

The laws of interaction between fullerenes and solids play a key role in any application of these highly interesting molecules in physical technologies. Among the most important stages of this interaction are the initial steps and, in particular, the contact stability of C_{60} molecules adsorbed on the solid surface. It was found that C_{60} molecules, while adsorbing without decomposition on silicon and on many transition metals [1, 2], decompose already at room temperature on the surface of tungsten. It was therefore important to study whether this effect can be suppressed by doping the metal surface with some foreign atoms.

Experimental methods. The experiments were performed in an ultrahigh vacuum (UHV) chamber ($P \sim 1 \times 10^{-10}$ Torr) of a high-resolution ($\Delta E/E \sim 0.1\%$) Auger electron spectrometer with a prism electron energy analyzer [3]. The samples were prepared from thin tungsten ribbons cut to $1 \times 0.02 \times 40$ mm, which were thoroughly purified from impurities by high-temperature heating in an oxygen atmosphere and under UHV conditions. The tungsten ribbon texture was characterized for more than 99.5% by a (100) crystal orientation. The sample surface was homogeneous with respect to the electron work function, which amounted to $e\varphi = 4.65$ eV.

The fullerene molecules were deposited onto the sample surface in UHV from a Khudsen cell with an absolutely calibrated flux. The doping impurities (carbon or silicon) were injected from special sources generating cluster-free flows of C and Si atoms [4]. The absolute atomic flow densities were determined as described elsewhere [5, 6].

Sample surface doping. In order to provide for reproducible surface doping conditions, we employed a method of forming the surface compounds tungsten carbide and silicide [5, 7]. When silicon atoms are deposited onto a tungsten surface at 1110–1400 K, all Si atoms striking the metal surface are retained until reaching a certain surface concentration N^* and all Si atoms deposited above this level are dissolved in the bulk. The N^* value depends neither on the temperature nor on the other deposition conditions. This parameter reflects the formation of a special compound—a surface silicide with the composition WSi and the adsorbed silicon concentration $N^* = 1 \times 10^{15}$ cm^{-2}. This surface silicide is stable at $T < 1400$ K, and the stoichiometric composition is independent of the total amount of silicon dissolved in the bulk [5]. A surface carbide with the composition WC is formed in a similar manner and characterized by the same concentration of adsorbed species [7].

Results and discussion. The transformation of C_{60} molecules upon adsorption was studied by monitoring the shape of the C*KVV* Auger line recorded at high resolution. It was found that C_{60} molecules are characterized by a special shape of this Auger line, observed at an energy of 269 eV (Fig. 1, spectrum *1*), differing from the shapes of analogous signals from all other types of the surface carbon such as graphite films, carbides, and chemisorbed clusters. This characteristic line shape is observed for C_{60} molecules in deposited films with a thickness of several tens of molecular layers—and the same shape is characteristic of the fullerenes adsorbed on the (100) surface of silicon, where fullerene molecules were reported to occur in a nondeformed state [1]. We used the shape and energy of this line as qualitatively indicating whether the C_{60} molecules retain their structure upon adsorption on a solid surface.

Adsorption of the fullerene molecules on a pure tungsten surface at 300 K was accompanied by partial decomposition of the adsorbate, as manifested by the Auger line significantly shifted (by ~ 2 eV) in energy

and a top part noticeably modified in shape (Fig. 1, spectrum *2*). Rather unexpectedly, the formation of a surface silicide on (100)W was found to inhibit decomposition of the C_{60} molecules at temperatures up to 750 K. Formed on tungsten with the dopant (silicon) concentration $N_{Si} = 1 \times 10^{15}$ cm^{-2}, the surface silicide covers no more than 25% of the metal surface and, as it might seem at first glance, can hardly prevent the adsorbed fullerene molecules from contacting with surface atoms of the metal substrate. It is interesting to note that a surface carbide, formed instead of silicide on tungsten with the same surface concentration of the nonmetal dopant (carbon), does not protect the adsorbed fullerene molecules from decomposition proceeding as if the metal surface were pure.

Taking into account quite close physicochemical properties of the surface carbide and silicide, including isoelectron and isostructural characteristics as well as the ability of entering into competition and forming mixed surface compounds, this result is rather intriguing. Apparently, this behavior is related to complex, still incompletely clear quantum-chemical differences in the electron structures of pure and doped metal surfaces.

A possible explanation of the observed effects is based on the concept of a mechanical blocking of the metal surface with respect to the contact between fullerene molecules and tungsten atoms. The adsorbed silicon atoms are capable of hindering the close chemical contact between C_{60} molecules and the surface atoms of tungsten, thus preventing the fullerene from transformation as a result of the adsorbate–substrate interaction. Indeed, proceeding from the structural considerations (Fig. 2), we may suggest that large spherical C_{60} molecules adsorbed on a (100)W surface bearing the surface silicide layer cannot approach the metal atoms to distances characteristic of the chemical contact. On the contrary, this possibility seems to be retained when the silicide is replaced by the surface carbide, apparently because the diameter of the carbon atom is only about half that of the silicon atom. Of course, this rough estimation ignores the surface reconstruction accompanying the formation of surface compounds but, in all probability, the reconstruction is not very significant in the system under consideration [8].

The observed influence of the surface doping on the contact stability of adsorbed fullerene molecules probably is of a rather general nature. It will be interesting to study whether the tungsten surface will be passivated with respect to the fullerene decomposition upon the formation of surface compounds with other adsorbates such as sulfur, oxygen, and phosphorus.

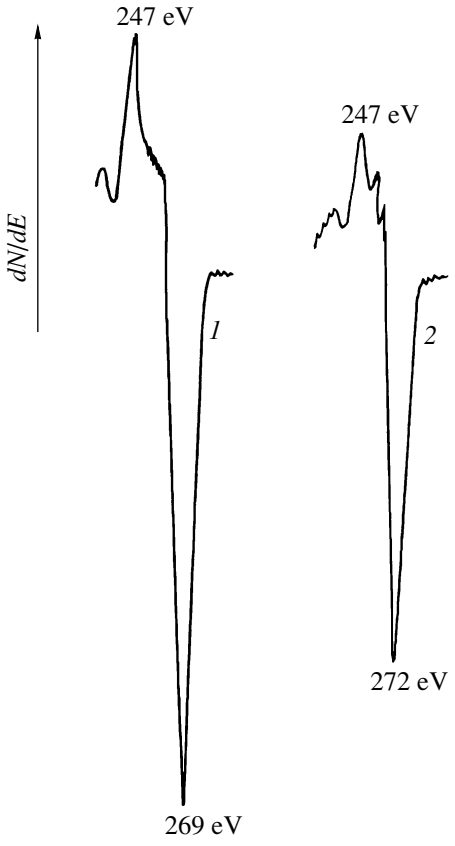

Fig. 1. The high-resolution C*KVV* Auger electron spectra of C_{60} molecules adsorbed at 300 K on different substrates: (*1*) a multilayer film on (100)Si; (*2*) a monolayer film on pure (100)W.

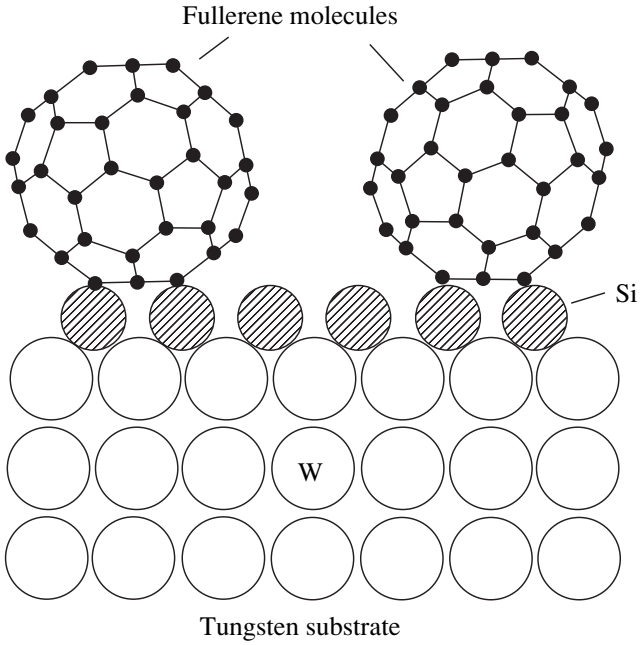

Fig. 2. A schematic diagram showing C_{60} fullerene molecules adsorbed over a surface silicide layer on tungsten.

Acknowledgments. This study was supported by the "Low-Dimensional Quantum Structures" Program of Basic Research of the Russian Academy of Sciences.

REFERENCES

1. E. A. Katz, in *Abstracts of the International Workshop on Fullerenes and Atomic Clusters (IWFAC-2001), St. Petersburg, 2001* (Fiz.-Tekh. Inst. im. A. F. Ioffe, Ross. Akad. Nauk, St. Petersburg, 2001), p. 18.
2. E. V. Rut'kov, A. Ya. Tontegode, and M. M. Usufov, Fullerene Sci. Technol. **6** (4), 721 (1998).
3. N. R. Gall, S. N. Mikhailov, E. V. Rut'kov, and A. Ya. Tontegode, Surf. Sci. **191**, 185 (1987).
4. N. R. Gall, E. V. Rut'kov, A. Ya. Tontegode, *et al.*, Chem. Vap. Deposition **6** (7), 72 (1997).
5. V. N. Ageev, E. Yu. Afanas'eva, N. R. Gall', *et al.*, Poverkhnost, No. 5, 7 (1987).
6. N. R. Gall, E. V. Rut'kov, and A. Ya. Tontegode, Int. J. Mod. Phys. B **11** (16), 1865 (1997).
7. N. R. Gall', E. V. Rut'kov, and A. Ya. Tontegode, Izv. Akad. Nauk, Ser. Fiz. **62** (10), 1980 (1998).
8. D. G. Kelly, M. Salmeron, and G. A. Somorjai, Surf. Sci. **175** (3), 465 (1986).

Translated by P. Pozdeev

Technical Physics Letters, Vol. 28, No. 2, 2002, pp. 129–130. Translated from Pis'ma v Zhurnal Tekhnicheskoĭ Fiziki, Vol. 28, No. 4, 2002, pp. 7–11.

The Effect of Wearless Friction in Aluminum–Tin and Aluminum–Lead Alloys

T. A. Shakhnazarov and Yu. A. Takhtarova

Institute of Physics, Dagestan Scientific Center, Russian Academy of Sciences, Makhachkala, Dagestan, Russia

e-mail: kamilov@datacom.ru

Received May 24, 2001; in final form, August 16, 2001

Abstract—The conditions favoring stable manifestations of the wearless friction in aluminum–tin and aluminum–lead antifriction alloys were studied. Special features of this phenomenon in the alloy systems studied are determined and the prospects for practical application of this effect are estimated. © *2002 MAIK "Nauka/Interperiodica".*

The phenomenon of wearless friction offers an example of dissipative structure formation under conditions of thermomechanical action, whereby the shear stresses in the surface layer of a material sharply decrease and the deformation process is not accompanied by accumulation of defects. The wearless friction effect was studied sufficiently well in the case of a selective transfer taking place in some special lubricant media, providing for the formation of a protective copper film on the friction surface. The cases of wearless friction were also thoroughly studied in various lubricating media for the steel–copper alloy couples in which no such protective films are formed [1].

Recently [2] we have demonstrated that a stable dissipative process involved in the wearless friction phenomenon, which is just what provides for the external force action being spent predominantly for the plastic deformation of the surface metal layer, is developed due to the kinetic phase transition to a more ordered regime of deformation. Below we demonstrate the possibility of the wearless friction manifestations in aluminum–tin and aluminum–lead alloys, which were previously never considered among the systems featuring this phenomenon.

The process of deformation of a surface metal layer during friction proceeds by the dislocation–vacancy mechanism [3], which provides for the intensive interaction and scattering of dislocations with the formation of a large number of vacancies continuously disappearing from the surface layer. Stability of the wearless friction effect is related to the stable operation of this dislocation–vacancy mechanism of deformation of the surface layer. Alloys of the aluminum–tin and aluminum–lead systems are susceptible to the formation of a surface oxide layer on the friction surface [4], which impedes emergence of the continuously formed dislocations at the surface, thus hindering realization of the dislocation–vacancy mechanism and the wearless friction effect.

We have studied conditions favoring stable manifestations of the wearless friction in aluminum–tin and aluminum–lead alloys, determined special features of this phenomenon in the systems studied, and estimated prospects for the practical application of this effect.

The experiments were performed in air and in an inert gas atmosphere on an SMTs-2 friction test machine operating in the boundary lubricating regime. An aluminum–tin alloy of the AO20-1 grade was obtained by a conventional melting technology, while the aluminum–lead alloy (containing 20 wt % Pb and 1 wt % Cu) was prepared by the chemical dispersion technique [5]. The inert atmosphere was represented by argon or nitrogen. The tests were conducted on alloy samples weighing about 10 g. The intensity of wear was evaluated by weighing the samples before and after the test. Before the test, the samples were lapped under conditions close to the main test regime. The quality of lapping was evaluated by stabilization of the friction force moment. The duration of lapping in air was about 1 h, while the same process in an inert atmosphere required about 3 h. The main test duration was initially about 6 h and above, but then the time was reduced to 2 h for each loading regime. The range of applied loads was selected taking into account the conditions of real alloy operation in internal combustion engines.

The results of our experiments are presented in Figs. 1 and 2. As can be seen from these data, the intensity of wear for the aluminum–tin (Fig. 1) and aluminum–lead (Fig. 2) alloys decreases by an order of magnitude in an inert gas atmosphere as compared to that in air. This fact, as well as a longer time required for the preliminary lapping in the former medium, indicate that friction in the inert atmosphere leads to removal of the oxide film and provides for the free escape of vacancies from a near-surface layer, thus ensuring deformation of this layer without accumulation of defects. Therefore, a sharp decrease in the intensity of wear and a stably low wear level maintained in the system (with a linear wear

1063-7850/02/2802-0129$22.00

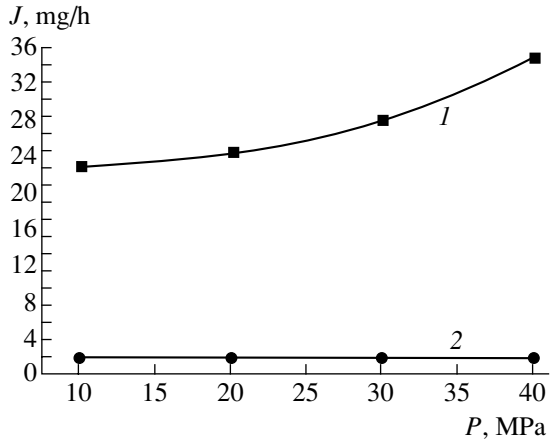

Fig. 1. The plots of wear intensity versus specific load for an Al–20% Sn alloy tested in (*1*) air and (*2*) an inert atmosphere.

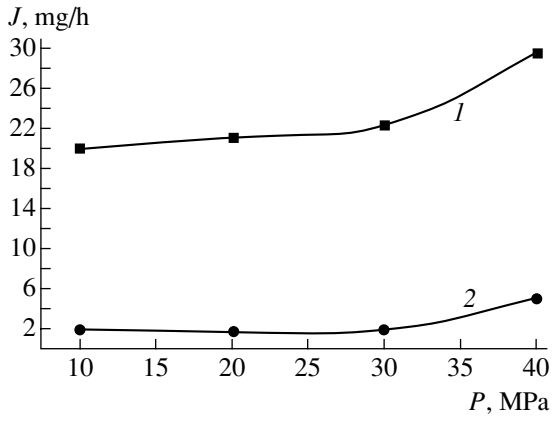

Fig. 2. The plots of wear intensity versus specific load for an Al–20% Pb alloy tested in (*1*) air and (*2*) an inert atmosphere.

intensity amounting to 10^{-10} [6]) in a broad range of applied loads are indicative of the wearless friction manifestations.

The ability of the surface layers of copper-containing alloys to deform without fracture so as to maintain the wearless friction conditions was explained [1] by the presence of a porous structure that provides for a large number of degrees of freedom for the bending and rotational deformation modes. According to this concept, the porous structure formation was related to special features of the lubricating medium. In the case of heterophase alloys of the aluminum–tin and aluminum–lead systems, in contrast to the copper-based antifriction alloys, the friction process leads to the formation of a surface layer containing only the "soft" alloy component (i.e., tin and lead, respectively). Indeed, according to the results of the electron-microscopic investigations [4], the plastic crystals of tin and lead form the basis of the surface layer formed during friction.

Lazarev *et al.* [7] described the deformation of solids on a microscopic level within the framework of a quantum-statistical model and estimated the structural stability of crystals loaded in the "pressure plus shear" scheme. According to this model, the crystal lattice loses stability when the external action reaches a certain level, after which the system passes into a strongly nonequilibrium coherent state. With respect to the character of this transition, the materials can be divided into "brittle" and "plastic." In the plastic materials, the above transition is accompanied by the formation of a dissipative structure characterized by the plastic deformation proceeding in a hydrodynamic regime. This process is essentially a transition to a more ordered state with decreasing entropy. The "brittleness–plasticity" transition can be described by a parameter R [7], the threshold value of which is $R = 1.0$. In particular, this parameter for lead is $R = 0.650$. This implies that lead—and, by analogy, tin—must pass to the hydrodynamic regime of plastic deformation, thus providing for a stable deformation of the surface layer during the wearless friction process.

A sharp decrease in the intensity of wear (Figs. 1 and 2) was observed in both argon and nitrogen atmosphere. In the final stage of experiments, we attempted to create the nitrogen atmosphere in the test chamber with the aid of selective membranes. The results showed that this approach offers a simple, reliable, and promising way to realize the wearless friction in internal combustion engines.

REFERENCES

1. V. P. Bulatov and O. F. Kirienko, Probl. Mashinostr. Nadezhnosti Mashin, No. 2, 56 (1991).
2. T. A. Shakhnazarov, G. M. Ataev, and Yu. A. Takhtarova, in *Proceedings of the International Conference, Makhachkala, 2000*, p. 166.
3. A. A. Polyakov, Vestn. Mashinostr., Nos. 6–7, 17 (1992).
4. T. F. Markova and F. O. Muktepavel, Izv. Akad. Nauk Latv. SSR, Ser. Fiz.-Tekh. Nauk, No. 4, 65 (1982).
5. T. A. Shakhnazarov and S. S. Shikhamirov, Izv. Akad. Nauk, Met., No. 2, 23 (1995).
6. *Friction, Wear and Lubrication: Handbook* (Mashinostroenie, Moscow, 1978), Vol. 1.
7. V. B. Lazarev, A. S. Balankin, A. D. Izotov, *et al.*, *Structural Stability and Dynamic Strength of Inorganic Materials* (Nauka, Moscow, 1993).

Translated by P. Pozdeev

Technical Physics Letters, Vol. 28, No. 2, 2002, pp. 131–133. Translated from Pis'ma v Zhurnal Tekhnicheskoĭ Fiziki, Vol. 28, No. 4, 2002, pp. 12–18.

Instability of the Charged Surface of an Electrolyte Film on an Ice Electrode Melting as a Result of the Joule Heat Evolution

A. I. Grigor'ev and V. V. Morozov

Yaroslavl State University, Yaroslavl, Russia

e-mail: grig@uniyar.ac.ru

Received May 11, 2001; in final form, August 28, 2001

Abstract—We have studied the formation of a liquid electrolyte film as a result of melting caused by the Joule heat evolution on the surface of an ice core at the end of a capillary by which the electrolyte containing a substance to be analyzed is supplied to the discharge system of a mass spectrometer. It is shown that the characteristic thickness of this film is ~1 μm and the radius of curvature at the tip of the emitting protrusion (formed due to realization of the film instability with respect to the surface charge) is ~10 nm, which provides for the intensive field evaporation of clustered and stripped ions from the protrusion tip. © *2002 MAIK "Nauka/Interperiodica".*

Introduction. The initial stage of the ion beam formation in the mass spectrometry of nonvolatile and thermally unstable organic substances (usually of biological origin) employs the phenomenon of electrohydrodynamic dispersion of the sample solution in a weak electrolyte [1–4]. The charged surface of this liquid is subject to the development of instability. As a result, small, strongly charged drops of the sample solution and clusters containing several sample molecules are emitted from the tips of emitting protrusions formed at the final stage of the instability development. The further evolution of the emitted drops and clusters is accompanied either by leakage of the excess charge, by realization of the film instability with respect to its own charge, or by the field evaporation of small ion clusters [2, 4–6].

The charged clusters can be ejected directly from the tip of an emitting protrusion formed on the free surface of the solution, provided the curvature of the protrusion tip is sufficiently large [7, 8]. The curvature of the tip of the emitting protrusion also affects the size of drops emitted during the instability development and, hence, influences the subsequent evolution of these drops. Depending on the initial radius and viscosity, a drop can either decay as a result of emission of a large number of very small (radius $R \le 0.1$ μm) but strongly charged droplets or divide into two parts of comparable size [4, 9].

In this context, it was of interest to study the formation of such emitting protrusions in mass spectrometers operating at low temperatures, that is, under the conditions when an aqueous sample solution may freeze at the end of a capillary supplying the solution to the discharge system. The emission of drops and clusters proceeds from the surface of a thin solution film formed on the ice surface as a result of the Joule heat evolved during the discharge current passage. The thickness of this film would naturally influence the geometry (i.e., the height and the curvature radius) of the emitting protrusion formed as a result of the electrohydrodynamic instability development [10, 11].

The purpose of this study was to describe, within the framework of an idealized model, the process of a liquid film formation due to melting of the ice surface under the action of heat that evolved as a result of the current passage.

Model description. Consider an ice plate (comprising a frozen aqueous NaCl solution) with a length a, width b, and thickness h in contact with a thermostat at a temperature of T_0. The surrounding medium (vacuum) is bounded at a large distance by walls occurring at the same temperature T_0. At the initial time instant ($t = 0$), the upper surface of the plate, bearing a solution film of negligibly small thickness ξ_0, is connected to a source of current with the internal resistance r and the emf ε in the direction of x axis (Fig. 1). The current passing through the electrolyte leads to a heat evolution according to Joule's law. We assume that the heat Q liberated per unit time of the current passage through the electrolyte be spent for (i) a radiative heat exchange between the free solution film surface and the surrounding medium according to the Stefan–Boltzmann law, (ii) a conductive heat transfer in depth of the ice plate, and (iii) the melting of ice. Let us describe variation of the melted electrolyte layer thickness ξ as a function of time $\xi = \xi(t)$ and determine the liquid film thickness in the stationary state $\xi = \xi(\infty) = \lim_{t \to \pm\infty} \xi(t)$, assuming the thermal properties of the electrolyte to be unchanged and the heat of the phase transition κ to be known. In order to simplify the considerations, we will assume that the temperature of the electrolyte film is indepen-

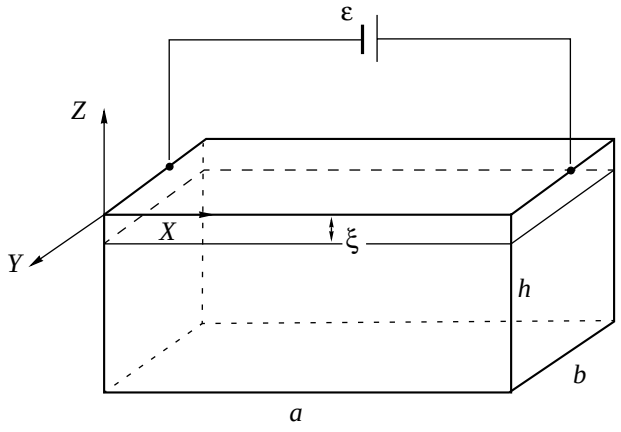

Fig. 1. A model of icicle melting as a result of Joule's heat evolution.

dent of the thickness and retains a constant value equal to the phase transition temperature T_*.

A mathematical model of the above process can be written in the form of a thermal balance equation

$$q = \sigma T_*^4 + \lambda_a \frac{T_* - T_0}{h - \xi} + \rho_e \kappa \frac{d\xi}{dt} \quad (1)$$

with the initial condition

$$\xi(0) = \xi_0 \approx 0, \quad (2)$$

where $q = \dfrac{Q}{ab}$ is the heat flow from the internal source (Joule's heat evolution) through the ab area per unit time, Q is the heat source power, $\dfrac{d\xi}{dt}$ is the rate of the electrolyte film thickness variation, λ_a is the heat conductivity of ice, ρ_e is the electrolyte density, and σ is the Stefan–Boltzmann constant.

Stationary solution. Using Joule's and Ohm's laws, we readily obtain an expression for the heat flux q:

$$q = \frac{Q}{ab} = \frac{\gamma}{a^2} \frac{\varepsilon\xi}{\left(\gamma\dfrac{a}{b} + r\xi\right)^2},$$

where γ is the electrolyte resistivity. Using this expression Eq. (1) can be written as follows:

$$\frac{\gamma}{a^2} \frac{\varepsilon\xi}{\left(\gamma\dfrac{a}{b} + r\xi\right)^2} = \sigma T_*^4 + \lambda_a \frac{T_* - T_0}{h - \xi} + \rho_e \kappa \frac{d\xi}{dt}. \quad (3)$$

Putting $\dfrac{d\xi}{dt} = 0$ in Eq. (3), we obtain a relationship for the stationary electrolyte film thickness:

$$\frac{\gamma}{a^2} \frac{\varepsilon\xi}{\left(\gamma\dfrac{a}{b} + r\xi\right)^2} = \sigma T_*^4 + \lambda_a \frac{T_* - T_0}{h - \xi}.$$

In a zero-order approximation with respect to the ξ/h ratio, this relationship yields a quadratic algebraic equation for the stationary solution film thickness,

$$\xi^2 + 2\left(\gamma\frac{b}{ar^2} - \frac{\gamma\varepsilon^2}{2a^2r^2\left(\sigma T_*^4 + \lambda_a\dfrac{T_* - T_0}{h}\right)}\right)\xi + \gamma^2\frac{b^2}{a^2r^2} = 0,$$

the solutions to which are as follows:

$$\xi_1 \approx \frac{\gamma\varepsilon^2}{a^2r^2\left(\sigma T_*^4 + \lambda_a\dfrac{T_* - T_0}{h}\right)} - 2\gamma\frac{b}{ar^2};$$

$$\xi_2 \approx \gamma\frac{b^2\left(\sigma T_*^4 + \lambda_a\dfrac{T_* - T_0}{h}\right)}{\varepsilon^2}. \quad (4)$$

The second root has no physical sense within the framework of our problem, since this value corresponds to the film thickness growing with increasing heat loss and decreasing ε, which can hardly be realized in practice. The value of the first root will be estimated for the following parameters: $a = b = 100$ μm; $\gamma = 0.06$ Ω m; $\Delta T = 200$ K; $T_* = 273$ K; $h = 100$ μm; $r = 10^6$ Ω; $\varepsilon = 1000$ V; $\lambda_a = 2.2$ W/(m K); and $\rho_e = 1040$ kg/m^3. Here, the characteristic linear dimensions were selected so as to correspond to a typical diameter of the capillaries used to supply the sample solutions to the discharge system of a mass spectrometer. Accordingly, the other values were also selected so as to correspond to the ion–cluster beam formation in a mass spectrometer. Substituting the above values into the expression for ξ_1, we obtain $\xi_1 \approx 1.4$ μm ($\xi_2 \approx 2.6 \times 10^{-3}$ μm).

Time-dependent solution. Now let us determine the time variation of the electrolyte film thickness. Integrating Eq. (3) with the boundary condition (2), we obtain

$$t = F_2 \ln\left|1 - \frac{\xi}{\xi_2}\right| - F_1 \ln\left|1 - \frac{\xi}{\xi_1}\right| - \frac{N}{G}\xi;$$

$$F_1 = \frac{1}{G(\xi_1 - \xi_2)}(K + M\xi_1 - 2DN\xi_1 - AN);$$

$$F_2 = \frac{1}{G(\xi_1 - \xi_2)}(K + M\xi_2 - 2DN\xi_2 - AN);$$

$$K = \rho_e\kappa\gamma^2\frac{b^2}{a^2}; \quad M = 2\rho_e\kappa\gamma\frac{b}{a}r; \quad N = r^2\rho_e\kappa; \quad (5)$$

$$G = r^2\left(\sigma T_*^4 + \frac{T_* - T_0}{h}\right);$$

$$D = \frac{1}{2}\left(2\gamma\frac{b}{ar^2}G - \frac{\gamma}{a^2}\varepsilon^2\right); \quad A = \gamma^2\frac{b^2}{a^2r^2}G,$$

where ξ_1 and ξ_2 are given by formulas (4).

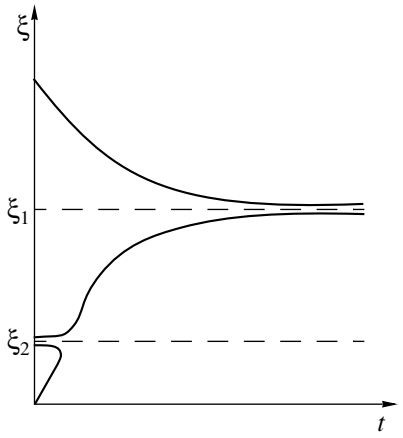

Fig. 2. A qualitative time variation of the melted film thickness.

The function determined by formula (5) is transcendental, nonperiodic, and monotonic (i.e., exhibits no extrema). A plot of this function has two asymptotes: $\xi(+\infty) = \xi_1$ and $\xi(-\infty) = \xi_2$ (Fig. 2).

Discussion. The development of instability in a thin film with respect to its own surface charge in an external electric field leads to the formation of emitting protrusions by superposition of shortwave modes [10, 12]. The experiments [10, 13] with an electric discharge in an inhomogeneous electrostatic field showed the formation of an emitting protrusion in the form of a soliton on the surface of a melting icicle. The soliton formed in the region of a weak field, propagated in the direction of increasing field strength, and stopped on arriving at the point of maximum field strength, after which a discharge in the form of a diffuse glow was initiated at the soliton tip. The soliton height was greater by at least one order of magnitude as compared to the liquid film thickness.

An analogous situation takes place in the ion source of a mass spectrometer, where a discharge also occurs at the surface of a melting icicle and it can be naturally expected that the emitting protrusion would be of a soliton shape. Within the framework of our analysis, it would be of interest to estimate the radius of curvature of the soliton tip because this value determines the field strength in the vicinity of the discharge initiation site (i.e., in the vicinity of the point of emission of strongly charged droplets and clusters).

According to [14], an analytical expression describing the shape of a soliton with the height H formed in a layer of liquid with the thickness h is as follows:

$$y = H\operatorname{sech}^2\left\{\sqrt{\frac{3H}{2h}}\frac{\xi}{h}\right\},$$

where $\xi = \xi(x, t) = x - Vt$ and V is a constant (having the dimensionality of velocity). The radius of curvature r at the soliton tip is given by the formula

$$r = \left[\sqrt{1 + \left(\frac{dy}{d\xi}\right)^2}\Big/\frac{d^2y}{d\xi^2}\right]_{\xi = 0} \equiv \left(\frac{d^2y}{d\xi^2}\right)^{-1}_{\xi = 0} \equiv \frac{h^3}{3H^2}.$$

Taking $\frac{h}{H} \sim 0.1$, we readily obtain an estimate of $r \sim 10^{-2}h$. For the conditions in a mass spectrometer ($h \approx 1$ μm), this yields $r \sim 10$ nm. Thus, even for $\varepsilon = 100$ V the field strength at the emitting protrusion tip will reach ~10 V/nm, which implies intensive field evaporation of both stripped and clustered ions [2, 5, 6]. The size of strongly charged droplets that can be also ejected from the tip of the emitting protrusion [9] are on the order of the curvature radius: $R \sim 10$ nm. According to [5], such a drop will also lose the charge as a result of the field evaporation of clustered and stripped ions.

Conclusion. Formed on the surface of thin liquid films unstable with respect to the surface charge, the tips of the emitting protrusions possess a characteristic radius of curvature sufficiently small to generate an electric field with a strength of up to ~10 V/nm, which gives rise to intensive field evaporation of stripped ions and ion clusters.

REFERENCES

1. D. S. Simons, Int. J. Mass Spectrom. Ion Processes **15** (3), 291 (1974).
2. N. B. Zolotoĭ, G. V. Karpov, and V. E. Skurat, Zh. Tekh. Fiz. **58** (2), 315 (1988) [Sov. Phys. Tech. Phys. **33**, 193 (1988)].
3. J. B. Fenn, M. Mann, Chin Kai Meng, *et al.*, Science **246** (4926), 64 (1989).
4. S. O. Shiryaeva and A. I. Grigor'ev, Zh. Tekh. Fiz. **63** (8), 162 (1993) [Tech. Phys. **38**, 715 (1993)].
5. A. I. Grigor'ev, Pis'ma Zh. Tekh. Fiz. **27** (4), 52 (2001) [Tech. Phys. Lett. **27**, 155 (2001)].
6. A. I. Grigor'ev, Pis'ma Zh. Tekh. Fiz. **27** (7), 89 (2001) [Tech. Phys. Lett. **27**, 305 (2001)].
7. N. B. Zolotoĭ, Zh. Tekh. Fiz. **65** (11), 159 (1995) [Tech. Phys. **40**, 1175 (1995)].
8. N. B. Zolotoĭ and G. V. Karpov, Dokl. Akad. Nauk **348** (3), 336 (1996).
9. A. I. Grigor'ev and S. O. Shiryaeva, Izv. Akad. Nauk, Mekh. Zhidk. Gaza, No. 3, 3 (1994).
10. A. I. Grigor'ev, I. D. Grigor'eva, and S. O. Shiryaeva, J. Sci. Exploration **5** (2), 163 (1991).
11. A. I. Grigor'ev, M. I. Munichev, and S. O. Shiryaeva, J. Colloid Interface Sci. **166**, 267 (1994).
12. D. F. Belonozhko, A. I. Grigor'ev, and S. O. Shiryaeva, Zh. Tekh. Fiz. **68** (10), 27 (1998) [Tech. Phys. **43**, 1160 (1998)].
13. A. I. Grigor'ev, Pis'ma Zh. Tekh. Fiz. **11** (16), 1004 (1985) [Sov. Tech. Phys. Lett. **11**, 415 (1985)].
14. E. N. Pelinovskiĭ, in *Nonlinear Waves. Propagation and Interaction: Collection* (Nauka, Moscow, 1981), pp. 187–202.

Translated by P. Pozdeev

Technical Physics Letters, Vol. 28, No. 2, 2002, pp. 134–138. Translated from Pis'ma v Zhurnal Tekhnicheskoĭ Fiziki, Vol. 28, No. 4, 2002, pp. 19–27.

The Initiation, Termination, and Evolution of Nonparaxial Optical Vortices: High-Order Singular Beams

A. V. Volyar and T. A. Fadeeva

Tauric National University, Simferopol, Crimea, Ukraine

Received March 27, 2001; in final form, June 26, 2001

Abstract—Exact solutions to the scalar Helmholtz wave equation describing nonparaxial high-order mode beams are considered. To match these solutions to those of the parabolic wave equation, soft approximate boundary conditions are formulated. According to these conditions, in the paraxial limit $kz_0 \gg 1$, paraxial and nonparaxial wave beams transform into each other either far off the focal caustic (at $z \gg z_0$) or near it. The behavior of the mode beams with different azimuthal and radial mode indices is described. © *2002 MAIK "Nauka/Interperiodica".*

The possibility of a paraxial transformation of the wave functions describing high-order paraxial and nonparaxial mode beams was mentioned as early as in the 1970s and 1980s [1–5]. However, a more detailed analysis revealed that this problem has no evident solutions. In particular, Sheppard and Saghafi [6] pointed out that this relationship cannot be derived by simple methods.

Nevertheless, we have recently demonstrated that the paraxial transformation can be derived for slightly reformulated approximate boundary conditions: the nonparaxial beams have to be matched to eigenmodes of the optical fiber only near the waist plane (where the input of the optical guide is located) [7]. This matching of the free-space and fiber modes indicates that we can use a somewhat softer formulation of the approximate boundary conditions according to Davis [8]. On the other hand, paraxial mode beams cannot be represented in terms of unit wave fields satisfying the Helmholtz wave equation; nor can their combination be used to obtain the paraxial correspondence along the whole optical axis because of the difference in topological phases [9].

The purpose of this work was to study features of the high-order nonparaxial optical beams and to determine conditions for the transformation of these beams into their paraxial counterparts.

Let us consider the scalar Helmholtz wave equation

$$(\nabla^2 + k^2)\Psi = 0. \tag{1}$$

The solution to Eq. (1) can be written as [1, 2]

$$\Psi_m^{(l)} = A_m^{(l)} P_m^{(l)}(\cos\theta) j_m(kR) \begin{pmatrix} \cos l\varphi \\ \sin l\varphi \end{pmatrix}, \tag{2}$$

where $P_m^{(l)}(\cos\theta)$ are the associated Legendre polynomials, $j_m(kR)$ are the mth order spherical Bessel function of the first kind, $R = \sqrt{x^2 + y^2 + (z + iz_0)^2}$ is the complex radius, $\cos\theta = \dfrac{(z + iz_0)}{R}$, $A_m^{(l)}$ is the normalization factor, k is the wavenumber, and φ is the azimuthal angle.

Let us require that, in the paraxial approximation $kz_0 \gg 1$, a superposition of wave functions (2) of a nonparaxial singular beam would transform into the wave function of a paraxial beam:

$$\tilde{\Psi}_p^{(q)} = \mathcal{R}^l L_p^{(q)}(2|\mathcal{R}|^2)\frac{1}{\xi}\exp(-\mathcal{R}^2)\begin{pmatrix} \cos q\varphi \\ \sin q\varphi \end{pmatrix}, \tag{3}$$

where $\mathcal{R}^2 = \dfrac{r^2}{\tilde{\rho}^2\xi}$, $\xi = 1 - i\dfrac{z}{z_0}$, $r^2 = x^2 + y^2$, and generalized Laguerre polynomials have the form

$$L_p^{(q)}(2|\mathcal{R}^2|) = p!\sum_{s=0}^{p}(-1)^s\binom{p+q}{p-s}\frac{1}{s!}2|\mathcal{R}|^{2s}. \tag{4}$$

The associated Legendre polynomials appearing in wave function (2) can be written as

$$P_m^l(\mu) = \frac{(2m)}{2^m m!(m-l)}(1-\mu^2)^{\frac{1}{2}l}$$

$$\times\left\{\mu^{m-l} - \frac{(m-l)(m-l-1)}{2(2m-1)}\mu^{m-l-2}\right. \tag{5}$$

$$\left. + \frac{(m-l)(m-l-1)(m-l-2)(m-l-3)}{2\times 4(2m-1)(2m-3)}\mu^{m-l-4} - \ldots\right\},$$

where $\mu = \cos\theta = \dfrac{(z + iz_0)}{R}$.

1063-7850/02/2802-0134$22.00 © 2002 MAIK "Nauka/Interperiodica"

The above expressions show that not all partial solutions (2) to Eq. (1) can be used to construct the required wave function (3). The matter is that the associated Legendre polynomials (5) are expressed in terms of the argument $(\cos\theta)^{m-l-2N}$, whereas the argument of the Laguerre polynomials (4) contains the variable $\left(\frac{r}{w}\right)^2 \propto \left(\frac{r}{R}\right)^2 = \sin^2\theta$. Hence, to construct the wave function of a combined beam, we should use such indices l and m that allow us to express the Legendre polynomials (5) in terms of $\sin\theta$. These indices must satisfy the wave function selection condition: $2p + l = m$ and $l = q$. This fact substantially restricts the spectrum of nonparaxial beams satisfying the chosen boundary conditions. The latter relationship ($l = q$) is nothing but the conservation law for the topological charge in a point-focused singular beam.

Let us expand the beam complex radius R into a power series in terms of $\frac{r^2}{(z + iz_0)^2}$:

$$R = \sqrt{r^2 + (z + iz_0)^2} \approx z + iz_0 + (1/2)r^2/(z + iz_0). \quad (6)$$

On substituting R into the Bessel functions, it is a usual practice [7] to retain two terms of the Taylor expansion (6) of the complex radius R in the arguments of trigonometric functions, while only the first term $R \approx z + iz_0$ is retained in the denominator. Then, in the paraxial asymptotics, we obtain

$$Aj_m(kR) \approx i^m \tilde{\Psi}_0^{(0)}(r, z, z_0), \quad A = \frac{kz_0}{\sinh(kz_0)} \quad (7)$$

for the whole optical axis. It should be noted that these relationships are well satisfied even for relatively small values of the beam waist radius: $kz_0 \geq 10$ or $z_0 \geq 1$ μm.

The above expressions enable the direct comparison of a superposition of the associated Legendre polynomials and the generalized Laguerre polynomials. For "nonsymmetric" wave functions, arguments of the Legendre polynomials must be real quantities. This condition is satisfied with rather good accuracy in the following regions: (i) in a small part of optical axis located near the waist plane $z = 0$ at $z + iz_0 \approx i\left(\frac{k\rho}{2}\right)w = i\left(\frac{k\rho}{2}\right)\rho\sqrt{1 + \frac{z^2}{z_0^2}}$ and (ii) in a substantial part of the optical axis at $z \gg z_0$, where $z + iz_0 \approx \pm aw = \frac{z}{|z|}aw$ ($a = \sqrt{\frac{kz_0}{2}}$). The approximations obtained for the complex radius can be treated as two types of the soft boundary conditions.

Let us write now the wave function of a nonparaxial beam as

$$\Psi_{2p+q}^{(q)} = \sum_{l'=0}^{q}\sum_{m=0}^{2p+q} C_m^{(l')} P_m^{(l')}(\cos\theta) j_m(kR)\begin{Bmatrix}\cos l'\varphi \\ \sin l'\varphi\end{Bmatrix} \quad (7a)$$

and require that the approximate identity would be valid:

$$\tilde{\Psi}_p^q(x, y, z, z_0) \cong \Psi_{2p+l}^l(x, y, z, z_0)\big|_{kz_0 \gg 1}. \quad (8)$$

Below, we consider several cases important in practice.

1. Let $l = 0$ and p be an even number. Using approximate identity (8) and expression (7), we consider the boundary conditions of the first type for the mode matching in the waist plane. For example, $p = 1$. Then $L_1^{(0)} = 1 - 2\frac{r^2}{w^2}$, $P_0^{(0)} = 1$, and $P_2^{(0)} = -\frac{1}{2}\left(2 - 3\frac{r^2}{R^2}\right)$. From identity (8), we find coefficients $C_0 = 1 - C_2$ and $C_2 = \frac{2}{3}kz_0$.

Figure 1 presents distributions of the field intensity, amplitude, and phase corresponding to the wave function of this nonparaxial beam. It should be noted that, for relatively small Rayleigh lengths $kz_0 < 5$, the height of the second maximum becomes comparable to that of the principal maximum. Moreover, the principal zero has different coordinates in the nonparaxial and paraxial beams. As the Rayleigh length increases ($kz_0 > 5$), the intensity and phase distributions in the nonparaxial beam rather closely fit to the intensity and phase profiles of the Laguerre–Gauss beam.

2. Let l and p be odd numbers, for example, $p = 1$ and $l = 1$. Using identity (8) and the approximate boundary conditions of the second kind, we obtain $L_1^{(1)} = -2\left(1 - \frac{r^2}{w^2}\right)$, $P_1^{(1)} = \frac{r}{R}$, and $P_3^{(1)} = -\frac{3}{2}\frac{r}{R}\left(4 - 5\frac{r^2}{R^2}\right)$. Then, the wave function coefficients are given by

$$C_1^{(1)} = i2\frac{z}{|z|}a\left(1 - \frac{12}{15}a\right), \quad C_3^{(1)} = i\frac{4}{15}\frac{z}{|z|}a^3.$$

Figure 2 illustrates evolution of the amplitude profile of this wave function.

3. Now, let l and p be an odd and even number, respectively: for example, $l = 1$ and $p = 2$. We solve this problem for the approximate boundary conditions of the first type and consider the beam matching near the

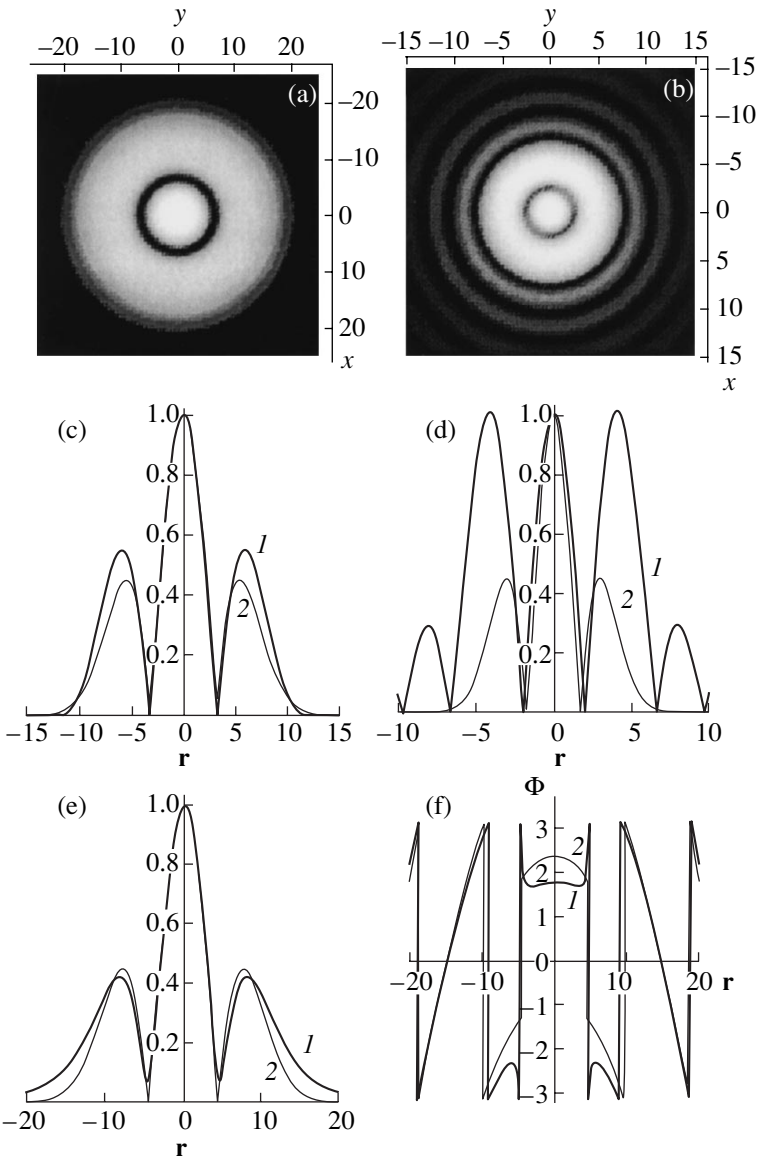

Fig. 1. Distributions of (a, b) intensity, (c, d, e) amplitude, and (f) phase in the (curve *1*) nonparaxial mode beam and (curve *2*) similar Laguerre–Gauss paraxial beam for mode indices (d, e) $m = 1$, $l = 0$ and $m = 2$, $l = 0$: (a, c) $kz_0 = 3$ and $kz = 0$; (b, e, f) $kz_0 = 10$ and $kz = 10$; (d) $kz_0 = 10$ and $kz = 0$. The amplitude of wave function is measured in arbitrary units. In all figures, spatial coordinates are measured in the wave number units $k = \frac{2\pi}{\lambda}$. The plots in Figs. 1 and 2 were calculated using expressions (2), (3), and (7a) with the coefficients $C_m^{(l)}$ corresponding to examples 1, 2, and 3.

waist plane. Then we have

$$L_2^{(1)} = 4\left(\frac{r}{w}\right)^4 - 12\left(\frac{r}{w}\right)^2 + 6,$$

$$P_5^{(1)} = \frac{21}{8}\frac{r}{R}\left\{5 - 40\left(\frac{r}{R}\right)^2 + 15\left(\frac{r}{R}\right)^4\right\},$$

$$C_1^{(1)} = -i6\frac{z}{|z|}a\left(1 - \frac{5}{2}a^2 + 2a^4\right),$$

$$C_3^{(1)} = -i2\frac{z}{|z|}a^3\left(1 - \frac{8}{9}a^2\right), \quad C_5^{(1)} = -\frac{z}{|z|}\frac{32}{315}a^5.$$

It should be noted that, as indices p and l increase, the discrepancy between the results obtained using the paraxial and nonparaxial approaches increases. This is manifested by the fact that curves *1* and *2* (Fig. 2c–2f) corresponding to the nonparaxial (curve *1*) and paraxial (curve *2*) cases almost coincide with each other at rather large distances from the waist (Fig. 2e) for small

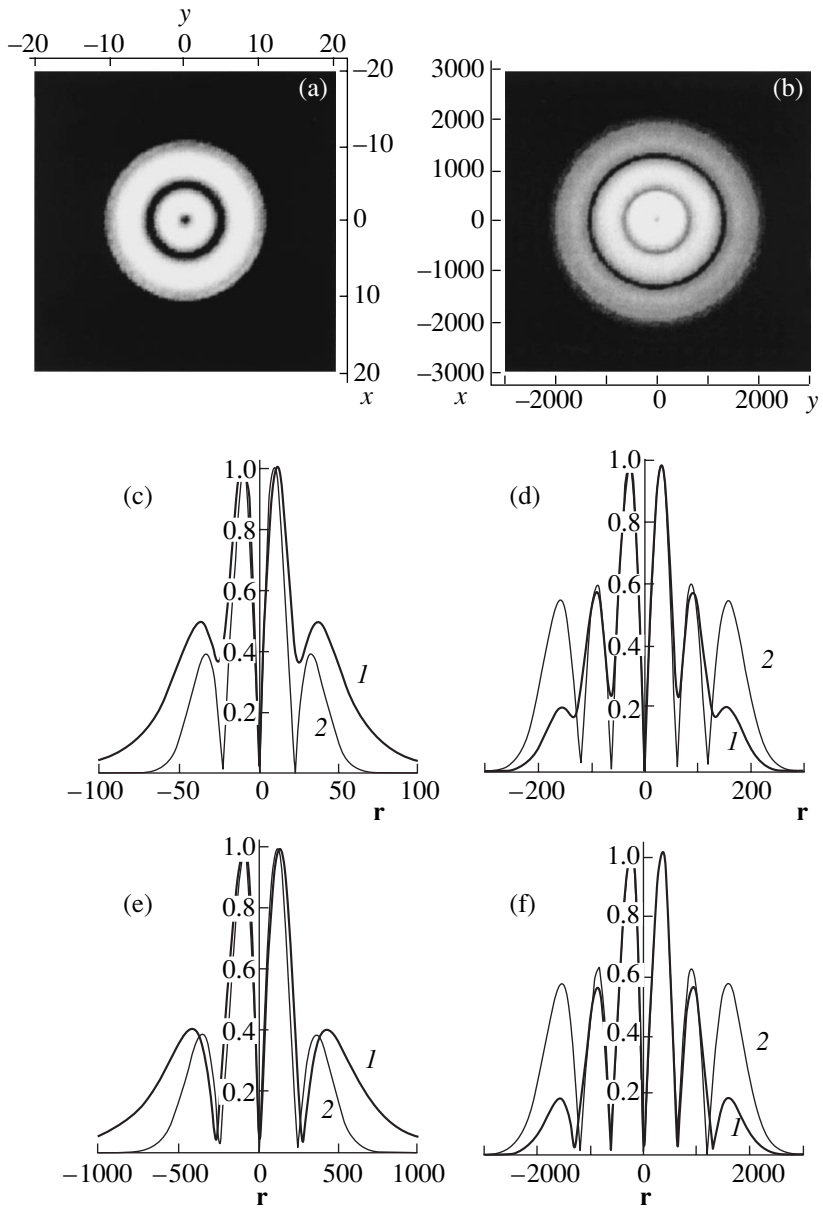

Fig. 2. Distributions of (a, b) intensity, (c, d, e) amplitude, and (f) phase in the (curve *1*) nonparaxial and (curve *2*) paraxial singular mode beams carrying optical vortices with mode indices (a, c, e) $m = 1$, $l = 1$ and (b, d, f) $m = 2$, $l = 1$: (a) $kz_0 = 10$ and $kz = 0$, (b) $kz_0 = 30$ and $kz = 3000$, (c) $kz_0 = 10$ and $kz = 50$, (d) $kz_0 = 30$ and $kz = 300$, (e) $kz_0 = 10$ and $kz = 550$, (f) $kz_0 = 30$ and $kz = 3000$.

mode indices ($l = p = 1$). At the same time the discrepancy between beam profiles increases near the focal plane (Fig. 2c), where profiles of the mode beams with higher indices agree rather poorly. This fact is clearly demonstrated in Fig. 2d, where a partial correspondence between beams with $p = 2$ and $l = 1$ can only be noticed from coinciding coordinates of zeros in their intensity distributions. In order to obtain a good correspondence between beams with higher mode indices, we should move away from the focal plane at a sufficiently large distance ($kz \gg kz_0$) ranging from several hundred to several thousand wavelengths (Fig. 2f). Note that, for $kz_0 > 50$, the degree of correspondence between paraxial and nonparaxial beams becomes almost independent of the Rayleigh length.

In conclusion, we can note that, due to the mode dispersion of the optical beam states, elementary beams involved in the wave function possess different phase velocities along the *z* axis. Therefore, we can obtain a rigorous correspondence between the paraxial and nonparaxial wave functions only within small segments of the optical axis. To all appearances, there is no method based on linear transformations that would allow matching the paraxial and nonparaxial beams in the entire space.

Acknowledgments. This work was supported by the United States Air Force Research Laboratory under project P-051 through the European Office of Aerospace Research and Development (EOARD).

REFERENCES

1. L. B. Felsen, J. Opt. Soc. Am. **66** (8), 751 (1976).
2. A. E. Siegman, J. Opt. Soc. Am. **63** (9), 1093 (1973).
3. S. Y. Shin and L. B. Felsen, J. Opt. Soc. Am. **67** (5), 699 (1977).
4. M. Coutare and P. A. Belanger, Phys. Rev. A **24** (1), 355 (1981).
5. E. Zauderer, J. Opt. Soc. Am. B **3** (4), 465 (1986).
6. C. Sheppard and S. Saghafi, Phys. Rev. A **57** (4), 2971 (1998).
7. A. V. Volyar, V. G. Shvedov, and T. A. Fadeeva, Opt. Spektrosk. **90** (1), 104 (2001) [Opt. Spectrosc. **90**, 93 (2001)].
8. L. W. Davis, Phys. Rev. A **19** (3), 1177 (1979).
9. A. V. Volyar, T. A. Fadeeva, and V. G. Shvedov, Pis'ma Zh. Tekh. Fiz. **25** (5), 87 (1999) [Tech. Phys. Lett. **25**, 203 (1999)].

Translated by A. Kondrat'ev

Technical Physics Letters, Vol. 28, No. 2, 2002, pp. 139–141. Translated from Pis'ma v Zhurnal Tekhnicheskoĭ Fiziki, Vol. 28, No. 4, 2002, pp. 28–34.

Atomic Force Microscopy of InAs Quantum Dots on the Vicinal Surface of a GaAs Crystal

V. P. Evtikhiev, O. V. Konstantinov, E. Yu. Kotel'nikov, A. V. Matveentsev, A. N. Titkov, and A. S. Shkol'nik

Ioffe Physicotechnical Institute, Russian Academy of Sciences, St. Petersburg, Russia

Received October 2, 2001

Abstract—An approach to the processing of images obtained by atomic force microscopy is proposed. An example of determining the parameters of InAs clusters formed on the vicinal surface of a GaAs crystal is presented. Using the proposed technique within the framework of the previously developed spherical cluster model, it is possible to determine the energy levels of electrons and holes in InAs quantum dots. *© 2002 MAIK "Nauka/Interperiodica".*

Introduction. Properties of the self-organized arrays of InAs quantum dots (QDs) formed during the molecular beam epitaxy (MBE) of InAs on a GaAs surface were extensively studied [1]. Such arrays are usually obtained on the GaAs surface representing a vicinal crystal plane [2] inclined at a small angle (e.g., 6°) relative to the (100) crystallographic plane. An important feature of the QDs grown by MBE on a vicinal GaAs surface is that the distribution of InAs clusters with respect to diameter is much more homogeneous as compared to that observed on the (100) plane.

A direct examination with the aid of atomic force microscopy (AFM) showed that InAs clusters formed on the (100)GaAs surface exhibit agglomeration similar to that observed for liquid droplets merging due to the surface tension. No such effects take place on the vicinal plane, which is probably related to the fact that this plane is not an atomically smooth surface. In fact, this plane represents a stepped surface in which terraces coinciding with the (100) planes are oriented at a small angle relative to an imaginary surface plane. Apparently, the agglomeration of clusters does not take place because the motions of adsorbed In atoms on the vicinal surface in the course of epitaxy is more difficult than the analogous motions on the (100) surface.

AFM image. Figure 1a shows an AFM image of a region on the vicinal GaAs surface bearing QDs. For the comparison, Fig. 1b presents an image of the (100)GaAs surface with analogous clusters showing a clear evidence of the agglomeration process. Below we will demonstrate that visual examination of the AFM images allows many important characteristics of the QD arrays to be determined, including (i) the surface density N of QDs, (ii) the average surface area S per cluster, (iii) the average cluster diameter $D = 2R$, and (iv) the average QD thickness b. The last quantity can be found provided the number n_M of monolayers (ML) required for the obtaining of a given cluster array is given. This number can be determined from the duration of epitaxy, which is usually known. However, the

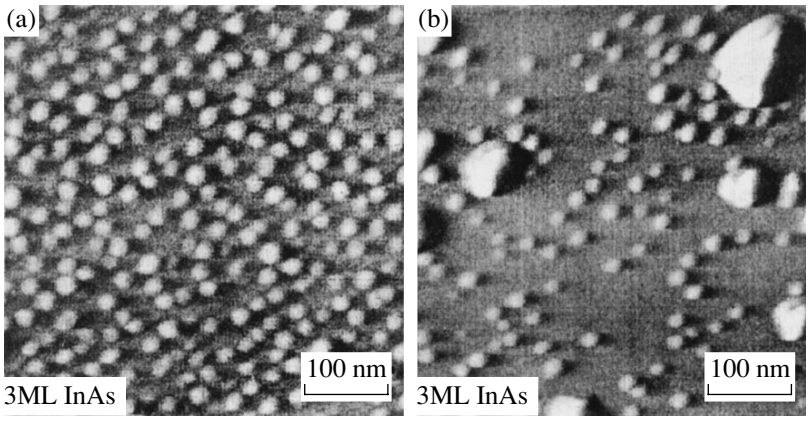

Fig. 1. AFM images of the QD arrays grown (a) on a vicinal GaAs surface inclined by 6° relative to the (100) plane and (b) on the (100)GaAs surface.

1063-7850/02/2802-0139$22.00 © 2002 MAIK "Nauka/Interperiodica"

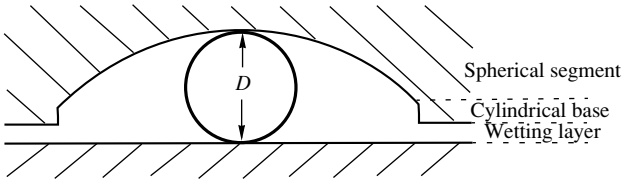

Fig. 2. A QD model for InAs clusters on a GaAs substrate, comprising a wetting layer (1.7 ML thick), a cylindrical base (1 ML thick), and a spherical segment with the curvature radius determined by the average QD thickness. The energy spectrum of the inscribed sphere models that of the charge carriers in the QD.

total MBE process time usually corresponds to a somewhat greater quantity

$$n_M^{tot} = n_M + n_W, \quad (1)$$

where n_W is the number of monolayers necessary to form a wetting layer; in our case, $n_M^{tot} = 2.9$ ML. According to [3], we will assume that $n_W = 1.7 \pm 0.2$ ML. Thus, we arrive at the estimate of $n_M = 1.2 \pm 0.2$ ML.

QD array parameters. Let us estimate the values of the aforementioned QD array characteristics using the AFM image presented in Fig. 1a.

(i) The surface density of QDs. To determine this parameter, it is sufficient to count the number of QDs (180 clusters) observed in the AFM image and determine the size of the imaged area (17×10^4 nm^2). This yields $N = 1.06 \times 10^{11}$ cm^{-2}. The relative error of this estimate being $1/\sqrt{180} = 0.08$, we finally obtain $N = (1.06 \pm 0.08) \times 10^{11}$ cm^{-2}.

(ii) The average surface area per cluster. This parameter is calculated as

$$S = 1/N, \quad S = 0.95 \times 10^{-11} \text{ cm}^{-2}. \quad (2)$$

(iii) The average QD diameter. Direct measurement yields $D = 20 \pm 4$ nm ($R = 10$ nm).

(iv) The average cluster thickness. This parameter is determined using the number of monolayers required to form a given cluster array on the surface; the product of this and the monolayer thickness h_M equals the total layer thickness. If all the substance falling within the area S would concentrate on a smaller area πR^2, the average cluster thickness would increase by a factor of $S/\pi R^2 = 3.03 \approx 3$. Then the average cluster thickness b is given by the formula

$$b = n_M h_M S/\pi R^2. \quad (3)$$

Taking into account that, according to relationship (1), $n_M = 1.2$ ML, and adopting that $h_M = 0.3$ nm, we obtain $b = 1.08$ nm.

QD shape parameters. Let us approximate the cluster shape by the spherical segment depicted in Fig. 2. The segment can be characterized by two parameters, including the cluster height a and either the curvature radius R_S or the base radius R, since the R_S and R values are related as

$$2aR_S = R^2 + a^2. \quad (4)$$

A simple algebra yields an expression for the average cluster height:

$$b = \frac{a}{2}\left(1 + \frac{a^2}{3R^2}\right); \quad a \approx 2b\left(1 - \frac{4b^2}{3R^2}\right). \quad (5)$$

Using this expression and the above parameters, we can estimate the height of the spherical segment as $a = 2.1$ nm.

For calculating the energy levels in the cluster, we replace the spherical segment on a base substrate (wetting layer) by a sphere inscribed into the cluster [4, 5]. Obviously, the diameter d of the inscribed sphere equals a sum of the segment height and the wetting layer thickness:

$$d = a + h_M n_W. \quad (6)$$

Using the values determined above, we obtain $d = 2.6$ nm. This estimate is somewhat greater than the value ($d = 2.2$ nm) we used previously [6]. We can approach the latter value by adding a one-monolayer cylindrical base under the spherical segment as depicted in Fig. 2. Then, the average thickness b should be replaced by a corrected value $b_C = b - 0.3$, from which it follows that $b_C = 0.78$ nm. According to formula (5), this yields the final segment height $a = 1.56$ nm and $d = 2.4$ nm. This diameter of a sphere modeling the QD will be used below.

Carrier energies in the spherical cluster model. The energy levels of electrons and holes in a cluster can be calculated using the spherical cluster model described in [4, 5]. In this model, a smooth envelope can be used even with a nonquadratic approximation of the electron dispersion law [4]. Solving a wave equation with the boundary conditions stipulating continuity of the wave function and its derivative on the spherical surface with $r = d/2$, we obtain the well-known relationships for discrete values of the wavevector k:

$$-\cot\left(\frac{kd}{2}\right) = q/k, \quad (7)$$

$$q^2 = \frac{2m_2}{\hbar^2}(\Delta E - E(k)), \quad (8)$$

where q is a parameter describing the decay of the wave function outside the cluster, m_2 is the effective carrier mass outside the cluster, ΔE is the break at the edge of the conduction or valence band, and $E(k)$ is the disper-

sion law for carriers inside the potential well. For holes, we adopt an isotropic quadratic dispersion law

$$E_v(k) = \frac{\hbar^2 k^2}{2m_v}, \quad (9)$$

where $m_v = 0.4m_0$ is the standard effective mass of a heavy hole in InAs (we ignore a corrugation of the isoenergetic hole surface). Previously [4], we demonstrated the importance of taking into account a nonquadratic character of the dispersion law for electrons in the InAs clusters and selected a phenomenological formula for this law:

$$E_c(k) = \frac{E_1}{2}\left(\sqrt{1 + \frac{2\hbar^2 k^2}{m_1 E_1}} - 1\right), \quad (10)$$

where $m_1 = 0.06m_0$ and $E_1 = 0.4$ eV are the mass and energy fitting parameters, respectively. In order to solve Eq. (7), we must also know the band edge breaks. Selecting these according to the conventional rule, $\Delta E_c = 0.65\Delta E_g$ and $\Delta E_v = 0.35\Delta E_g$ (where ΔE_g is the bandgap width), we obtain with sufficient precision $\Delta E_c = 0.7$ eV and $\Delta E_v = 0.4$ eV. In this approximation, we ignore an increase in the bandgap width related to a possible contraction of the cluster. Taking the square of Eq. (7), we arrive at the following equation for electrons:

$$I_e(x) = \Delta E_c - \frac{E_1}{2}\left(\sqrt{1 + \frac{4E_{d1}x^2}{E_1}} - 1\right), \quad (11)$$

$$I_e(x) = E_{d2}x^2\cot^2(x),$$

$$x = \frac{kd}{2}, \quad E_{d1} = \frac{2\hbar^2}{m_1 d^2}, \quad E_{d2} = \frac{2\hbar^2}{m_2 d^2}. \quad (12)$$

Using the values of parameters determined above, we obtain $E_{d1} = 0.44$ eV and $E_{d2} = 0.407$ eV. Solving numerically the transcendental equation (11) with respect to x, we obtain $x = 1.84$ and the ionization energy for electrons $I_e = 0.099$ eV. By the same token, the dispersion equation for holes takes the following form:

$$I_v(x) = \Delta E_v - E_{d1}x^2,$$
$$I_v(x) = E_{d2}x^2\cot^2(x). \quad (13)$$

In this case, the heavy hole masses inside and outside the cluster are $m_1 = 0.40m_0$ and $m_2 = 0.41m_0$, respectively; $\Delta E_v = 0.4$ eV is the valence band break at the cluster boundary. Using the above values, we obtain the hole energy parameters $E_{d1} = 0.0645$ eV and $E_{d2} = 0.0587$ eV. A solution to the dispersion equation (13) is $x = 2.125$, with the ionization energy for holes $I_h = 0.106$ eV. Then, the photon energy (with neglect of the electron–hole interaction) is

$$\hbar\omega = E_{gGaAs} - (I_e + I_h) = 1.31 \text{ eV}. \quad (14)$$

The experimental photoluminescence spectra of a QD array show a maximum at a photon energy of $\hbar\omega_{max} = 1.33$ eV. A discrepancy of 0.02 eV falls within the interval of uncertainty of the calculation.

REFERENCES

1. I. V. Kudryashov, V. P. Evtikhiev, V. E. Tokranov, *et al.*, J. Cryst. Growth **201**/**202**, 1158 (1999).
2. V. P. Evtikhiev, V. E. Tokranov, A. K. Kryganovskii, *et al.*, J. Cryst. Growth **201**/**202**, 1154 (1999).
3. J. M. Moison, F. Houzay, F. Barthe, *et al.*, Appl. Phys. Lett. **64** (2), 196 (1994).
4. V. P. Evtikhiev, O. V. Konstantinov, and A. V. Matveentsev, Pis'ma Zh. Tekh. Fiz. **27** (6), 65 (2001) [Tech. Phys. Lett. **27**, 248 (2001)].
5. L. V. Asryan and R. A. Suris, Semicond. Sci. Technol. **11**, 554 (1996).

Translated by P. Pozdeev

Technical Physics Letters, Vol. 28, No. 2, 2002, pp. 142–144. Translated from Pis'ma v Zhurnal Tekhnicheskoĭ Fiziki, Vol. 28, No. 4, 2002, pp. 35–40.

A Focusing X-ray Diffractor: Effect of the Crystal Bending Parameters on the Spectral Resolution

E. M. Latush and M. I. Mazuritsky*

Rostov State University, Rostov-on-Don, Russia

** e-mail: mazurmik@icomm.ru*

Received September 4, 2001

Abstract—The dependence of the spectral resolution of a focusing X-ray diffractor on the shape and curvature of the reflecting crystallographic faces in the plane perpendicular to the focusing circle plane is theoretically studied in the point source approximation. The curvature parameters ensuring the best spectral resolution are determined for ellipsoidal and toroidal types of the crystal bending. *© 2002 MAIK "Nauka/Interperiodica".*

X-ray radiation is usually monochromatized with the aid of perfect and mosaic crystals (quartz, silicon, germanium, mica, graphite, etc.). The traditional crystal diffraction schemes were developed and described in sufficient detail [1–4]. The spectral resolution is conventionally defined as a dimensionless ratio $\Delta E/E$ or $\Delta\lambda/\lambda$, where E is the X-ray quantum energy and λ is the corresponding wavelength. For θ denoting the Bragg angle between the incident radiation beam and the tangent to the corresponding crystallographic plane, the Bragg diffraction law stipulates that the admitted range of the Bragg angle variation $\Delta\theta$ is related to the spectral resolution as

$$\Delta\lambda/\lambda = \Delta\theta/\tan\theta \quad (1)$$

and depends primarily on the following factors: the mosaic imperfection of the crystal, the method used for the X-ray radiation expansion into the spectrum, and the size of the Bragg zone on the reflecting surface of a crystal diffractor.

At present, X-ray radiation is frequently monochromatized by reflection from flat or bent crystals. The latter diffractor type is usually employed with the point radiation sources (i.e., those with dimensions not exceeding the crystal curvature radius multiplied by the spectral resolution $\Delta\lambda/\lambda$) to focus the primary X-ray beam with a given wavelength on the detector entrance window. Previously [5], we described an algorithm and presented the results of the computer simulation of the shape of the Bragg zone on the surface of a bent crystal.

Let us study the spectral resolution of a focusing X-ray diffractor as a function of the crystal curvature in the plane perpendicular to the focusing circle plane. A schematic diagram showing mutual arrangement of the radiation source *S*, the crystal diffractor *K*, and the detector *D* in the focusing circle plane is depicted in the figure, where *XYZ* is the coordinate system and *O*', *O* are the centers of the focusing circle and the crystal curvature in the *YOZ* plane, respectively. Below, *r* denotes the length of the *O'A* segment representing the focusing circle radius. Thus, the focusing circle in the *XOY* plane passes through the source *S*, the diffractor apex *A*, and the detector *D*.

Let us consider the toroidal and ellipsoidal types of crystal bending. The cylindrical and spherical types can be considered as special variants of the ellipsoidal bending. The *XOY* and *YOZ* planes are the symmetry planes of the crystal. For any point *P* (except the diffractor apex *A*) on the crystal surface in the *YOZ* plane, the angles θ_1 and θ are not equal. In other words, for the Bragg diffraction in the *YOZ* plane, a beam originating

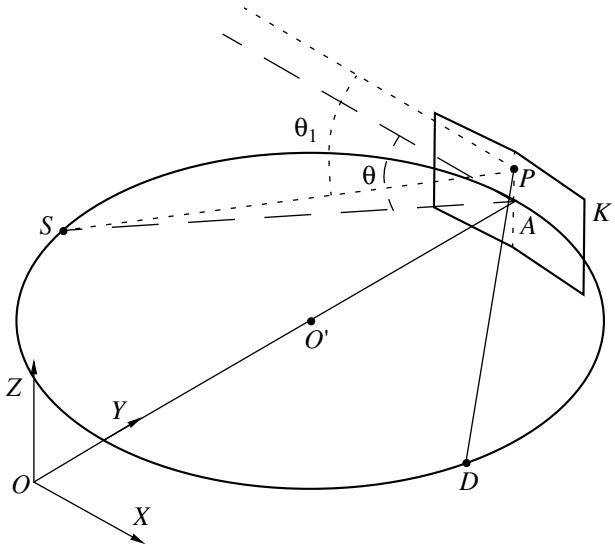

A schematic diagram showing mutual arrangement of the radiation source *S*, the bent crystal *K*, and the detector *D* in the focusing circle plane of a diffractor.

1063-7850/02/2802-0142$22.00

from point *S* strikes the point *P* at a somewhat different angle relative to the tangent as compared to the analogous angle at the center of the bent crystal. Obviously, the longer the distance from point *P* to the crystal apex, the greater the difference between angles θ_1 and θ.

Thus, the deviation $\Delta\theta = \theta_1 - \theta$ of the diffraction angle θ_1 from the true Bragg angle θ depends on the *z* coordinate of point *P*. For a fixed *z*, the $\Delta\theta$ value depends on the radius of crystal curvature in the *YOZ* plane. Let us denote by *b* the radius of curvature of the crystal in the *YOZ* plane for the toroidal type of bending or the corresponding semiaxis for the ellipsoid of revolution. We will study behavior of the function $\Delta\theta(b)$ on the set $b \in (0, \infty)$ at a fixed value of $z \neq 0$ (for $z = 0$, $\theta_1 = \theta$ and $\Delta\theta(b) = 0$).

First, let us consider the case of a crystal with toroidal bending. Now we will demonstrate that the function $\Delta\theta(b)$ defined (for $z \neq 0$) on the set $b \in (0, \infty)$ acquires zero value at the points $2r$ and $2r\sin^2\theta$ of this interval. The crystal cross section by the *YOZ* plane represents an arc with the center at point *O* and the radius *OA* = *b*. The equation of a torus section in the *YOZ* plane can be written as $y^2 + z^2 = b^2$.

As is known, diffractors employed in the X-ray spectroscopy are characterized by small values of z/b (typically $|z/b| \leq 10^{-2}$). To within the second-order terms, we can approximate the expression $y = \sqrt{b^2 - z^2} = b\sqrt{1 - z^2/b^2}$ as $y \approx b - z^2/(2b)$. Taking into account this approximate expression and using the coordinates of points *P*, *O*, and *S*, we readily obtain expressions for the vectors **PS** and **n** (the normal to the crystal atomic plane at point *P*):

$$\mathbf{PS} \approx -2r\sin\theta\cos\theta \cdot \mathbf{i} + \left(\frac{z^2}{2b} - 2r\sin^2\theta\right) \cdot \mathbf{j} - z \cdot \mathbf{k};$$
$$\mathbf{n} \approx \mathbf{PO} = \left(\frac{z^2}{2b} - b\right) \cdot \mathbf{j} - z \cdot \mathbf{k}. \quad (2)$$

We can also express $\sin\theta_1$ through the scalar product of vectors **PS** and **n**:

$$\sin\theta_1 = \cos(90 - \theta_1) = \frac{(\mathbf{n} \cdot \mathbf{PS})}{|\mathbf{n}| \cdot |\mathbf{PS}|}. \quad (3)$$

Taking into account that $\Delta\theta = \theta_1 - \theta \approx \sin\theta_1 - \sin\theta$ and using expressions (2) and (3), we obtain an approximate expression

$$\Delta\theta \approx -\frac{z^2}{b^2}\frac{1 - 2(r/b)(1 + \sin^2\theta) + 4(r/b)^2\sin^2\theta}{8(r/b)^2\sin\theta + (z/b)^2(1/\sin\theta - 2(r/b)\sin\theta)}. \quad (4)$$

The function in the right-hand side of Eq. (4) becomes zero when the numerator is zero. The roots of the quadratic equation $b^2 - 2r(1 + \sin^2\theta)b + 4r^2\sin^2\theta = 0$ are

$$\{b = 2r; \quad b = 2r\sin^2\theta\}. \quad (5)$$

Note that, for these *b* values, the denominator of the ratio in Eq. (4) is not zero since $\theta \in [20°, 60°]$ and $r \gg |z|$.

Evidently, a minimum value of $|\Delta\theta|$ in the case of toroidal bending is achieved for the *b* values satisfying the condition (5). Since $\Delta\theta$ determines the spectral resolution (1) of the diffractor, the best spectral resolution at an arbitrary point $P(0, y, z)$ in the *YOZ* plane is provided by this very condition.

As is known, the optimum (from the standpoint of the spectral resolution) crystal curvature radius in the focusing circle plane is $2r$. Then, according to condition (5), the ratio of the curvature radii R_H and R_V in the *XOY* and *YOZ* planes, respectively, in the case of toroidal bending is

$$\frac{R_V}{R_H} = \begin{cases} 1 \text{ (sphere)} \\ \sin^2\theta. \end{cases} \quad (6)$$

Now let us proceed to the case of a diffractor crystal with ellipsoidal bending. We will demonstrate that the function $\Delta\theta(b)$ defined (for $z \neq 0$) on the set $b \in (0, \infty)$ acquires zero value at the points $\sqrt{2ra}$ and $\sqrt{2ra}\sin\theta$. The crystal cross section by the *YOZ* plane represents an elliptic arc with the center at point *O* and the semiaxes *a* and *b* (along the *Y* and *Z* axes, respectively). The equation of ellipse in the *YOZ* plane can be written as $y^2/a^2 + z^2/b^2 = 1$.

By analogy with the considerations for the case of toroidal bending, we can approximate the expression $y = a\sqrt{1 - z^2/b^2}$ as $y \approx a - (z^2a)/(2b^2)$. Taking into account this approximate expression and using the coordinates of points *P*, *O*, and *S*, we also readily obtain expressions for the vectors **PS** and **n**:

$$\mathbf{PS} \approx -2r\sin\theta\cos\theta \cdot \mathbf{i} + \left(\frac{z^2a}{2b^2} - 2r\sin^2\theta\right) \cdot \mathbf{j} - z \cdot \mathbf{k};$$
$$\mathbf{n} \approx \left(\frac{z^2a}{2b^2} - a\right) \cdot \mathbf{j} - \frac{a^2}{b^2}z \cdot \mathbf{k}. \quad (7)$$

Expressing $\sin\theta_1$ by formula (3) as in the case of toroidal bending, taking into account that $\Delta\theta = \theta_1 - \theta \approx \sin\theta_1 - \sin\theta$ and using expressions (3) and (7), we obtain an approximate expression

$$\Delta\theta \approx -\frac{z^2}{b^2}\frac{1 - 2(ra/b^2)(1 + \sin^2\theta) + 4(ra/b^2)^2\sin^2\theta}{(1 + (z/b)^2(a^2/b^2 - 1)/2)(8(r/b)^2\sin\theta + (z/b)^2(1/\sin\theta - (2ra/b^2)\sin\theta))}. \quad (8)$$

The function in the right-hand side of Eq. (8) turns zero when the numerator is zero. The roots of the biquadratic equation $b^4 - 2ra(1 + \sin^2\theta)b^2 + 4r^2a^2\sin^2\theta = 0$ are $\{b^2 = 2ra; b^2 = 2ra\sin^2\theta\}$. Taking into account that $b > 0$, we obtain

$$\{b = \sqrt{2ra}; \quad b = \sqrt{2ra}\sin\theta\}. \tag{9}$$

For these b values, the denominator of the ratio in Eq. (8) is not zero since $\theta \in [20°, 60°]$ and $r \gg |z|$. Evidently, a minimum value of $|\Delta\theta|$ in the case of ellipsoidal bending is achieved for the b values satisfying the condition (9). Since $\Delta\theta$ determines the spectral resolution (1) of the diffractor, condition (9) actually provides for the best spectral resolution at an arbitrary point $P(0, y, z)$ in the *YOZ* plane.

Since the ellipsoid cross section by the *XOY* plane is an arc of the circle with the center at point *O* and the radius $2r$ ($a = 2r$ is the radius of curvature in the focusing plane), the optimum ratio of semiaxes in the *XOY* and *YOZ* planes according to condition (9) is

$$\frac{b}{a} = \begin{cases} 1 \text{ (sphere)} \\ \sin\theta. \end{cases} \tag{10}$$

REFERENCES

1. A. K. Freund, *X-ray Optics* (ESRF, Grenoble, 1987).
2. C. Bonnelle and C. Mande, *Advances in X-ray Spectroscopy* (Pergamon, Oxford, 1982).
3. J. W. M. DuMond and A. Kirpatrick, Rev. Sci. Instrum. **1**, 88 (1930).
4. H. H. Johann, Z. Phys. **69**, 185 (1931).
5. M. I. Mazuritsky, A. V. Soldatov, E. M. Latush, *et al.*, Pis'ma Zh. Tekh. Fiz. **25** (19), 11 (1999) [Tech. Phys. Lett. **25**, 763 (1999)].

Translated by P. Pozdeev

Technical Physics Letters, Vol. 28, No. 2, 2002, pp. 145–147. Translated from Pis'ma v Zhurnal Tekhnicheskoĭ Fiziki, Vol. 28, No. 4, 2002, pp. 41–45.

Development of the Rayleigh–Taylor Instability in Finite-Strength Media. Two- and Three-Dimensional Perturbations

E. E. Meshkov, N. V. Nevmerzhitskiĭ, and E. A. Sotskov

Institute of Experimental Physics, Russian Federal Nuclear Center, Sarov, Russia

e-mail: root@gdd.vniief.ru

Received September 10, 2001

Abstract—The instability development in plane-parallel jelly layers of various strength accelerated by a compressed gas flow is studied. The character of the perturbation variations significantly depends on the strength of the accelerated layer. © *2002 MAIK "Nauka/Interperiodica".*

When a boundary between two media moves with acceleration directed normally to the interface from a lighter to a heavier component, the boundary exhibits instability of the Rayleigh–Taylor type [1]. The strength of one (or both) of these media is a factor stabilizing the interface, while not completely hindering the development of instability and turbulent mixing. The finite strength implies the existence of critical values of the amplitude and wavelength of the initial perturbation, above which the perturbation can exhibit unlimited growth (see, e.g., [2]).

A convenient method for the investigation of nonstationary hydrodynamic flows is offered by the jelly technique [3], which is especially suited for studying the instability development in finite-strength media [4]. Indeed, the strength can be controlled within broad limits by varying the concentration C of a solution from which the jelly is prepared, since the jelly strength monotonically increases with the concentration.

In our experiments, the 6-mm-thick layer of a jelly representing an aqueous gelatin solution was accelerated by the pressure (~1 MPa) of gaseous products of a gaseous explosive mixture (a stoichiometric acetylene–oxygen composition) in a square (4×4 cm) vertical channel with transparent walls. In the initial position, the jelly layer separated the channel into two parts, the combustion chamber and the acceleration channel, and was maintained in this position by adhesion to the channel walls. In order to reduce the layer sagging caused by its own weight, the interface was additionally reinforced by a thin (5 μm) mylar film, so that the sag did not exceed 1 mm.

The combustion chamber was closed, while the acceleration channel was open. The closed chamber was filled with a stoichiometric acetylene–oxygen mixture ($C_2H_2 + 2.5O_2$). Detonation of the mixture was initiated simultaneously at 64 points uniformly distributed over the channel cross section. No initial perturbation was set on the lower (unstable) boundary of the layer. The initial perturbation was provided only by the three-dimensional perturbation due to the detonation wave (from the initiation system) and the subsequent nonstationary shock wave development as a result of the reflection of the detonation wave from the jelly layer. The pattern of the jelly layer acceleration was monitored with a high-speed camera.

Three series of shots, illustrating the results of an experiment with jelly layers prepared from solutions with the concentrations C = 17.6, 26.4, and 52.8% are presented in the figure. The figure shows images of the accelerating layer obtained simultaneously in two projections. The bottom part of each shot corresponds to the side projection (the viewing direction is perpendicular to the direction of motion). The top part of each shot represents the frontal projection (as if the camera were facing the oncoming layer; these images were obtained with the aid of a mirror mounted at the end of the accelerating channel and inclined at 45° to the channel axis).

Here, of most interest are the frontal images. The pattern of perturbation of the unstable boundary for the layer with C = 17.6% is virtually the same as that typically observed at the gas–liquid interface [5]: the gas penetrates into the liquid by forming a system of competing rounded "bubbles" (the coarsest bubbles grow at the expense of suppressed smaller neighbors), while the liquid protrudes into the gas in the form of streams thinning toward the ends. This pattern is clearly seen in the side view.

The character of the observed pattern sharply changes for the layer with C = 52.8%. Here, the gas penetrates into the jelly by forming strongly extended bent cavities (in the side view, resembling fat smooth caterpillars). Thus, the pattern of perturbation (albeit,

1063-7850/02/2802-0145$22.00

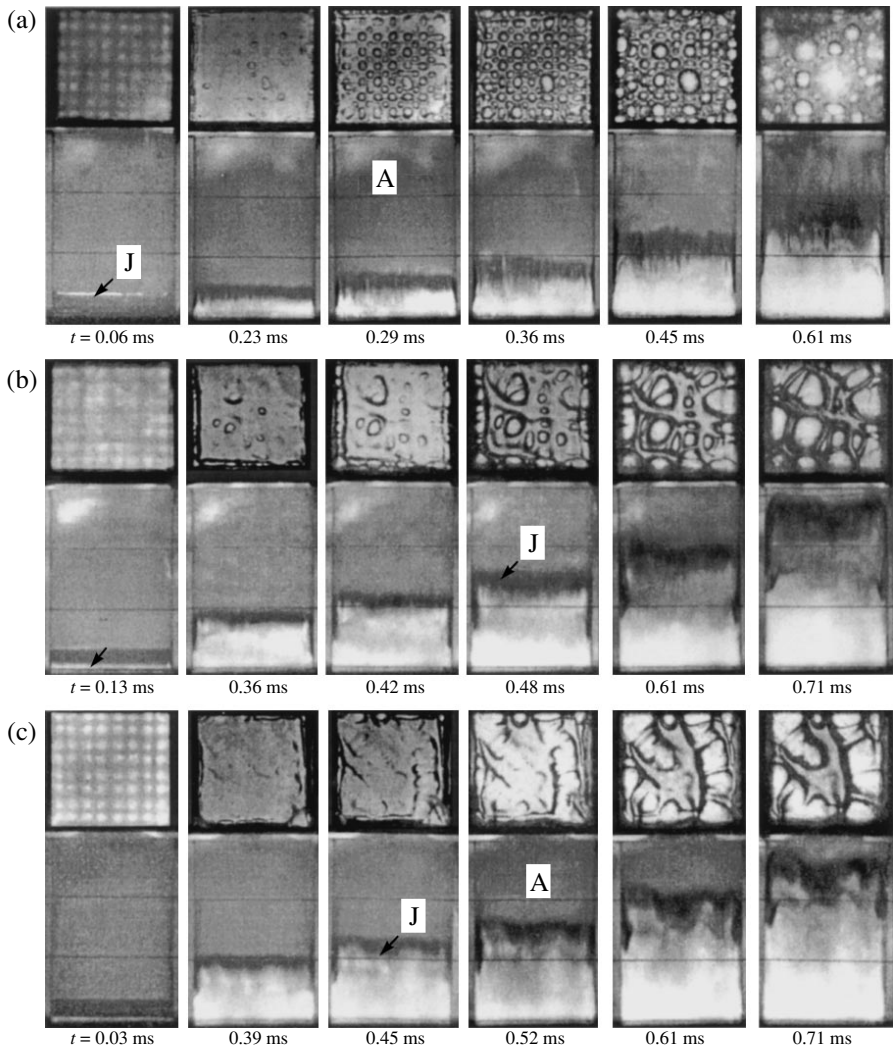

A sequence of shots illustrating the acceleration of a thin jelly layer (J) with the concentration $C = 17.6$ (a), 26.4 (b), and 52.8% (c) by the products of combustion of a gaseous explosive mixture. The time is measured from the moment of detonation. Top rows show the frontal shots through the jelly layer; bottom rows show the side view through the transparent channel walls.

strictly speaking, still being three-dimensional) acquires a two-dimensional character. The streams are practically not distinguished. In all cases, the near-wall layer appears as smeared over the wall of the acceleration channel.

In our opinion, the change in the pattern of perturbation as described above is consistent with the following well-known facts: (a) in media possessing no strength, the three-dimensional perturbations grow at a greater rate than do two-dimensional ones; (b) in media with finite strength, the situation is the opposite [2].

In all cases, the initial perturbations are provided by a three-dimensional detonation wave containing a regular component (from the points of detonation) and a random component (related to the scatter of the detonation moments). Apparently, the regular component dominates in the case of a low-strength layer, thus determining a three-dimensional scenario of the perturbation development in the form of bubbles (the arrangement of bubbles generally resembles that of the detonation points). In the case of a higher strength, the random component seems to prevail with the spectrum containing quasi-two-dimensional structures in the form of "caterpillars."

An interesting pattern was observed in the case of $C = 26.4\%$, which seems to represent an intermediate case between the two mechanisms considered above. Here, both types of the initial perturbations are present, including bubbles of the quasi-rounded shape and of the "caterpillar" type. However, as the perturbations grow with time, the former character begins to prevail and the rounded bubbles dominate. Based on the photographic evidence, we may suggest that development of the turbulent mixing zone at the interface of a finite-strength medium always involves an initial stage when the perturbations develop by the "caterpillar" mecha-

nism (with a two-dimensional character). As the characteristic perturbation scale grows with time, the mechanism gradually changes to that leading to the formation of quasi-rounded bubbles (purely three-dimensional type).

Acknowledgments. The authors are grateful to V.A. Raevskii and P.N. Nizovtsev for fruitful discussion of the results and to M.V. Bliznetsov for the processing of some experimental data.

This study was supported by the Los Alamos National Laboratory (USA), contract no. B70040006-35.

REFERENCES

1. G. I. Taylor, Proc. R. Soc. London, Ser. A **201**, 192 (1950).
2. A. I. Lebedev, P. N. Nizovtsev, V. A. Rayevsky, *et al.*, in *Proceedings of the 5th International Workshop on Compressible Turbulent Mixing, Stony Brook, USA, 1995*, p. 231.
3. O. I. Volchenko, I. G. Zhidov, B. A. Klopov, *et al.*, USSR Inventor's Certificate No. 1026154, Byull. Izobret., No. 24 (1983).
4. M. V. Bliznetsov, E. E. Meshkov, N. V. Nevmerzhitskiĭ, *et al.*, Vopr. At. Nauki Tekh., Ser. Teor. Prikl. Fiz. **54** (1999).
5. O. I. Volchenko, I. G. Zhidov, E. E. Meshkov, *et al.*, Pis'ma Zh. Tekh. Fiz. **15** (1), 47 (1989) [Sov. Tech. Phys. Lett. **15**, 19 (1989)].

Translated by P. Pozdeev

Technical Physics Letters, Vol. 28, No. 2, 2002, pp. 148–150. Translated from Pis'ma v Zhurnal Tekhnicheskoĭ Fiziki, Vol. 28, No. 4, 2002, pp. 46–50.

Structure Degradation and Conductivity Variation in the Perovskite Phase of Yttrium–Barium Ceramics

M. U. Kalanov and É. M. Ibragimova

Institute of Nuclear Physics, Academy of Sciences of the Republic of Uzbekistan, Tashkent, Uzbekistan

Received September 19, 2001

Abstract—It is found that the perovskite phase of yttrium–barium ceramics with the composition $[(Y,Ba)CuO_{3-\Delta/3}]_3$ under normal conditions is metastable and exhibits atmospheric degradation with time. This degradation results in the formation of an orthorhombic $YBa_2Cu_3O_{7-\delta}$ phase characterized by the superconducting transition at $T_c = 91$ K. As a result of the degradation, the conductivity type changes from mixed metallic-semiconductor ($\rho(T) = \text{const}$) to purely metallic in the temperature interval from 100 to 300 K. © *2002 MAIK "Nauka/Interperiodica".*

Previously [1, 2], we demonstrated that yttrium–barium ceramics contain a highly symmetric $[(Y,Ba)CuO_{3-\Delta/3}]_3$ cubic perovskite phase belonging to the space group $Pm3m$. The unit cell of this phase has a simple cubic structure, characterized by a statistical distribution of barium and yttrium atoms in the cationic sublattice and by an oxygen nonstoichiometry in the anionic sublattice. The latter nonstoichiometry, as well as the general ability of materials with a perovskite structure for the reversible absorption and liberation of oxygen, suggests that the perovskite phase of yttrium–barium ceramics under normal conditions must be unstable. This implies the possibility of degradation with the transition to a stabler structural state.

Below we report the results of experimental monitoring of the structural degradation and the variation of conducting properties of the $[(Y,Ba)CuO_{3-\Delta/3}]_3$ ceramics in the course of long-term passive storage under normal ambient conditions.

The storage test was conducted using pellets of the $[(Y,Ba)CuO_{2.85/3}]_3$ ceramics with a diameter of 10 mm and a thickness of 0.6 mm characterized by the oxygen nonstoichiometry $\Delta = 0.15$ and the lattice parameter $a_c = 0.4051$ nm, which were prepared by sintering as described previously [1, 2]. The structural characteristics of the pellets were determined by X-ray diffraction measured on a DRON-UM1 diffractometer using Cu$K\alpha$ radiation with $\lambda = 0.1542$ nm. The temperature dependence of the resistivity was studied by the conventional four-point-probe technique in the temperature interval from 77 to 300 K. The samples were passively stored for more than four months in air at room temperature and a relative humidity of ~50%.

The kinetics of degradation of the perovskite phase in the samples of yttrium–barium ceramics is illustrated in the figure. The X-ray diffraction pattern of the as-sintered sample fully conforms to the space group $Pm3m$ with the lattice parameter $a_c = 0.4051$ nm (diffractogram (a)). After a one-month storage of the sintered samples, the diffraction pattern exhibited splitting of the main structural lines of the perovskite phase (in particular, of the (100), (200), (210), (211), and (310) peaks), except for the peaks of reflections of the (*HHH*) type (such as (111) and (222) peaks, see diffractogram (b)). The splitting of the selective reflections (110) and (220) was somewhat less pronounced as compared to the other peaks. After storage for 2.5 months, the degradation of the phase structure ceased and the X-ray diffraction pattern corresponded to the orthorhombic $YBa_2Cu_3O_{7-\delta}$ phase with $\delta = 0.05$ possessing superconducting properties (diffractogram (c)).

The conductivity of the as-sintered sample exhibited a mixed metallic-semiconductor character ($\rho(T) \approx \text{const}$) with the experimentally measured values $\rho(100) = 8.53 \times 10^{-2}$ Ω cm and $\rho(300) = 8.71 \times 10^{-2}$ Ω cm. In contrast, a ceramic sample with the composition $YBa_2Cu_3O_{6.95}$ exhibited the superconducting transition at $T_c = 91$ K and showed a metallic conductivity in the temperature interval from 91 to 300 K. Additional storage of this superconducting sample for about one month showed stability of the structure under normal ambient conditions (1 atm and *RH* ~ 50% at 300 K).

The observed change in the symmetry of the initial cubic phase of the yttrium–barium ceramics as a result of the long-term structural transition can be explained by the loss of oxygen and by the behavior of the central atom in position (1/2, 1/2, 1/2) of the unit cell. As is known, the perovskite structure contains infinite linear chains of the –M–O–M–O– type (M and O denoting the metal and oxygen atoms, respectively) along each axis of the unit cell. The intersection of these chains at the cationic positions leads to the octahedral coordination [3]. The positions of yttrium and barium cations are coordinated to 12 anionic sites situated at a distance of $2^{1/2}xa_c$.

1063-7850/02/2802-0148$22.00

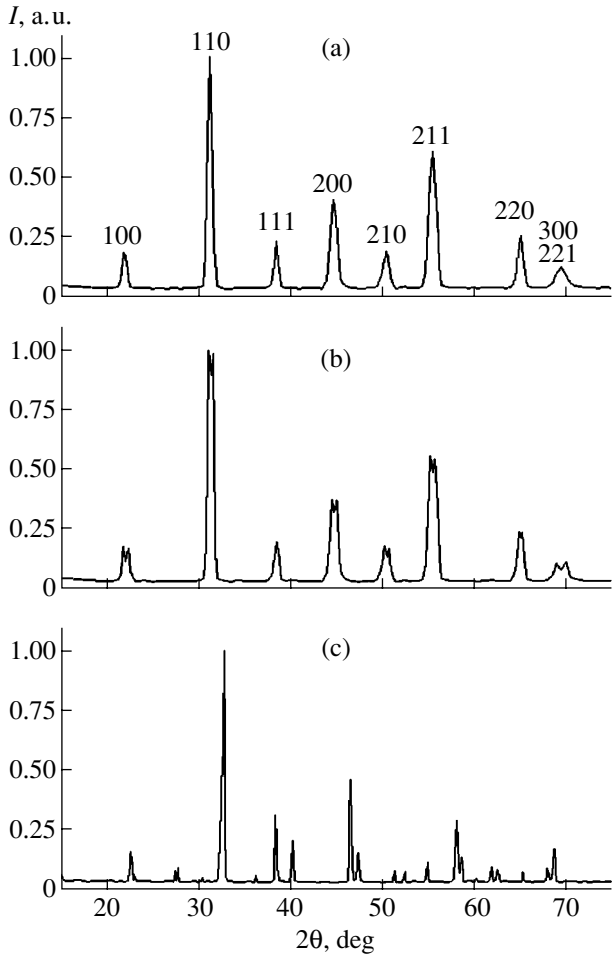

The kinetics of atmospheric degradation of the $[(Y,Ba)CuO_{3-\Delta/3}]_3$ perovskite phase at 300 K as illustrated by the X-ray diffraction patterns of (a) as-sintered sample and of the same stored for (b) 1 month and (c) 3.5 months.

Since the ion volume of Y^{3+} is smaller than that of Ba^{2+} ($V_Y = 4.5 \times 10^{-3}$ nm^3 versus $V_{Ba} = (12–17) \times 10^{-3}$ nm^3 for the covalent radii of yttrium and barium being 0.102 and 0.142–0.160 nm, respectively [4]), it can be expected that oxygen anions surrounding the yttrium cations are more displaced toward the center of the polyhedron. As a result, the cubic subcell around the central position (1/2, 1/2, 1/2) of yttrium is contracted along the *c* axis, whereas that around the barium position is extended. This deformation probably renders the presence of oxygen atoms in positions (0, 0, 1/2) favorable for the barium subcells and unfavorable for the yttrium ones.

Thermal fluctuations drive oxygen atoms to leave positions (0, 0, 1/2) in the yttrium subcells. As a result, these subcells become still more contracted in the direction of the *c* axis. This, in turn, induces a shift of oxygen atoms in the adjacent barium subcells and even of the barium ion (from the initial ideal position) in the same direction. The shift of the barium atom in the intrinsic subcell breaks the equivalence of the Ba–O bonds (characteristic of the cubic cell), whereby the Ba–O bonds on the side of the yttrium subcell become stronger, while the bonds on the opposite side weaken. This factor, together with the oxygen nonstoichiometry (Δ) observed in the perovskite phase of the yttrium–barium ceramics, probably renders positions (0, 1/2, 0) energetically unfavorable for oxygen atoms as compared to positions (1/2, 0, 0). Therefore, the oxygen atoms may partly leave positions (0, 1/2, 0) as a result of the thermoactivated hopping diffusion [5].

The appearing oxygen vacancies reduce the coordination number from 12 to 8 for Y^{3+} cations and from 12 to 10 for Ba^{2+} cations. As a result, there arises a possibility of the ordered arrangement of Y^{3+} and Ba^{2+} cations in positions (1/2, 1/2, 1/2) by the scheme –Y–Ba–Ba–Y– along the *c* axis. This order of the A-cations is characteristic of the superconducting 123-phase of the yttrium–barium ceramics. Based on the above data, the observed atmospheric degradation of the perovskite phase in the yttrium–barium ceramics studied can be described by the quasi-chemical reaction

$$[(Y,Ba)CuO_{3-\Delta/3}] \Rightarrow YBa_2Cu_3O_{7-\delta} + (1+\delta)O_2\uparrow.$$

Thus, the atmospheric degradation of the $[(Y,Ba)CuO_{3-\Delta/3}]_3$ perovskite phase in the yttrium–barium ceramics stored under normal conditions is accompanied by the loss of oxygen and leads to the formation of an orthorhombic $YBa_2Cu_3O_{7-\delta}$ phase characterized by the superconducting transition at $T_c = 91$ K. The proposed mechanism of transformation of the cubic perovskite phase into the superconducting phase may play a dominating role in the synthesis of high-T_c ceramics, melt-grown crystals, and laser-ablation-grown films.

REFERENCES

1. M. U. Kalanov, M. S. Paizullakhanov, V. M. Rustamova, *et al.*, in *Proceedings of the Third International Conference "Modern Problems of Nuclear Physics", Bukhara, Uzbekistan, 1999*, p. 350.
2. M. U. Kalanov, É. M. Ibragimova, T. Kh. Khaidarov, *et al.*, Pis'ma Zh. Tekh. Fiz. **27** (24), 46 (2001) [Tech. Phys. Lett. **27**, 1047 (2001)].
3. P. S. Galasso, *Structure, Properties and Preparation of Perovskite-type Compounds* (Pergamon, New York, 1969).
4. B. D. Shannon and C. T. Piewitt, Acta Crystallogr. B **25**, 925 (1969).
5. J. L. Routbort and S. I. Rothman, J. Appl. Phys. **76** (10), 5615 (1994).

Translated by P. Pozdeev

Technical Physics Letters, Vol. 28, No. 2, 2002, pp. 151–153. Translated from Pis'ma v Zhurnal Tekhnicheskoĭ Fiziki, Vol. 28, No. 4, 2002, pp. 51–56.

On the Nature of Concentration Thresholds for the Electron-Stimulated Desorption of Europium Atoms from the Oxidized Tungsten Surface

S. Yu. Davydov

Ioffe Physicotechnical Institute, Russian Academy of Sciences, St. Petersburg, 194021 Russia
St. Petersburg State Electrotechnical University, St. Petersburg, Russia

Received September 10, 2001

Abstract—The nature of the electron-stimulated desorption (ESD) of europium atoms from an oxidized tungsten surface for the electron energies of E_e = 50 and 80 eV and some features of the yield of Eu atoms as a function of their surface concentration on this surface are discussed. It is shown that the ESD of Eu is related to the electron transitions from the core 5*p* of 5*s* shells of a surface tungsten atom to the outer unoccupied 2*p* level of oxygen. © *2002 MAIK "Nauka/Interperiodica".*

Previous investigations of the electron-stimulated desorption (ESD) of europium atoms from a tungsten surface coated with a monolayer of oxygen (O/W) [1, 2] showed that, first, dependence of the yield of Eu atoms (q) on the energy of bombarding electrons (E_e) exhibits a pronounced resonance character and, second, dependences of the yield q on the O/W surface coverage Θ by adsorbed europium atoms are characterized by the presence of concentration thresholds Θ^*. For example, the $q(E_e)$ peaks corresponding to E_e = 50 and 80 eV (referred to below as peak 50 and peak 80, respectively) are characterized by the thresholds at Θ^* = 0.07 and 0.035: no desorption of Eu atoms is observed for the coverages below the threshold level ($\Theta < \Theta^*$). As for the $q(E_e)$ peak corresponding to E_e = 33 eV (peak 33), the coverage dependence exhibits two thresholds, Θ_1^* = 0.03 and Θ_2^* = 0.35, with $q(\Theta) \neq 0$ in the interval $\Theta_1^* < \Theta < \Theta_2^*$.

The results reported in [1, 2] were theoretically analyzed in [3–5], where the electron state of Eu adatoms on the O/W surface was considered [3] and various ESD mechanisms were discussed [4, 5]. In particular, a model proposed in [5] elucidated the nature of the $q(E_e)$ and $q(\Theta)$ behavior for the ESD peak 33. As will be demonstrated below, an analogous model is applicable to description of the features of behavior observed for the europium desorption peaks 50 and 80 as well.

An analysis of the experimental data showed that the ESD of Eu atoms for E_e = 50 and 80 eV is related to the creation of vacancies in the 5*p* and 5*s* shells of the surface tungsten atoms, respectively [1, 2, 4]. Let us consider the following set of electron energy levels in the Eu–O/W system: (i) an excited 2*p* level of the oxygen adatom with the energy $\varepsilon_p(\Theta)$, which is initially empty (before the appearance of a hole in the core shell of the surface tungsten atom) and finally (after the hole creation) occupied by one electron; (ii) a one-electron 6*s* level of the europium adatom with the center of gravity corresponding to the energy $\varepsilon(\Theta)$, the occupancy of which is $n(\Theta) < 1$; (iii) a 5*p* or 5*s* level of the surface tungsten atom, which is occupied in the initial state and empty in the final state. Note that the selected set of levels is analogous to that employed in the model proposed in [5] (the difference was that previously a 5*p* level of Eu was considered instead of the internal levels of W and a 6*p* empty level of Eu adatom was taken instead of the 2*p* level of oxygen). The energy of the proposed three-level system in the initial (vacancy-free) state is

$$E_0(\Theta) = \varepsilon(\Theta)n(\Theta) + \varepsilon_i, \quad (1)$$

where ε_i is the energy of the internal level (5*p* or 5*s*). Here and below, the energy is measured from the Fermi level.

Let us consider, by analogy with the approach used in [5], two possible scenarios for the creation of vacancies in the core shells of tungsten. According to scenario 1, the ejected electron is transferred to a free quasi-level of oxygen, which represents an interatomic transition (in contrast to the intraatomic one considered in [5] for peak 33). In this case, the potential energy of the excited system is

$$E_1(\Theta) = \varepsilon(\Theta)[1 + n(\Theta)] + Un(\Theta) - G[1 + n(\Theta)], \quad (2)$$

where U is the energy of repulsion between electrons localized on the oxygen and europium atoms and G is the energy of attraction between the ejected electron (localized on the oxygen) and the hole (localized on

tungsten). For simplicity, we assume that the energies $\varepsilon_p(\Theta)$ and $\varepsilon(\Theta)$ are equal.[1]

According to scenario 2, the electron is ejected from the tungsten shell into a vacuum. The potential energy of this excited state is

$$E_2(\Theta) = [\varepsilon(\Theta) - G]n(\Theta). \quad (3)$$

In the case of scenario 1, ionization to the same energy E_e as in scenario 2 would require the excess energy to be carried away by plasmons (for details, see [5]).

For further analysis, it is necessary to consider a difference of the energies of excited states 1 and 2:

$$\Delta W \equiv E_1 - E_2 = Un(\Theta) + \varepsilon(\Theta) - G. \quad (4)$$

If $\Delta W < 0$, scenario 1 is energetically more favorable than scenario 2, while $\Delta W > 0$ implies the inverse situation. Taking into account the resonance character of peaks 50 and 80, as well as of the corresponding thresholds [1, 2], we may suggest that the ESD of Eu atoms is related to scenario 1, since the yield of Eu atoms at higher electron energies E_e is zero (according to scenario 2, the ionization would still take place). Note also that, in the limit of a zero width of the oxygen quasi-level, the condition $\Delta W < 0$ corresponds to this level being occupied by a single electron, which is also consistent with scenario 1. The condition $\Delta W = 0$ may imply both the onset and termination of the ESD process (see [5, Fig. 4]).

Taking into account relationship (4) and the sign of ΔW, we conclude (see Appendix) that the condition

$$\frac{\partial n(\Theta)}{\partial \Theta} < \frac{3}{2}\sqrt{\Theta}\frac{\xi[1 - n(\Theta)]}{U + \xi\Theta^{3/2}} \quad (5)$$

corresponds to the onset of ESD (i.e., to the passage from $\Delta W > 0$ to $\Delta W < 0$), whereas the opposite sense of this inequality implies breakdown of the ESD process. Thus, relationship (5) (together with the condition $\Delta W = 0$) determines the concentration process Θ_1^*, while a relationship inverse to (5) gives the threshold Θ_2^*. In deriving inequality (5), we took into account (for details, see [5]) that

$$\varepsilon(\Theta) = \varepsilon_0 - \xi\Theta^{3/2}[1 - n(\Theta)],$$
$$\xi = 2e^2\lambda^2 N_{ML}^{3/2} A. \quad (6)$$

Here, ξ is the dipole–dipole interaction constant for Eu adatoms, N_{ML} is the concentration of Eu adatoms for a monolayer coverage, 2λ ia the surface dipole arm, $A \approx 10$ is a coefficient weakly dependent on the adlayer geometry, and ε_0 is the energy of the 6*s* quasi-level of a Eu adatom at a zero coverage. Taking into account [5] that

$$n(\Theta) = \pi^{-1}\operatorname{arccot}[\varepsilon(\Theta)/\Gamma], \quad (7)$$

where Γ is the half-width of the above quasi-level, we can reduce relationship (5) to a simpler condition of the ESD onset:

$$\rho(\Theta)U < 1, \quad \rho(\Theta) = \pi^{-1}\frac{\Gamma}{\varepsilon(\Theta)^2 + \Gamma^2}. \quad (8)$$

Here, $\rho(\Theta)$ is the density of states on the Fermi level of Eu adatoms. The inverse inequality, $\rho(\Theta)U > 1$, corresponds to the ESD breakdown.

Let us obtain some numerical estimates using the results of theoretical calculations [5]. Taking $\varepsilon_0 = 1$ eV, $\xi = 24.89$ eV, and $\Gamma = 0.25$ eV for the coverages $\Theta^* = 0.07$ (peak 50) and 0.35 (peak 80), we obtain the following occupancies and energies of the Eu quasi-level: $n = 0.14$, $\varepsilon = 0.63$ eV (peak 50); $n = 0.76$, $\varepsilon = -0.26$ eV (peak 80). For a monolayer europium coverage $\Theta = 1$, we obtain $n = 0.92$ and $\varepsilon = -0.99$ eV. Since the interatomic electron repulsion parameter U is identical to the matrix element $V = 0.74$ eV determined in [4], the condition $\Delta W = 0$ yields the values $G = 0.73$ and 0.40 eV for peaks 50 and 80, respectively. The value $\rho(\Theta^*)U$ is 0.13 for peaks 50 and 0.45 for peak 80, which implies that, in agreement with the experimental data, the coverages $\Theta^* = 0.07$ and 0.35 correspond to the ESD onset for these peaks. At a monolayer coverage, $\Delta W = -1.04$ and -0.71 eV for peaks 50 and 80, respectively, which implies that no ESD breakdowns take place for this coverage—also in agreement with experiment [1, 2].

For comparison, let us consider the analogous characteristics for peak 33. For $\Theta_1^* = 0.03$, we obtain $n = 0.9$ and $\varepsilon = 0.88$ eV. The U and G values can be determined from the condition that $\Delta W = 0$ for Θ_1^* and Θ_2^*, which yields $U = 1.72$ eV and $G = 1.04$ eV. Using these values, we obtain $\rho(\Theta_1^*)U = 0.16$ and $\rho(\Theta_2^*)U = 1.04$. The fact that we obtained somewhat higher values of the Coulomb parameters for peak 33 is quite reasonable, since in this system we deal with intraatomic (rather than interatomic) interaction.

Thus, an analysis of the concentration thresholds for the ESD of europium atoms from the oxidized tungsten surface showed that the ESD peaks 50 and 80 correspond to the interatomic electron transition from a core shell of the surface tungsten atom to an initially vacant outer *p* level of oxygen, whereas the process responsible for the appearance of peak 33 is related to the intraatomic electron transition from a core shell of europium to an outer level of the same atom.

In concluding, let us briefly discuss a difference of the concentration dependence $q(\Theta)$ for peak 33 from

[1] Strictly speaking, we deal with a surface band 1 formed by the states of tungsten and oxygen with a width of 4–5 eV [3]. At a small adsorbate concentration Θ, the quasi-levels of Eu adatoms overlap with this band, while at large Θ, a quasi-two-dimensional band 2 is formed, which is built into band 1. Therefore, we may well assume that $\varepsilon_p(\Theta) = \varepsilon(\Theta)$. This simplification is not of a principal significance, since otherwise the problem would only acquire an additional parameter.

those for peaks 50 and 80 [2]. In the author's opinion, the behavior of $q(\Theta)$ for peak 33 is determined by a probability of the *first* stage of the ESD process, involving the electron transition from 5*p* to 6*p* level of europium. Indeed, the fact that the theoretical curve of $\Delta W(\Theta)$ ([5, Fig. 4, case 1b]) resembles the experimental curve of $q(\Theta)$ ([2, Fig. 2, case *1*]) suggests that $q(\Theta) \infty |\Delta W|^{\alpha}$, where α is an exponent. At the same time, $q(\Theta)$ for peaks 50 and 80 is well described in [4] within the framework of the recharge theory [6, 7]. The latter circumstance implies that the concentration dependence of the yield of Eu for $E_e = 50$ and 80 eV is determined by the *final* stage of the ESD process involving the electron exchange between desorbed particle and the substrate.

Acknowledgments. The author is grateful to V.N. Ageev, Yu.A. Kuznetsov, and N.D. Potekhina for stimulating discussion. This study was supported by the Russian Foundation for Basic Research (project no. 99-02-17972) and by the Federal Program "Surface Atomic Structures" (project no. 4.5.99).

APPENDIX

Since the adatom occupation number $n(\Theta)$ is determined by Eqs. (6) and (7) (see, e.g., [5]), one can readily show that

$$\frac{\partial n(\Theta)}{\partial \Theta} = \frac{3}{2}\sqrt{\Theta}\frac{\rho(\Theta)\xi[1-n(\Theta)]}{1+\Theta^{3/2}\rho(\Theta)\xi}, \qquad \text{(A.1)}$$

$$\frac{\partial \varepsilon(\Theta)}{\partial \Theta} = -\frac{3}{2}\sqrt{\Theta}[1-n(\Theta)] + \Theta^{3/2}\xi\frac{\partial n(\Theta)}{\partial \Theta},$$

where the density of states on the Fermi level $\rho(\Theta)$ is given by formula (8). At the same time, proceeding from expression (4) and the condition of the ESD onset ($\Delta W < 0$), we obtain

$$U\frac{\partial n(\Theta)}{\partial \Theta} < -\frac{\partial \varepsilon(\Theta)}{\partial \Theta}. \qquad \text{(A.2)}$$

Substituting (A.1) into (A.2), we arrive at relationship (5).

REFERENCES

1. V. N. Ageev and Yu. A. Kuznetsov, Pis'ma Zh. Tekh. Fiz. **26** (13), 86 (2000) [Tech. Phys. Lett. **26**, 579 (2000)].
2. V. N. Ageev, Yu. A. Kuznetsov, and N. D. Potekhina, Fiz. Tverd. Tela (St. Petersburg) **43** (10), 1890 (2001) [Phys. Solid State **43**, 1972 (2001)].
3. S. Yu. Davydov, Pis'ma Zh. Tekh. Fiz. **27** (7), 68 (2001) [Tech. Phys. Lett. **27**, 295 (2001)].
4. S. Yu. Davydov, Fiz. Tverd. Tela (St. Petersburg) **43** (9), 1710 (2001) [Phys. Solid State **43**, 1783 (2001)].
5. S. Yu. Davydov, Fiz. Tverd. Tela (St. Petersburg) **44** (2), 375 (2002) [Phys. Solid State **44**, 391 (2002)].
6. S. Y. Davydov, Surf. Sci. **407** (1-3), L652 (1998).
7. S. Y. Davydov, Surf. Sci. **411** (1-3), L878 (1998).

Translated by P. Pozdeev

Technical Physics Letters, Vol. 28, No. 2, 2002, pp. 154–156. Translated from Pis'ma v Zhurnal Tekhnicheskoĭ Fiziki, Vol. 28, No. 4, 2002, pp. 57–64.

Microwave-Stimulated Relaxation of Internal Strains in GaAs-Based Device Heterostructures

N. S. Boltovets, A. B. Kamalov, E. Yu. Kolyadina, R. V. Konakova, P. M. Lytvyn, O. S. Lytvyn, L. A. Matveeva, V. V. Milenin, and O. E. Rengevych

"Orion" State Research Institute, Kiev, Ukraine

Institute of Semiconductor Physics, National Academy of Sciences of Ukraine, Kiev, Ukraine

e-mail: plyt@isp.kiev.ua

Received August 2, 2001

Abstract—We have studied the effect of microwave radiation (frequency, 2.45 GHz; specific power density, 1.5 W/cm^2) on the relaxation of internal mechanical strains in the (i) n–n^+-GaAs structures, (ii) Au–Ti–n–n^+-GaAs diode structures with Schottky barriers, and (iii) GaAs-based Schottky-barrier field-effect transistors (SFETs). It is shown that exposure of the samples to the microwave radiation for a few seconds leads to relaxation of the internal mechanical strains and improves the quality of the semiconductor surface layer structure. This results in improved parameters of the GaAs-based device structures of both (diode and SFET) types, as manifested by increased Schottky barrier height, reduced ideality factor and back current in the diode structures, and increased gain slope and initial drain current in the SFETs. © *2002 MAIK "Nauka/Interperiodica".*

In recent years, the special attention of researchers has been drawn to the effect of microwave processing on the properties of semiconductor material, device heterostructures, and devices [1–10]. This is related both to the search for new technologies and to the investigation of mechanisms responsible for the degradation of semiconductor devices under the action of various external factors (temperature, strong magnetic fields, ionizing radiation, and microwave fields).

An important factor influencing the properties of semiconductor materials and the parameters of related devices is the relaxation of internal mechanical strains. The influence of a microwave radiation on the residual deformation of the surface layers of silicon was reported in [3]. However, to our knowledge, no such investigations were reported for the device heterostructures with potential barriers and ohmic contacts. Previously [11, 12], we showed that the relaxation of internal mechanical strains not always leads to degradation of the heterostructures and related devices. Below we present some new data on the effect of microwave radiation on the parameters of Au–Ti–n–n^+-GaAs diode structures and Shottky-barrier transistor structures and on the relaxation of internal mechanical strains in the plates with an n–n^+-GaAs structure and the Schottky-barrier field-effect transistor (SFET) topology and in the Au–Ti–n–n^+-GaAs diode structures.

The experiments were performed with the n–n^+-GaAs(100) structures obtained by vapor-phase epitaxy under commercial conditions, the related Au–Ti–n–n^+-GaAs Shottky-barrier diode structures, and GaAs-based SFETs with a Shottky-barrier gate formed by Au–Ti metallization. The ohmic contacts on the device structures of both types were obtained by applying an Au–Ge eutectic composition. The diode structure diameter was 500 μm.

Both before and after the microwave treatment (irradiation in a free space in a magnetron operating at 2.45 GHz at a specific power density of 1.5 W/cm^2 for 0.5–10 s), the samples were characterized by measuring the current–voltage (I–U) characteristics (for the diode structures and SFETs), the plate curvature radius R, and the surface-barrier electroreflectance (SBER) spectra (for the n–n^+-GaAs structures). The SBER spectra were used to determine the collisional broadening parameter Γ. The curvature radius R was either measured on a P201 profilometer–profilograph or determined from the X-ray diffraction data. The profilograms were measured on the side of the film or the device structure topology without damaging the sample surface. The internal mechanical strains were calculated by the Stoney formula [11] using the radius of bending of the n–n^+-GaAs sample structures. The room-temperature SBER spectra were measured by an electrolytic method in the photon energy range from 1.2 to 2.0 eV at a spectral resolution of 3 meV. The spectra were interpreted in terms of the weak-field theory using a three-point technique.

The experimental parameters of the diode and transistor structures and the plate curvature radii measured before and after the microwave treatment are presented in Tables 1 and 2. As can be seen from these data, the microwave irradiation even for a few seconds leads to significant changes in the parameters of diode structures correlated with even more pronounced changes in the bending radii of the plates bearing the device struc-

tures. The irradiation-induced changes include (i) an increase in the Schottky barrier φ_B, (ii) a decrease in the ideality factor n, and (iii) a more than tenfold decrease in the thermoactivated back current I_b of diodes and an increase in the gain slope and initial drain current of SFETs.

The process of structural relaxation in the GaAs plates with a SFET topology significantly depends on the level of structure perfection and bending of the samples (Table 2). For example, a 5-s microwave processing of a sample (plate 1) featuring no initial bending ($R = \infty$) resulted in a curvature radius of $R = 2.9$ m and impaired the SFET parameters (the initial drain current and the gain slope decreased). After a 10-s irradiation of the initially stressed plates with opposite signs of the surface bending, it was found that one of the samples (plate 2) changed both magnitude and sign of the curvature and the other sample (plate 3) completely relaxed (to $R = \infty$), while both structures showed improved SFET parameters. In the plates with $R = \infty$, changes in the device parameters were more significant than in the other samples. Maximum changes in the parameters of diode and transistor structures were observed upon the complete irradiation-stimulated relaxation ($R = \infty$) of the stressed state.

The observed effects can be explained by taking into account that the microwave treatment can stimulate the gettering of defects in the active region of the device structure, which is related to the relaxation of internal mechanical strains. Previously, the effects of stress relaxation and the related defect gettering were observed in the samples subjected to thermal, radiation, field, and ultrasonic treatments [11, 12]. An analysis of the bending radii measured with the profilometer on the n–n^+-GaAs structures before and after a 0.5–10-s microwave, together with the calculated mechanical strains σ (Fig. 1, curve *1*), shows that the σ value in the microwave-irradiated samples decreased approximately by half an order in magnitude. The parameter Γ estimated for the same samples from the SBER spectra (Fig. 1, curve *2*) decreased after irradiation by a factor of about 1.5. This quantity characterizes the structural perfection of a surface layer of the n–n^+-GaAs structure: the smaller the Γ value, the more perfect the semiconductor surface layer. According to [13], the observed decrease in Γ provides evidence of an increase in the Hall mobility in the surface layer and,

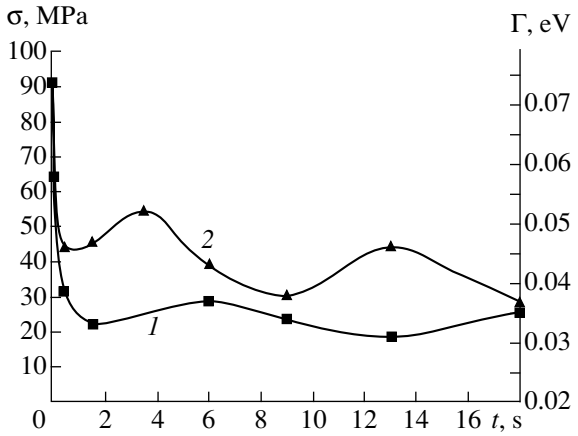

Fig. 1. Time variation of the (*1*) level of internal mechanical strains σ and (*2*) collisional broadening parameter Γ in the course of the microwave treatment of GaAs-based heterostructures.

Table 1. Parameters of the Au–Ti–n–n^+-GaAs diode structures measured before and after microwave treatment

Parameter	Microwave treatment time, s							
	0	0.5	1	2	3	5	6	10
φ_B, V	0.63	0.64	0.66	0.69	0.72	0.72	0.72	0.72
n	1.35	1.35	1.3	1.22	1.15	1.15	1.15	1.15
I_b, A (U_b = 4 V)	4×10^{-8}	4×10^{-8}	2×10^{-8}	4×10^{-9}	10^{-9}	10^{-9}	10^{-9}	10^{-9}
R, m	6.0	12.0	19.0	∞	∞	∞	∞	∞

Table 2. Bending radii and parameters of the GaAs-based Schottky-barrier field-effect transistor structures measured before and after a 10-s microwave treatment

Parameter	R (initial), m			R (final), m		
	Plate 1	Plate 2	Plate 3	Plate 1	Plate 2	Plate 3
	$R_1 = \infty$	$R_2 = -2.82$	$R_3 = 4.53$	$R_1 = 2.9$	$R_2 = 11.9$	$R_3 = \infty$
I_2/I_1	1	1	1	0.8	1.08	1.3
S, mA/V	42	35	37	36	37	42

Note: I_2/I_1 is the ratio of initial drain currents of the irradiated and initial SFET; S is the transistor gain slope.

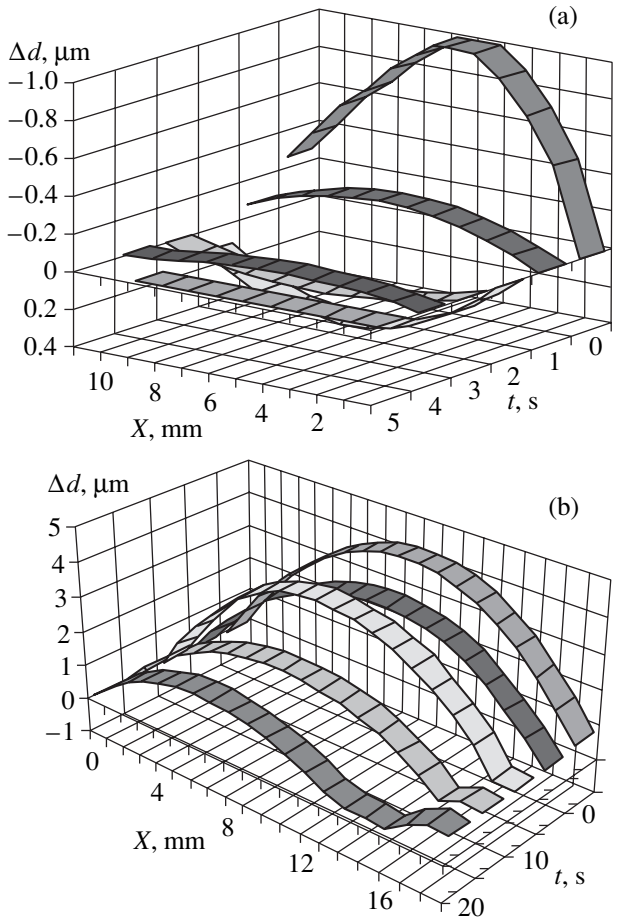

Fig. 2. Changes in the profiles of atomic planes on the surface of (a) n–n^+-GaAs and (b) Au–Ti–n–n^+-GaAs structures as a result of the microwave treatment.

hence, of the defect gettering in this layer. Changes of this type were also observed in the plates bearing the SFET topology and in the Au–Ti–n–n^+-GaAs Schottky-barrier diode structures. In accordance with an increase in the carrier mobility, the SFET structures exhibited increasing gain slope and drain current, while the diode structure showed a decrease in the thermoactivated back current.

An analogous information concerning changes in the curvature radius and the relaxation of internal mechanical strains in the device structures was obtained by X-ray diffraction measurements. Figure 2 shows changes in the profiles of atomic planes on the surface of n–n^+-GaAs and Au–Ti–n–n^+-GaAs structures as a result of the microwave treatment. As can be seen, a 5–10-s exposure to the microwave radiation can provide for a complete relaxation of internal strains in the samples of both types. By the data of topographic investigations based on the anomalous X-ray transmission effect, the dislocation density distribution in the n–n^+-GaAs structure has a weakly-pronounced W-shaped character not affected by a microwave treatment in the indicated regimes. Separate dislocations are generated and then propagate along the slip planes from the edge into bulk of the substrate. The contrast due to microscopic inclusions tends to vanish, which is evidence of the decay of these inclusions. Changes in the dislocation structure are accompanied by an intensive rearrangement of the fields of elastic deformations, resulting in their more uniform distribution over the samples. In the device structures with both diode and transistor structures, these changes correlate with an increase in the useful yield of devices with identical parameters.

Thus, the results of our investigation showed that relaxation of the internal mechanical strains in GaAs-based device structures with Schottky barriers, stimulated by an 0.5–10-s exposure to a microwave radiation with a frequency of 2.45 GHz and a specific power density of 1.5 W/cm^2, is accompanied by pronounced structure–impurity ordering in the surface layer of GaAs that ensures an increase in the parameters of diode and transistor structures with Schottky barriers.

REFERENCES

1. D. E. Abdurakhimov, F. Sh. Vakhidov, V. L. Vereshchagin, *et al.*, Mikroélektronika **20** (1), 21 (1991).
2. D. E. Abdurakhimov, V. L. Vereshchagin, V. P. Kalinushkin, *et al.*, Kratk. Soobshch. Fiz., No. 6, 27 (1991).
3. V. I. Pashkov, V. A. Perevoshchikov, and V. D. Skupov, Pis'ma Zh. Tekh. Fiz. **20** (8), 14 (1994) [Tech. Phys. Lett. **20**, 310 (1994)].
4. V. V. Milenin, R. V. Konakova, V. A. Statov, *et al.*, Pis'ma Zh. Tekh. Fiz. **20** (4), 32 (1994) [Tech. Phys. Lett. **20**, 147 (1994)].
5. S. B. Bludov, N. P. Gadetskiĭ, K. A. Kravtsov, *et al.*, Fiz. Plazmy **20** (8), 712 (1994) [Plasma Phys. Rep. **20**, 643 (1994)].
6. A. A. Belyaev, A. E. Belyaev, I. B. Ermolovich, *et al.*, Zh. Tekh. Fiz. **68** (12), 49 (1998) [Tech. Phys. **43**, 1445 (1998)].
7. V. I. Chumakov, Radiotekhnika **106**, 120 (1998).
8. T. A. Briantseva, Z. M. Lebedeva, I. A. Markov, *et al.*, Appl. Surf. Sci. **272**, 288 (1999).
9. H. Zohm, E. Kasper, P. Mehringer, and G. A. Muller, Microelectron. Eng. **54**, 247 (2000).
10. A. E. Kadukov and A. V. Razumov, Peterb. Zh. Élektron., No. 2, 53 (2000).
11. *Structural Relaxation in Semiconductor Crystals and Device Structures*, Ed. by Yu. A. Tkhorik (Feniks, Kiev, 1994).
12. E. F. Venger, R. V. Konakova, V. V. Milenin, *et al.*, Vopr. At. Nauki Tekh., Ser. Fiz. Radiats. Povrezhdeniĭ Radiats. Materialoved. **3** (75), 60 (1999).
13. O. Yu. Borkovskaya, S. A. Grusha, N. L. Dmitruk, *et al.*, Zh. Tekh. Fiz. **55** (10), 1977 (1985) [Sov. Phys. Tech. Phys. **30**, 1161 (1985)].

Translated by P. Pozdeev

Technical Physics Letters, Vol. 28, No. 2, 2002, pp. 157–158. Translated from Pis'ma v Zhurnal Tekhnicheskoĭ Fiziki, Vol. 28, No. 4, 2002, pp. 65–70.

A Magnetostatic Mass Analyzer of the Plane Mirror Type with Second-Order Focusing

L. P. Ovsyannikova and T. Ya. Fishkova

Ioffe Physicotechnical Institute, Russian Academy of Sciences, St. Petersburg, 194021 Russia

e-mail: L.Ovsyannikova@pop.ioffe.rssi.ru

Received October 16, 2001

Abstract—An optimum operation regime of a plane magnetostatic mirror analyzer is established with a homogeneous field and increased transmission provided by the second-order focusing. In contrast to the well-known mass spectrometer scheme with the half-circle focusing, both the source and detector of charged particles are arranged outside the field. For the spectrograph operation mode, we have determined the coordinates of the focus line on which the detectors should be located. © *2002 MAIK "Nauka/Interperiodica".*

There are many types of charged-particle mass analyzers employing both homogeneous and inhomogeneous fields, as well as of prism mass spectrometers. In practice, most widely used are the instruments employing 60% and 90% sector homogeneous magnetic fields. In addition, some instruments intended for the chemical analysis employ the simplest mass analyzers of the magnetostatic mirror type with plane-parallel poles creating a homogeneous magnetic field and ensuring a 180° deviation of the charged particle beam. The particle beam is injected perpendicularly to the magnetic field lines and the angular focusing is provided at the field edge. A disadvantage of this mass spectrometer scheme is that both the source and detector of charged particles have to be arranged in the field. Moreover, these instruments possess a relatively small transmission because only a rough angular focusing of the diverging beam is provided by the scheme.

In this study, we have determined the optimum parameters for a mass spectrometer with a homogeneous field operating with the beam entrance angles different from 90° (Fig. 1). An interval of the beam entrance angles was determined in which the first-order focusing is provided for the particle source and detector arranged outside the field. The optimum beam entrance angle was found which ensures the second-order focusing in the plane of dispersion of the mass spectrometer.

The radius of curvature of the charged particle trajectories in a homogeneous magnetic field is determined by the well-known formula $\rho = c/H\sqrt{-2m\Phi/e}$, where m and e are particle mass and charge, respectively, Φ is the accelerating potential, c is the speed of light, and H is the magnetic field strength. Expressions for the main system parameters in the plane of dispersion of a mass analyzer operating in the plane mirror regime can be obtained in a simple analytical form in terms of the radius of curvature and the beam entrance angle. For example, the mass analyzer base (i.e., the distance from source to detector, see Fig. 1) is $L = 1 + (h + g)\cot\theta$, where $l = 2\rho\sin\theta$ is the spacing between the entrance and exit points of the central trajectory of a beam injected at an angle θ.

The condition of the first-order focusing with respect to the beam divergence angle ($\pm\alpha$) determines the sum of distances from the source (h) and detector (g) to the point of entrance into the field: $h + g = 2\rho\sin^2\theta\cos\theta$. As is seen from this expression, the focusing takes place at the field edge for $\theta = 90°$ [1] and inside the field for $\theta > 90°$. However, the latter case is of no interest from the standpoint of the most favorable arrangement of the source and detector. For the first-order focusing, the second-order aberration coefficient is $C_2 = 1/2\partial^2 L/\partial\theta^2 = \rho\sin\theta(2\cot^2\theta - 1)$. This value becomes zero for the central trajectory entrance angle $\theta_0 = \arctan\sqrt{2} = 54.74°$, in which case $h + g = 0.770\rho$ and $L = 2.177\rho$. This regime is optimum from the standpoint of using maximum beam divergence angles responsible for instrument transmission.

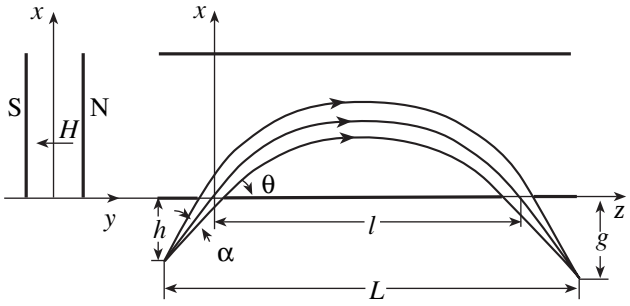

Fig. 1. A schematic diagram of the mass analyzer with a homogeneous field. The curves show the particle trajectories in the plane mirror operation mode.

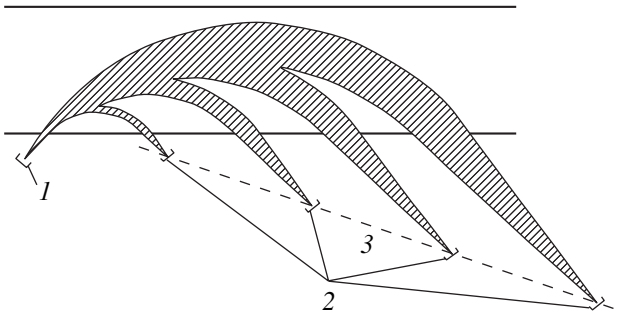

Fig. 2. A schematic diagram of the multichannel mass spectrograph with a central trajectory entrance angle $\theta_0 = 54.7°$: (*1*) ion source; (*2*) detectors; (*3*) focus line.

For the regime of mass spectrometer operation with the second-order focusing, it is of interest to determine the third-order aberration coefficient. This characteristic, given by the formula $C_3 = 1/6\partial^3 L/\partial\theta^3 = -2\rho\cos\theta_0 = -1.155\rho$, determines the beam image expansion. For a mass analyzer operating in the plane mirror regime, the coefficient of linear dispersion in a homogeneous field is $D_m = \rho\sin\theta$, which yields $D_m = \rho$ for $\theta = 90°$ (see [1]). In the aforementioned optimum regime with second-order focusing, the linear dispersion coefficient is somewhat lower $D_m = 0.8165\rho$. However, the specific dispersion (determining the system resolution in the case of a point source) equal to the ratio of the dispersion coefficient to the highest aberration term ($\delta = 0.707/\alpha^3$) is significantly greater than that for the traditional instruments with the half-circle focusing ($\theta = 90°$, $\delta = 1/\alpha^2$) since the beam divergence angle is $\alpha \ll 1$ rad. It should be noted that the specific dispersion is also greater in the regime employing only the first-order focusing for the beam entrance angles $90° > \theta > 45°$, since $\delta = 1/[(2\cot^2\theta - 1)\alpha^2] > 1/\alpha^2$. The most interesting region is that near the optimum angle θ_0 ($50° \le \theta \le 60°$), where the specific dispersion is more than twice as large as that of an instrument with the half-circle focusing.

A comparison of the proposed mass spectrometer with the optimum beam entrance angle to the sector type instruments [1] showed that, for the same resolution, the beam divergence angle of a point source of ions can be increased (due to the high-order focusing) by a factor of 3–4.

It was also of interest to consider the aforementioned mass analyzer with plane-parallel poles operating in the spectrograph mode, since such instruments are frequently employed in various investigations of charged particles, in particular, for the plasma diagnostics (see, e.g. [2]). Figure 2 shows a diagram of trajectories in such a spectrograph with the optimum central trajectory entrance angle $\theta_0 = 54.7°$ for the charge particle mass varying by a factor of 16. In the field-free space of each channel, the system provides for the second-order focusing with the focus line representing a straight line with the coordinates

$$x_f = h - 0.770\rho_0\sqrt{m/m_0},$$

$$z_f = 2.177\rho_0\sqrt{m/m_0} - 0.707h$$

(the origin of coordinates is located at the entrance point of a base trajectory with the curvature ρ_0 for the particle mass $m_0 = 1$). It should be noted that the position of the source can be varied within $0 < h < 0.770\rho_0$, whereby the focus line would exhibit a parallel shift by $0.770\rho_0 < g_0 < 0$ (since $h_0 + g_0 = 0.770\rho_0$).

Operation in the above spectrograph mode with the source and detector arranged outside the field ensures, in addition to improved focusing conditions, a higher transmission as compared to that in the traditional schemes. For example, a commercial mass spectrometer of the MX-1330 type for the chemical analysis of multicomponent organic mixtures [1] is characterized by a mass resolution (at the peak base) of $R = 9000$, which is achieved for the source and detector slit widths $s_1 = s_2 = 0.1$ mm and a beam divergence angle of $2\alpha \approx 0.7°$. For the same slit width and the trajectory curvature, the same resolution in a spectrograph operating in the proposed regime is achieved at a significantly greater beam divergence angle ($2\alpha = 3.4°$). For the same slit width and the beam divergence angle, the mass resolution in the proposed system increases by a factor of 1.5 because of a significantly smaller total expansion of the entrance and exit slit images, which is related to a correction of the second-order aberrations.

Thus, we have found an optimum operation regime for mass analyzers of the plane magnetostatic mirror type. This regime provides for an increase in the mass resolution and/or transmission of the instrument. In contrast to the traditional schemes of mass spectrometers with the half-circle focusing, both the source and detector of charged particles are arranged outside the field.

REFERENCES

1. V. M. Kel'man, I. V. Rodnikova, and L. M. Sekunova, *Static Field Mass-Spectrometers* (Nauka, Alma-Ata, 1985).
2. A. B. Izvozchikov *et al.*, Zh. Tekh. Fiz. **62** (2), 157 (1992) [Sov. Phys. Tech. Phys. **37**, 201 (1992)].

Translated by P. Pozdeev

Technical Physics Letters, Vol. 28, No. 2, 2002, pp. 159–161. Translated from Pis'ma v Zhurnal Tekhnicheskoĭ Fiziki, Vol. 28, No. 4, 2002, pp. 71–77.

On the Possibility of a Collective Acceleration of Ions in a Magnetically Insulated Vircator in the Regime of a Traveling Distributed Virtual Cathode Boundary

A. E. Dubinov[a], V. D. Selemir[a], and V. P. Tarakanov[b]

[a] *Institute of Experimental Physics, Russian Federal Nuclear Center, Sarov, Russia*

[b] *Associated Institute for High Temperatures, Russian Academy of Sciences, Moscow, Russia*

Received September 21, 2001

Abstract—A new scheme for the acceleration of ions by a traveling distributed virtual cathode boundary is proposed. Operation of the scheme is based on the phenomenon according to which an electron beam with a density exceeding a certain threshold exhibits a transition into the so-called compressed state. This state is characterized by a small velocity, a large electron density, and the developed turbulence of the opposite flows. The results of numerical calculations are presented. © *2002 MAIK "Nauka/Interperiodica".*

The collective ion acceleration in high-current beams of positively charged particles is most frequently provided by the devices employing electron beams with virtual cathodes, such as reflex triodes [1, 2], gas-filled vircators [3, 4], and vacuum vircators with ion extraction from an anode (Luce diode, plasma-anode vircator) [5, 6].

An obvious disadvantage of the reflex triodes is that the virtual cathode is, on the average, immobile. Therefore, the overall acceleration energy on approaching the virtual cathode is small even for a sufficiently high rate of ion acceleration. This circumstance probably explains the fact that these schemes did not attract the attention of researchers in the past decade.

The vircators of the two types mentioned above employ moving virtual cathodes and are operated so as to provide for a maximum synchronism between the virtual cathode and the accelerated ions. However, the driving force of a directed virtual cathode motion in a vircator is the gradual neutralization of a negative space charge of the virtual cathode by the supplied ions. In other words, the virtual cathodes in these schemes would be also immobile on the average in the absence of ions. This circumstance does not favor creation of the collective ion accelerators with controlled acceleration rate. Therefore, it would be important to develop an acceleration scheme in which a virtual cathode would be capable of moving at a controlled velocity independently of the ion beam.

For this purpose, Lymar' *et al.* [7] suggested accelerating ions by the edge field of a traveling distributed virtual cathode boundary, thus providing for the wave of switching from the "state with virtual cathode" to "the state with fully transit current." At the same time, Latsko *et al.* [8] put forward an almost analogous idea to create a chain of several virtual cathodes along the acceleration axis with the aid of a series of electron diodes. As the ion beam propagates along the acceleration axis, an external device is used to switch every electron gap from the state with a virtual cathode to the state without such a cathode. It is possible to provide that the trailing front of the chain would move synchronously with the accelerated ion beam. The synchronism of the collective acceleration and the modular design of the accelerator can basically allow the ions to be accelerated practically to any energy. However, there is one technical feature complicating these schemes. The problem is that, according to [7, 8], the directions of motion of the accelerated ion beam and the electron beams creating the virtual cathode are mutually perpendicular and, hence, the conventional magnetic systems of beam tracing are inapplicable. This problem casts doubt as to the very possibility of constructing long accelerating channels using the aforementioned schemes.

Below we propose a new scheme for the acceleration of ions in the regime of a traveling distributed virtual cathode boundary and present the results of the corresponding calculations.

The principle of operation of the new scheme is based on a phenomenon [9] according to which electron beams with a density exceeding a certain threshold limit exhibit a transition from the two-flow state into the so-called compressed state. The compressed beam state is characterized by a small velocity, a large electron density, and a developed turbulence of the opposite flows. It was also established that the compressed beam state development in a foil-free magnetically insulated vircator, representing a long tube with a stepwise change in the diameter and a cathode situated in the narrower section, exhibits a wave character. The wave of switching from double-flow beam state (DBS) to

1063-7850/02/2802-0159$22.00

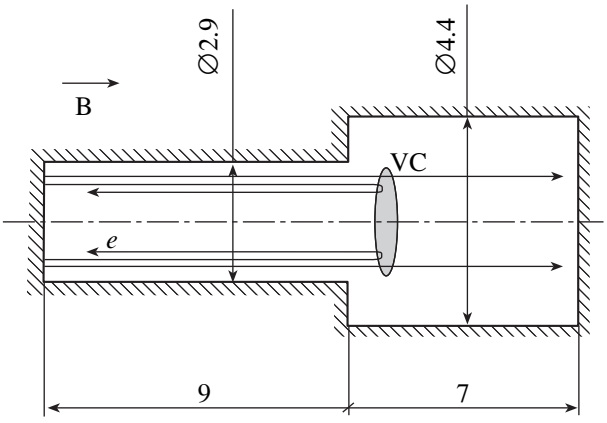

Fig. 1. The geometry of a magnetically insulated vircator with a traveling distributed virtual cathode (VC) boundary (figures indicate dimensions in centimeters).

compressed beam state (CBS) propagates from virtual cathode to cathode, that is, in the direction opposite to injection. The velocity of the DBS–CBS switching wave was estimated at ~10 cm/ns. In order to explain this phenomenon, a theory was developed based on the balance of moments of the pressure forces in the cross sections on various sides of the tube diameter step. In fact, CBS is a virtual cathode distributed in the drift space.

It should be noted that the attaining of CBS is accompanied by the accumulation of an additional charge and the velocity of the DBS–CBS switching wave is determined by the rate of charge accumulation, that is, by the ratio of a beam current to the threshold current.

The dynamics of CBS development was studied in [10–12]. It was found [10] that the rate of CBS devel-

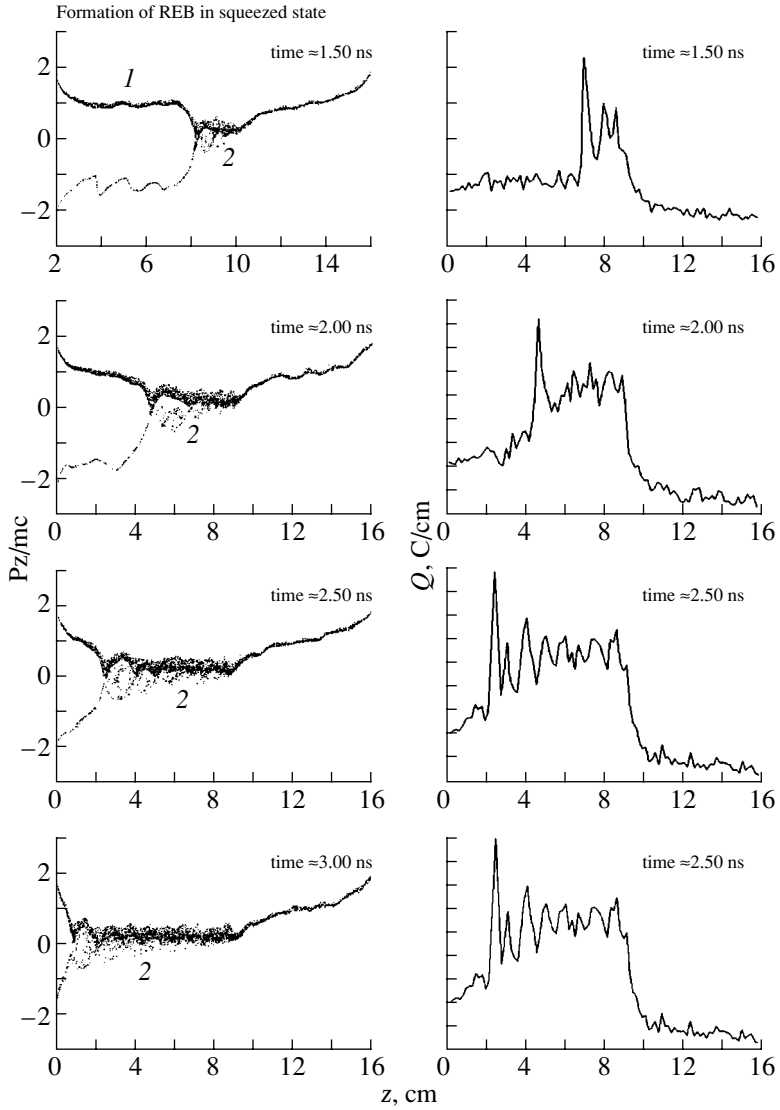

Fig. 2. Evolution of (left column) the beam phase portrait and (right column) the charge distribution along the vircator axis illustrating the wave character of the compressed beam state development: (*1*) DBS, (*2*) CBS.

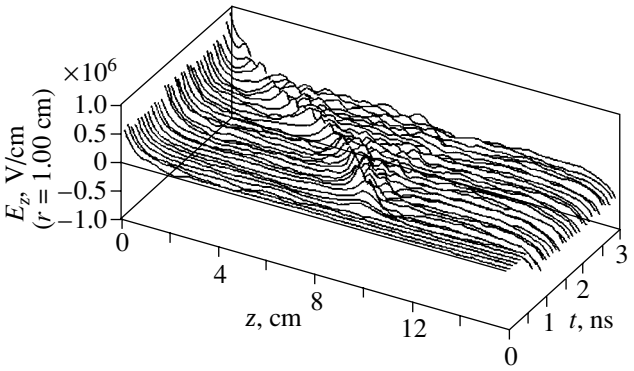

Fig. 3. Spatiotemporal dynamics of the longitudinal electric field in the model system.

opment decreases if a foil is placed (or a thin plasma layer is formed) at the diameter step of a magnetically insulated vircator. In the scheme of a magnetically insulated vircator with a magnetic plug proposed in [11], where the CBS is attained between the virtual cathode and the plug, the switching wave may propagate in the opposite direction (away from the cathode).

Since the switching wave front features a significant change in the electron density, this region is also characterized by a strong longitudinal electric field accelerating the positive ions. The dynamics of the switching wave and the related electric field was calculated using a 2D(rz) variant of the KARAT (Version 80007win) program package [13] representing a fully self-consistent relativistic electromagnetic PIC code. The system geometry (Fig. 1) and the electric parameters of the magnetically insulated vircator (current, 10 kA; accelerating voltage, 750 kV; homogeneous axial magnetic field, 50 kG) were approximately the same as reported in [9].

The presence of a compressed beam state in the system can be readily established using an instantaneous beam phase portrait. Figure 2 shows the calculated dynamics of the CBS switching wave motion, illustrated by several beam phase portraits and the synchronous instantaneous electron space charge profiles. These profiles confirm that the CBS–CBS switching wave front is characterized by a significant change in the electron density.

We have also calculated the dynamics of the longitudinal electric field distribution at a radius equal to the external beam radius. The spatiotemporal pattern of this field is shown in Fig. 3. The results of these calculations indicate that the electric field amplitude at the DBS–CBS switching wave front is approximately constant, amounting to several fractions of MV/cm. The velocity of the switching wave is readily controlled by varying, for example, the channel radius or the rate of electron density accumulation in CBS (i.e., the beam current). If the DBS–CBS switching wave is charged with an ion bunch, this charge can be accelerated for a relatively long time at a very high rate. The magnetic field and the radial potential well created by electrons provide for the transverse stability of the ion beam.

Thus, we have proposed a scheme for the collective acceleration of ions, which is free of disadvantages inherent in the other known schemes and allows stably operating accelerators to be created.

Acknowledgments. This study was supported by the International Scientific-Technological Center, project no. 1629.

REFERENCES

1. S. Humphries, Jr., R. N. Sudan, and W. C. Condit, Jr., Appl. Phys. Lett. **26** (12), 667 (1975).
2. V. M. Bystritskiĭ and A. N. Didenko, Usp. Fiz. Nauk **132** (1), 91 (1980) [Sov. Phys. Usp. **23**, 576 (1980)].
3. S. W. Kuswa, L. P. Bradley, and G. Yonas, IEEE Trans. Nucl. Sci. **NS-20** (3), 305 (1973).
4. A. A. Kolomenskiĭ, V. M. Likhachev, I. N. Sinil'shchikova, *et al.*, Zh. Éksp. Teor. Fiz. **68** (1), 51 (1975) [Sov. Phys. JETP **41**, 26 (1975)].
5. J. S. Luce, H. L. Sahlin, and T. R. Crites, IEEE Trans. Nucl. Sci. **NS-20** (3), 336 (1973).
6. A. L. Babkin, A. E. Dubinov, V. S. Zhdanov, *et al.*, Fiz. Plazmy **23** (4), 343 (1997) [Plasma Phys. Rep. **23**, 316 (1997)].
7. A. G. Lymar', V. V. Belikov, A. V. Zvyagintsev, *et al.*, Vopr. At. Nauki Tekh., Ser. Yad.-Fiz. Issled., Teor. Éksp., No. 5, 71 (1989).
8. E. M. Latsko, RF Patent No. 1529476, MKI: N05 N 5/00, 9/00, Byull. Izobret., No. 46 (1989).
9. A. M. Ignatov and V. P. Tarakanov, Phys. Plasmas **1** (3), 741 (1994).
10. A. E. Dubinov, Pis'ma Zh. Tekh. Fiz. **23** (22), 29 (1997) [Tech. Phys. Lett. **23**, 870 (1997)].
11. A. E. Dubinov, Radiotekh. Élektron. (Moscow) **45** (7), 875 (2000).
12. A. E. Dubinov and I. A. Efimova, Zh. Tekh. Fiz. **71** (6), 80 (2001) [Tech. Phys. **46**, 723 (2001)].
13. V. P. Tarakanov, *User's Manual for Code Karat* (Berkley Research Associate Inc., Springfield, 1992).

Translated by P. Pozdeev

Technical Physics Letters, Vol. 28, No. 2, 2002, pp. 162–163. Translated from Pis'ma v Zhurnal Tekhnicheskoĭ Fiziki, Vol. 28, No. 4, 2002, pp. 78–80.

Centrifugation of Liquid Low-Melting Metals

V. N. Gurin, L. I. Derkachenko, I. N. Zimkin, M. M. Korsukova, and S. P. Nikanorov

Ioffe Physicotechnical Institute, Russian Academy of Sciences, St. Petersburg, 194021 Russia

e-mail: Vladimir.Gurin@pop.ioffe.rssi.ru

Received October 25, 2001

Abstract—Special purity grade metallic gallium in the melted state was centrifuged for the first time at various accelerations in the range from 1000*g* to 12000*g*. The crystallized metal exhibits a small change in the lattice period and a significant increase in the microhardness with increasing acceleration. The previously observed effects of the centrifugal acceleration upon the structure, composition, and properties of multicomponent systems are confirmed for the first time in a one-component liquid metal system (with point defects probably playing the role of the second component). © *2002 MAIK "Nauka/Interperiodica".*

To our knowledge, no investigations of the centrifugation of low-melting metals in the melted state were reported so far. It was commonly accepted that such processes cannot lead to significant changes in the structure and properties of metals. Below we will demonstrate for the first time that the centrifugal acceleration acting upon melted gallium leads to crystallization of the metal with changed structural characteristics and significantly modified properties.

The samples were centrifuged under the conditions analogous to those used to study the crystallization of ionic compounds in the course of centrifugation [1]. Melted gallium of the special purity grade (99.99997% Ga) was heated to ~80°C and centrifuged for 30 min at various accelerations (1.3, 6.2, or 11.8) $\times 10^3 g$. After this treatment, a part of the gallium melt that remained in the liquid state was decanted. The crystallized parts were extracted from tubes and studied.

The crystalline samples were characterized by conventional methods with respect to the lattice period (DRON-2 diffractometer using FeK_α radiation with λ = 1.93597 Å) and microhardness (PMT-3 device with the Knoop pyramid indentor; experimental error, 7%). The lattice periods of the initial metal and the samples crystallized under various acceleration regimes (1.3, 6.2, or 11.8) $\times 10^3 g$ were determined with an experimental error of (2–4) $\times 10^{-4}$ nm using (420), (403), and (234) reflections. The experimental results are summarized in the table.

As can be seen from data presented in the table, the metal structure formed in the centrifuge is slightly distorted as compared to that of the reference samples—the initial gallium (published data) and the metal thermally treated by approximately the same scheme as the centrifuged specimens (g = 1 in the table). On the whole, we may conclude that the lattice constant a in the centrifuged samples decreases (below $g = 11.8 \times 10^3$), while the lattice constants b and c tend to increase (for g indicated in the table). This change in the structure leads to a very significant growth in the microhardness with increasing acceleration. This is confirmed by the H_K values measured for three indentor loads (except for the value obtained under a load of 98.1 mN for the sample treated at $6.2 \times 10^3 g$, where the H_K versus acceleration curve exhibits a break). The observed consistent increase in the microhardness measured for all the indentor loads employed cannot be accidental. The effect is due to a certain deformation of the crystal structure which consists, as is seen from the table, in a small decrease of the constant a at an increase in the b and c values.

Now it is not possible to specify details of this deformation pattern (increased dislocation density, stressed chemical bonds, etc.). Elucidating these questions would require special investigations, including neutron or X-ray diffraction measurements, determination of the dislocation density in the samples treated at various accelerations, etc. A significant experimental difficulty is related to the fact that the surface of a gallium ingot cannot be oriented in a certain crystallographic direction: for any cleavage, the slip system is not revealed and a sample exposes a fracture surface passing through several crystallographic planes. This behavior explains why the results of the microhardness measurements performed with the aid of the Knoop pyramid are presented in the table without indication of the corresponding crystal plane. Another experimental difficulty is related to the low melting point of gallium (28.79°C), which hinders the preparation of metallographic sections with a certain crystallographic orientation for the microhardness measurements and the study of other properties and characteristics.

A hypothesis that the centrifugation may lead to the formation of a glassy sate is confirmed neither by the X-ray diffraction measurements (all the centrifuged samples behaved as "single crystals" or as materials

The results of measurements of the lattice parameters (a, b, c) and the microhardness (H_K) for three indentor loads P of the initial and centrifuged gallium samples at 20–23°C

Acceleration g ($1g = 9.81$ m/s^2)	a, nm	b, nm	c, nm	H_K, MPa ($P = 19.6$ mN)	H_K, MPa ($P = 49.0$ mN)	H_K, MPa ($P = 98.1$ mN)
Publ. data	0.4530	0.4500	0.7632	–	–	–
1	0.4535	0.4516	0.7645	111	135	59
1.3×10^3	0.4524	0.4522	0.7649	250	236	176
6.2×10^3	0.4520	0.4524	0.7652	272	240	131
11.8×10^3	0.4528	0.4516	0.7653	384	292	202

composed of a few coarse grains) nor by the experiments on the material melting in a differential scanning calorimeter. Investigations of the density of samples by the method of hydrostatic weighing revealed no significant difference between the samples prepared at $g = 1$ and $g = 11.8 \times 10^3$.

Acknowledgments. The authors are grateful to V.M. Egorov, Yu.A. Burenkov, and Yu.G. Nosov for their help in conducting this investigation.

This study was supported by the Russian Foundation for Basic Research, project no. 01-03-32822.

REFERENCES

1. V. N. Gurin, S. P. Nikanorov, A. P. Nechitaĭlov, *et al.*, Fiz. Tverd. Tela (St. Petersburg) **43** (7), 1196 (2001) [Phys. Solid State **43**, 1241 (2001)].

Translated by P. Pozdeev

Technical Physics Letters, Vol. 28, No. 2, 2002, pp. 164–166. Translated from Pis'ma v Zhurnal Tekhnicheskoĭ Fiziki, Vol. 28, No. 4, 2002, pp. 81–86.

The Optical Properties of Long-Lived Luminous Formations

G. D. Shabanov

St. Petersburg Institute of Nuclear Physics, Russian Academy of Sciences, Gatchina, Leningrad oblast, Russia
e-mail: Discharge@gtn.ru

Received April 4, 2001; in final form, September 4, 2001

Abstract—Luminous formations initiated by electric discharge appear differently depending on the intrinsic luminosity, external illumination, and the background color. These formations simultaneously exhibit four colors: red, yellow, violet, and blue. These colors are known to be typical of the ball lightning (BL) possessing, according to the available statistics [1], a short lifetime. At the same time, it was stated [2] that there is BL of two types: short- and long-lived. Based on the results obtained, it is suggested that the short-lived BL must also exhibit all four colors simultaneously.[1] © *2002 MAIK "Nauka/Interperiodica".*

This study continued with the investigations of plasma formations initiated by an erosive discharge [3–6]. The author agrees with Avramenko *et al.* [6] in believing that these objects represent "a laboratory analog of ball lightning." On the other hand, the appearance of erosive plasma formations (Avramenko streams) generated as described in [3–6] is far from resembling natural ball lightning (BL). The purpose of this study was to obtain, under erosive discharge conditions, a luminous formation that would be close to BL in both size and appearance.

The base electric scheme of an erosive plasmatron [4] with stored energy increased up to 7.5 kJ allowed a luminous formation to be obtained which resembled that reported in [4]: "Formed in the head part of a long-living energy-consuming plasmoid was a "furry" plasmoid possessing an ellipsoidal shape with a diameter of ~7 cm and a length of ≈10 cm." The furry plasmoid observed in our experiments also possessed a diameter of ~7 cm and a length of ~9 cm (Fig. 1). By changing the plasmatron polarity and reducing the anode–cathode spacing, we obtained a luminous formation with a diameter of ≈9 cm and a lifetime of 0.5–1 s (Fig. 2). The results were fully reproducible. Thus, we have succeeded in obtaining luminous formations in the erosive discharge, the dimensions and appearance of which were close to those known for natural BL.

In some experiments, the surface of a luminous formation was touched with the end of a wire freely suspended on dielectric threads, which resulted in the ejection of a substance from the object. In [3–6], it was suggested to distinguish the "core" and "shell" parts in the Avramenko streams. It was believed [4] that these are two interpenetrating plasma structures, one of which is "similar to a usual heated gas and, accordingly, can be readily blown out by an air flow from a long-lived energy-consuming plasmoid." Suggesting that this component represented for the most part the products of erosion of the material (stearin and wax) covering the plasmatron channel [4], we used the plasmatron channel made of quartz without any coating. To provide for the maximum suppression of the erosive process, we also replaced the iron cathode by a graphite unit. As a result, the luminosity of the plasma formations sharply dropped so that it was possible to observe the objects by the naked eye. Note that the appearance of luminous formations observed in these experiment resembles descriptions of the autonomous formation as reported in [7]: "a not very bright yellow ball 1–1.5 mm in diameter, with visibly constant luminance and a distinct spherical boundary, noiselessly vanishing approx-

Fig. 1.

[1] A good illustration to this study is offered by the first BL observation described by Stakhanov [2]. In that case, all data (including the diameter, velocity, and trajectory) communicated by two observers between which the BL traveled coincided, except that one reported it was yellow, while the other described it appearing as a "red-hot coal." The most probable reason for this discrepancy is that the BL was observed on a different background.

imately 1 s after appearance." The only significant difference is that the diameter of a luminous formation observed in our experiments reached more than 10 cm in diameter (Fig. 3); that is, it was two orders of magnitude greater than the object reported in [7].

For making photographs of the luminous formations, each experiment was repeated: the object was photographed with and without flash. Photographed with the flash, the luminous formations obtained in the quartz plasmatron exhibited unusual optical properties. An observer viewing the object against the background of a dark (night) window described it as a transparent violet formation with a weakly luminous shell. Indeed, this object appeared as "transparent": the leaves of a plant and the opposite wall are well distinguishable through the formation.[2] The lifetime of the object was ~0.5 s; the diameter reached ~10 cm. The luminous formation appeared as yellow on a green background and seemed white against a white wall. Against a green and white background, the shell region appears red. We do not present a color photograph here because all significant information is lost when reproduced in black and white.

The unusual combination of optical properties of the luminous formation and the simultaneous presence of violet, yellow, and red in the same object (depending on the observation conditions) resembled the descriptions given in [1], where the following correlation between the color and lifetime was pointed out. "A nontrivial feature was a nonmonotonic relationship between the lifetime of the luminous formation and the luminosity and color. Confirmed by a greater volume of information, these data may be evidence for the existence of two types of luminous formations." The observed colors of our luminous objects agree with those reported for BL characterized by short lifetimes on the correlation plot presented in [1]. Therefore, it is possible to relate these colors to BL called short-lived in [2], where BL was classified only between two groups. We observed three colors simultaneously present in the same luminous formation and revealed under various observation conditions. All these colors belong to the same object, probably BL, representing the short-living type. Note that, in addition, a blue color was also reported in [1] as belonging to BL with a short lifetime.

Another series of experiments was devoted to attempts at separately observing the existing colors. This task has proved to be rather difficult. Many rather contradictory remarks about colors were made previously [3–7]. Indeed, it was pointed out that "half of the emission falls within the infrared range" [3] and refined

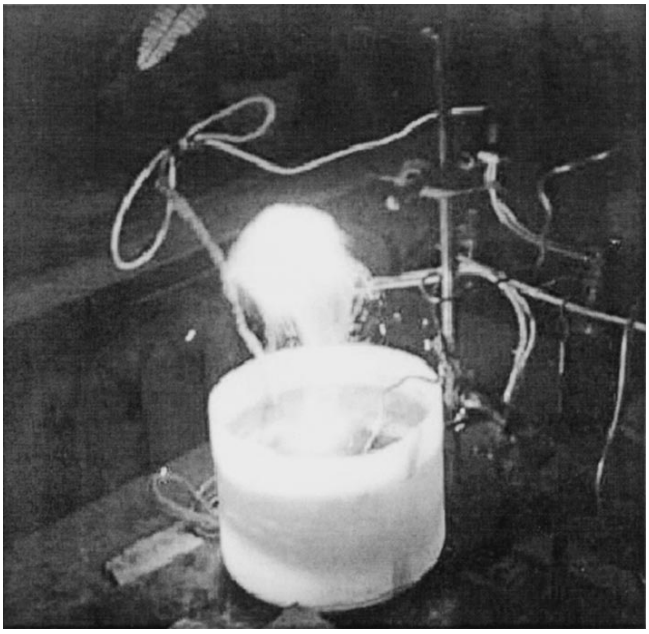

Fig. 2.

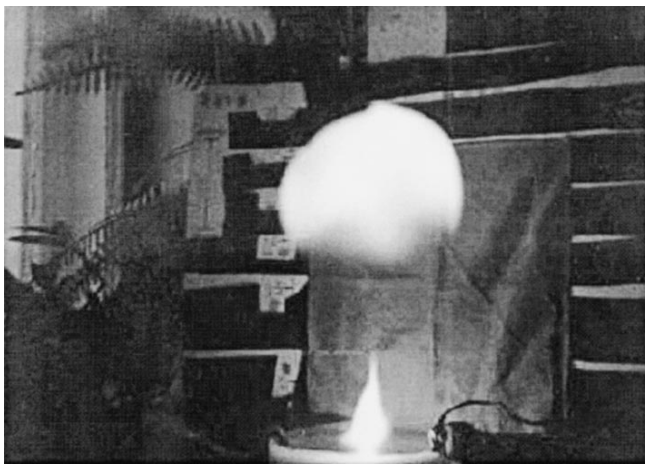

Fig. 3.

that "the red and ultraviolet emission was concentrated within a narrow (on the order of 0.1 mm) frontal part of the shell" [5], while the same shell was reported as "blue-violet" in [4] and "pale yellow" in [7].

The difficulties in visually determining the observed color spectrum are related to specific features of color perception by humans. These features are well illustrated by the relative photopic luminous efficiency curve, from which it follows that the efficiencies of red and yellow colors under daylight conditions are K_λ = 0.004 and 0.995, respectively. This implies that, under otherwise identical conditions, red is detected by less than 0.5% relative to yellow. Under twilight illumination conditions, the sensitivity with respect to red drops

[2] The transparency is not unusual for BL. For example [2]: "An interesting property of BL is the transparency in the visible range. Communications that the surrounding objects can be seen through BL (of course, provided that the intrinsic emission from BL is not intensive so as to hinder the observer's ability of looking directly at BL) can be found in reviews and in answers to our questionaries." Note the valuable remark concerning the intrinsic BL luminosity.

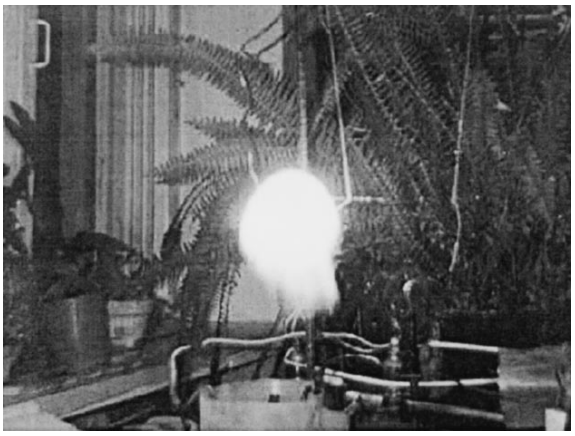

Fig. 4.

by another two orders of magnitude. Thus, the observations of a certain color in BL depend on the luminosity, external illumination conditions, and background.

The presence of red was confirmed by the experiments performed under daylighting conditions with screens and under twilight conditions in the presence of steam. The red shell was observed almost in all color photographs. There were also no problems with observing yellow, which was also present in all photographs (the luminous formation in Fig. 3 was completely yellow). It was more difficult to detect violet and blue (mentioned in [1]). These colors were best detected under low illumination conditions, mostly in twilight. According to the photopic luminous efficiency curve, these colors are characterized by $K_\lambda \sim 0.1$ and ~0.5, respectively. A mixture of violet and blue colors was well distinguished in a photograph made against a white wall near window (Fig. 4).

Conclusions. (1) A "nonmonotonic" relationship between the BL lifetime and color [1] is explained by the fact that red, yellow, violet, and blue belong to BL of the same type (short-lived). Moreover, all these colors belong to the same object, but the level of detection of each particular color depends on the intrinsic luminance, external illumination level, and background on which the object is observed.

(2) The first point confirms the existence of BL of two types, as suggested in [1] and affirmed in [2].

Acknowledgments. The author is grateful to A.I. Egorov and S.I. Stepanov for their participation in experiments and fruitful discussions and to K.A. Bush for advice in photography. Many thanks to A.I. Grigor'ev for valuable remarks.

REFERENCES

1. A. I. Grigor'ev and I. D. Grigor'eva, Zh. Tekh. Fiz. **59** (2), 79 (1989) [Sov. Phys. Tech. Phys. **34**, 176 (1989)].
2. I. P. Stakhanov, *On the Physical Nature of Ball Lightning* (Nauchnyĭ Mir, Moscow, 1996).
3. R. F. Avramenko, B. N. Bakhtin, V. I. Nikolaeva, *et al.*, Zh. Tekh. Fiz. **60** (12), 57 (1990) [Sov. Phys. Tech. Phys. **35**, 1396 (1990)].
4. A. I. Klimov and G. I. Mishin, Pis'ma Zh. Tekh. Fiz. **19** (13), 19 (1993) [Tech. Phys. Lett. **19**, 405 (1993)].
5. S. E. Emelin, V. S. Semenov, A. I. Éĭkhval'd, and A. K. Khassani, in *Ball Lightning in Laboratory: A Collection of Articles* (Khimiya, Moscow, 1994), pp. 87–95.
6. R. F. Avramenko, V. I. Nikolaeva, and L. P. Poskacheeva, in *Ball Lightning in Laboratory: A Collection of Articles* (Khimiya, Moscow, 1994), p. 15.
7. S. E. Emelin, V. S. Semenov, V. L. Bychkov, *et al.*, Zh. Tekh. Fiz. **67** (3), 19 (1997) [Tech. Phys. **42**, 269 (1997)].

Translated by P. Pozdeev

Technical Physics Letters, Vol. 28, No. 2, 2002, pp. 167–169. Translated from Pis'ma v Zhurnal Tekhnicheskoĭ Fiziki, Vol. 28, No. 4, 2002, pp. 87–94.

The Influence of the Boundary Layer Thickness in the Vicinity of a Body Streamlined by a Hot Gas Flow on the Efficiency of Surface Cooling by a Submerged Cold Stream

V. G. Volkov, V. V. Lebedev, and S. O. Shiryaeva

Yaroslavl State University, Yaroslavl, Russia

e-mail: shir@uniyar.ac.ru

Received April 10, 2001

Abstract—Using numerical modeling methods, we have reproduced the experimental effect of decrease in the efficiency of a cooling gas screen with increasing boundary layer thickness in the vicinity of a body streamlined by a hot gas flow. The simulation results allow the effect to be rationalized on a physically rigorous level, avoiding simplifications common in analytical descriptions and undesired in technical applications.

Introduction. Various problems of hydrodynamics and gasdynamics encounter the problem of cooling bodies streamlined by liquids and gases. The most effective means of solving this task is to create a cold gas screen in the vicinity of the body by injecting a stream of this gas into the hot medium flow [1–3]. The cooling gas screens formed by tangential slit injection of a coolant through the protected body surface into a turbulent boundary layer were sufficiently well studied by analytical and empirical methods. The practical application of screens is usually characterized by a broad spectrum of perturbing factors acting upon the boundary layer, including nonisothermicity and compressibility of the gas flow, pressure gradient, wall permeability, chemical reactions, etc.

In contrast to the case of the gas stream injected through a tangential slit, the coolant injected through a sloped channel in the protected solid wall in the general case forms a system of submerged near-wall streams, instead of creating a continuous screening film [4]. In this case, we can only speak of a certain layer featuring the coolant mixed with the main flow, with the parameters of this mixture determining the state of the screen. These parameters are determined, in turn, by the conditions of interaction between the main and injected flows. This interaction depends, albeit in an empirically unpredictable manner, on the presence and the state of a boundary layer at the wall. The analytical and semiempirical calculation methods also cannot take into account every variety of the interaction conditions. Therefore, it was of interest to study the role of the boundary layer in the gas screen formation by numerical methods.

Calculation methods. In order to analyze the pattern of flow arising upon forming a gas screen by a series of equidistant cooling streams injected into the main transverse flow, we have developed a special program for calculating a three-dimensional turbulent flow. The program is based on a complete system of the Navier–Stokes equations (averaged according to Reynolds), which can be written in the following dimensionless form [5]:

$$\frac{\partial \rho}{\partial t} + \mathrm{div}(\rho \mathbf{V}) = 0,$$

$$\frac{\partial}{\partial t}(\rho \mathbf{V}) + \mathrm{div}(\rho V_n V_m) + \mathrm{grad}\left(p + \frac{2}{3}\rho k\right)$$

$$+ \frac{1}{\mathrm{Re}_0}\left[\mathrm{grad}\left(\frac{2}{3}\mu_* \mathrm{div}\mathbf{V}\right) - \mathrm{div}(2\mu_* S_{nm})\right] = 0,$$

$$\frac{\partial}{\partial t}(\rho H) + \mathrm{div}(\rho \mathbf{V} H) - (\gamma_0 - 1)M_0^2\left[\frac{\partial p}{\partial t} - \mathrm{div}\left(\frac{2}{3}\rho k \mathbf{V}\right)\right]$$

$$+ \frac{(\gamma_0 - 1)M_0^2}{\mathrm{Re}_0}\mathrm{div}\left[\frac{2}{3}\mu_* \mathbf{V}\mathrm{div}\mathbf{V} - 2\mu_* V_n S_{nm}\right]$$

$$- \frac{1}{\mathrm{Re}_0 \mathrm{Pr}_0}\mathrm{div}\mathbf{q} = 0,$$

$$\rho = \frac{1 + \gamma_0 M_0^2 p}{T}, \quad H = h + 0.5(\gamma_0 - 1)M_0^2 V^2.$$

Here, h is the gas enthalpy; p is the dynamic pressure related to the dimensional pressure p' as $p = (p' - p_0)/(\rho_0 V_0^2)$; V, ρ, and T are the gas velocity, density, and temperature, respectively; μ_* is the effective viscosity equal to a sum of the molecular and turbulent viscosities; k is the kinetic energy of the turbulent flow oscillations; ε is the rate of dissipation of the kinetic energy of turbulent oscillations; S_{nm} is the deformation rate tensor; and $\mathbf{q}$ is the thermal flux density vector (symbol "div" denotes the tensor field divergence operator).

1063-7850/02/2802-0167$22.00 © 2002 MAIK "Nauka/Interperiodica"

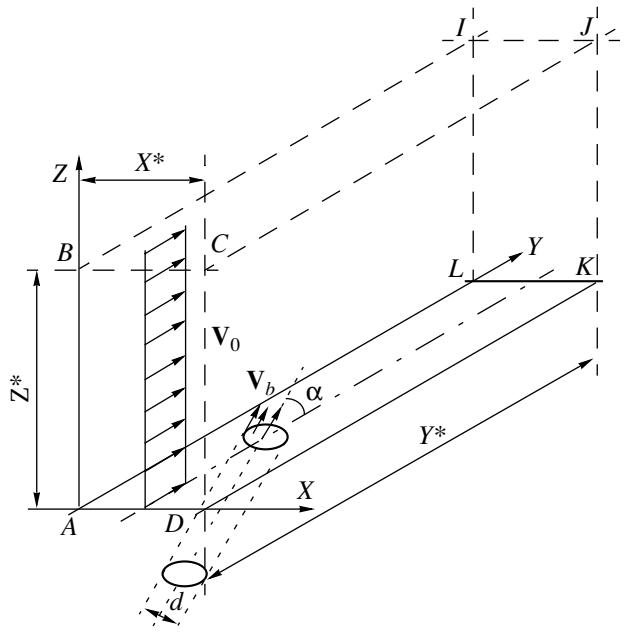

Fig. 1. Calculated flow cell configuration.

The scaling factors entering into the above system of equations are determined by the conventional expressions

$$\mathrm{Re}_0 = \frac{\rho_0 V_0 L_0}{\mu_0}, \quad \mathrm{Pr}_0 = \frac{\mu_0 C_p}{\lambda_0},$$

$$M_0 = \frac{V_0}{\sqrt{\gamma_0 R T_0}}, \quad \gamma_0 = \frac{C_p}{C_v}.$$

Here the subscript "0" indicates the scaling values of the physical quantities characterizing the main flow at the entrance of the spatial region studied: L_0 is the linear scale; Re_0 is the Reynolds number; Pr_0 is the Prandtl number; M_0 is the Mach number; C_p and C_v are the heat capacities at constant pressure and volume, respectively; λ_0 is the thermal conductivity; γ_0 is the adiabate exponent; and R is the universal gas constant. The system of equations is closed by a low-Reynolds k–ε Chen turbulence model [6].

Model description. Let us consider a gas screen formed by submerged streams of a coolant injected into the main hot flow through a system of holes in a solid wall. Taking into account the translational symmetry of the problem, we may restrict the consideration to a single elementary cell comprising one cooling stream. This will imply the use of a periodic boundary condition at the side walls of the cell. The configuration of the spatial region studied (elementary cell) is depicted in Fig. 1. The length, width, and height of this cell (expressed in units of the diameter d of a hole through which the stream is injected) amount to $X^* = 3d$, $Y^* = 26d$, and $Z^* = 11.4d$, respectively. The solid wall at which the screen is formed coincides with the plane $Z = 0$. The axis of the stream (ejected from a side channel) makes an angle α with the wall, deviating downstream toward the Y axis direction.

At the entrance of the calculated cell (*ABCD* plane), we set the distributions of dimensionless temperature, density, velocity, and turbulence characteristics of the main flow. The initial temperature ratio of the main and injected flows was $T_0/T_b = 2$. The exit cross section (*IJKL* plane) was characterized by soft boundary conditions (with zero first derivatives of all parameters in the longitudinal direction). The side edges of the cell (*ABIL* and *DCJK*) obeyed periodic boundary conditions. The top boundary (*BIJC*) was characterized by impermeability, while the bottom (solid wall) was described by the conditions of adherence and zero turbulent viscosity. The condition of impermeability on the top edge is selected in order to provide for the flow core integrity: the heat and mass exchange processes in real systems are localized in the vicinity of the protected wall surface. The pressure was set at point *I* and restored in the inner points of the spatial region studied in accordance with the main equations. The entrance cross section obeyed the condition of zero second derivative of the pressure, the side edges were characterized by periodic conditions, and all other edges were characterized by zero first derivative of the pressure [5]. A difference scheme was obtained using the conventional methods of control volumes, compressibility scaling, and splitting. The problem was solved using a method based on the vector trials. The difference scheme provided accuracy up to the second order with respect to the spatial variable and to the first order with respect to time.

Taking into account adiabaticity of the wall and restricting the consideration to small Mach numbers of the incident flow ($M_0 = 0.3$), we may assume that no boundary temperature layer is present at the wall in front of the channel output. Owing to the boundary conditions (adherence), the boundary layer is formed under the conditions of the main flow compressed by the injected stream. The injected stream was characterized by the parameter $m = \rho_b V_b/\rho_0 V_0$ representing the ratio of current densities of the injected and main flows. The calculation was performed for $\mathrm{Re}_0 = 3330$, using the hole diameter d as the linear scale. The purpose of the calculation was to determine the temperature distribution T_{ad} at the adiabatic wall, from which the efficiency parameter of the cooling screen can be calculated by the formula $\theta = (T_0 - T_{ad})/(T_0 - T_b)$

Results and discussion. Using the methods of numerical modeling with controlled boundary conditions, it is possible to study any variant of interacting flows. We will illustrate the influence of a boundary layer on the efficiency of a gas screen formed by a series of cooling streams in the case of injection at $\alpha = 90°$ with the parameter $m = 1$. When a flow is incident on a cylindrical body standing with its edge on a plate, a three-dimensional boundary layer formed on the plate exhibits breakdown with the formation of near-wall horseshoe-shaped vortices [7]. Prior to the breakdown,

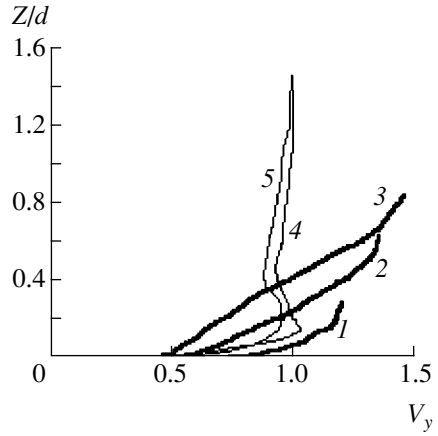

Fig. 2. Profiles of the longitudinal velocity component V_y in front of the injection hole calculated for three cross sections Y/d = 1.5 (*1*), 2.4 (*2*), and 3 (*3*) in the case of a thin boundary layer and for two cross sections Y/d = 1.5 (*4*) and 2.4 (*5*) in the case of a thick boundary layer. The ordinate Z/d is the dimensionless distance along the normal to the wall.

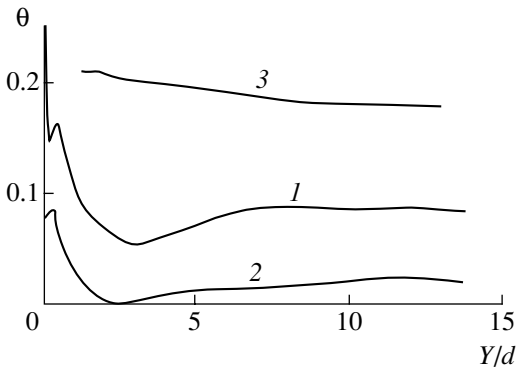

Fig. 3. Profiles of the screen efficiency θ averaged across the side stream region for m = 1 and α = 90° (Y/d is the longitudinal dimensionless coordinate): (*1*) thin boundary layer; (*2*) thick boundary layer; (*3*) theoretical calculation for the central flow region (no boundary layer).

the boundary layer exhibits certain variations. In particular, the pressure in the flow symmetry plane (meridional plane of the cylinder) across the whole boundary layer increases as a result of the flow drag on approaching the cylinder. This leads to a deformation of the longitudinal velocity profile, which varies slower in the direction of normal to the surface. A similar deformation of the boundary layer takes place in the flow incident on a submerged stream injected from a wall channel into the main flow [8]. However, the boundary layer exhibits virtually no breakdown in front of relatively weak side streams, because such streams are also injected by the surrounding medium.

Figure 2 shows the profiles of the longitudinal velocity component V_y calculated for three cross sections in front of the injection hole in the case of a "thin" boundary layer and for two cross sections in the case of a "thick" boundary layer. The case of a thick boundary layer is obtained by setting the appropriate initial velocity profile in the entrance cross section. The velocity profiles are presented for three cross sections (Y/d = 1.5, 2.4, and 3) in the flow symmetry plane X/d = 1.5. As can be seen from the data in Fig. 2, the profile of the longitudinal velocity component attains a level 1.5 times as low as that for a thin boundary layer. This is related to a deeper penetration of a side stream into the main flow, which leads to the flow drag. In addition, the side stream is significantly heated and produces no cooling action on returning to the wall.

The results of our calculations showed that, as the boundary layer thickness increases, the cooling screen efficiency θ decreases and the screen occupies a narrower layer behind the injection hole. Figure 3 shows the screen efficiency profiles averaged across the side stream. In these plots, the Y/d coordinate is measured from the rear edge of the injection hole. For comparison, we also present the screen efficiency profile calculated using a semiempirical method [4] assuming that the boundary layer is completely absent in front of the injected stream. As can be seen from Fig. 3, the absence of the boundary layer results in the maximum screen efficiency (curve *3*). The presence of even a thin boundary layer significantly decreases the efficiency (curve *1*), while a thick boundary layer leads to a further drop (curve *2*). Note that the three profiles are approximately equidistant with respect to each other.

Conclusion. The fields of the physical quantities obtained in our numerical experiments reveal the reason for a strong dependence of the cooling gas screen efficiency on the parameters of a boundary layer formed at the protected wall. A decrease in the screen efficiency with increasing boundary layer thickness is explained by the fact that the injected stream falls within a flow possessing a lower specific momentum (ρV^2) as compared to that in the main flow far from the wall ($\rho_0 V_0^2$). As a result, the stream deviates from the wall toward the main flow and the wall temperature grows.

REFERENCES

1. V. G. Lushchik and A. E. Yakubenko, Izv. Akad. Nauk, Mekh. Zhidk. Gaza, No. 6, 34 (2000).
2. S. Friendrichs, H. P. Hatson, and W. N. Dawes, Trans. ASME **119** (10), 786 (1997).
3. R. J. Goldstein, P. Jin, and R. L. Olson, Journal of Turbomachinery **121** (4), 225 (1999).
4. E. N. Bogomolov, *Working Processes in Cooled Turbines of Gas Turbine Engines with Perforated Blades* (Mashinostroenie, Moscow, 1987).
5. L. A. Zaĭkov, M. Kh. Strelets, and M. L. Shur, Teplofiz. Vys. Temp. **32** (6), 850 (1994).
6. J. Y. Chien, AIAA J. **20** (1), 33 (1982).
7. P. Chang, *Separation of Flow* (Pergamon, Oxford, 1970; Mir, Moscow, 1972), Vol. 1.
8. Y. Kamotani and I. Greber, AIAA J. **10** (11), 1425 (1972).

Translated by P. Pozdeev

Technical Physics Letters, Vol. 28, No. 2, 2002, pp. 83–86. Translated from Pis'ma v Zhurnal Tekhnicheskoĭ Fiziki, Vol. 28, No. 3, 2002, pp. 1–8.

The Phase Diagram and Properties of Solid Solutions of the Ternary Sodium–Lithium–Potassium Niobate System

L. A. Reznichenko, O. N. Razumovskaya, L. A. Shilkina, S. I. Dudkina, and A. V. Borodin

Institute of Physics, Rostov State University, Rostov-on-Don, Russia

e-mail: klevtsov@ip.rsu.ru

Received September 11, 2001

Abstract—A phase diagram of the (Na,Li,K)NbO_3 ternary system in the $NaNbO_3$ region was constructed using the experimental X-ray diffraction data. Various physical properties of solid solutions were studied in a broad range of component concentrations. Promising compositions for the high- and medium-frequency piezotransducers are determined. *© 2002 MAIK "Nauka/Interperiodica".*

This paper represents a continuation of the study of ternary systems of the (Na,Li,*A*')NbO_3 type (*A*' = $Pb_{0.5}$, $Sr_{0.5}$, $Cd_{0.5}$) reported in [1–5]. Here, the object of investigation was the xNaNbO$_3$–yLiNbO$_3$–zKNbO$_3$ system. The samples of solid solutions were prepared by two-stage solid-state synthesis (1123 K, 1.8×10^4 s; 1173 K, 1.44×10^4 s). This was followed by hot molding (19.6 MPa, 2.4×10^3 s, 1223–1473 K, depending on the composition), ensuring a sufficiently high relative density of the samples ($\rho_1 = 0.985$).*

The boundaries of single-phase regions in the (Na,Li,K)NbO_3 ternary system, the kinetics and mechanisms of interaction of the initial components, and the sequence of reactions involved in the solid-state synthesis of solid solutions were previously studied by Freĭdenfel'd *et al.* [6]. The system was considered as representing quasibinary compositions of the type $(1 - y)(Na_xK_{1-x})NbO_3$–$y$LiNbO$_3$ ($0 \le y \le 0.20$, $0.45 \le x \le 0.50$). The content of $NaNbO_3$ was varied within the limits providing for the best piezoelectric properties [7].

We have studied solid solutions belonging to six *z*-sections corresponding to the compositions with 2.5–15.0 mol % $KNbO_3$. Each of these sections was represented by a series of samples containing 1.0–15.0 mol % $LiNbO_3$. The upper limit of these *y*-sections was selected so as to restrict the series of continuous solid solutions in the (Na,Li)NbO_3 binary system to 14.5 mol % $LiNbO_3$ [8]. The upper limit of the *z*-sections was determined by the condition that a single-phase orthorhombic structure (*R* = *R*II) [9]), analogous to that realized in the (Na,Li)NbO_3 system with $0.032 \le x \le 0.118$ [10] and complicated by the phase transitions known in the (Na,K)NbO_3 system with $x > 0.15$ [7], would exist almost in the entire range of the component concentrations studied (except for a very narrow region close to $NaNbO_3$). This orthorhombic structure is characterized by a monoclinic (*M*2) perovskite subcell with the parameters $a_0 = c_0$, b_0, and $\beta \ne 90°$ related to those of the unit *R*-cell by the relationships $A = 2a_0\cos\beta/2$, $B = 2b_0$, and $C = 2a_0\sin\beta/2$. It was of interest to study (as was done previously [1–5]) only a part of the phase diagram in the $NaNbO_3$ region, where the solid solutions retain certain special properties [11] related to the proximity to this very composition.

The phase diagram of the system studied (Fig. 1) was determined by the diagrams of the component binary systems (Na,Li)NbO_3 and (Na,K)NbO_3 for the corresponding component concentrations. The

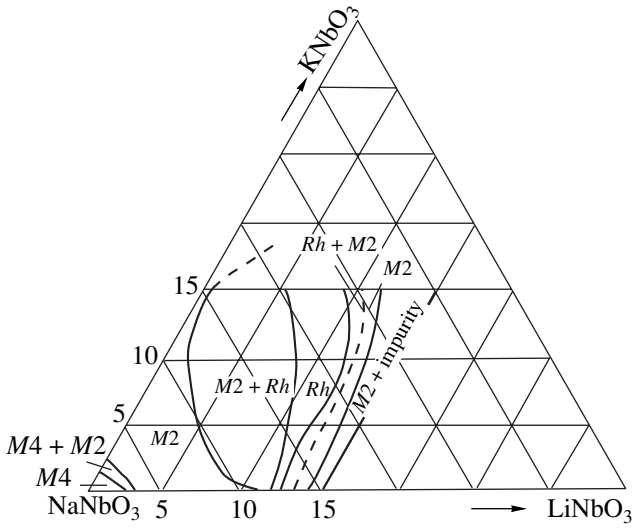

Fig. 1. The $NaNbO_3$ corner of a phase diagram of the (Na,Li,K)NbO_3 ternary system.

* $\rho_1 = \rho/\rho_2$, where ρ is the density and ρ_2 is the X-ray density.

1063-7850/02/2802-0083$22.00 © 2002 MAIK "Nauka/Interperiodica"

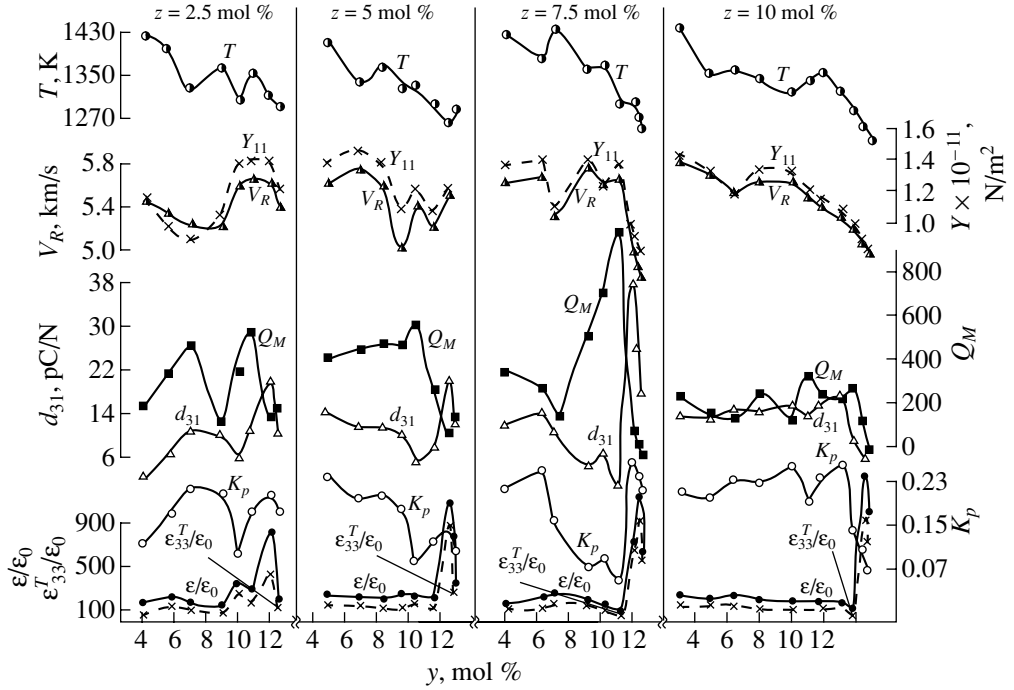

Fig. 2. The plots of some physical characteristics versus composition ($LiNbO_3$ content *y*) for solid solutions of the (Na,Li,K)NbO_3 ternary system in the sections with *z* = 2.5–10.0 mol %.

$NaNbO_3$ region is occupied by the *R*(*M*4) phase (with $B = 4b_0$), which is characteristic of this compound at room temperature [12] and transforms in both systems into the *R*(*M*2) phase through a morphotropic region containing *R*-structures of various multiplicity [13]. As the *z* value increases, the field occupied by the *R*(*M*2) phase exhibits sharp narrowing. At the same time, the boundaries of coexistence of the orthorhombic *R*(*M*2) and rhombohedral (*Rh*) phases expand to form a region with a maximum width of ~10 mol % (with respect to *y*), which is much greater as compared to ~1 mol % in the (Na,Li)NbO_3 system [8]. The *Rh* phase region also significantly expands. The right-hand boundary of the adjacent morphotropic region featuring the coexisting *Rh* + *R*(*M*2) phases is conditionally indicated by a dashed line, since a more precise determination in this narrow concentration range is difficult. The width of the next *R*(*M*2) phase region is virtually the same for all *z*.

An increase in the $LiNbO_3$ concentration above 12.0–14.5 mol % (for various *z*) leads to the formation of an insignificant amount (1.0–8.0 mol %) of the impurity phase: $LiNbO_3$ for $z < 2.5$ mol % and (Na,K)Nb_3O_8 for $z > 2.5$ mol % (the greater the $KNbO_3$ content in the system, the earlier the onset of the impurity formation). This result is consistent with the data [6] concerning a decrease in the solubility of $LiNbO_3$ in (Na,K)NbO_3 and is indicative of limitations in the solid-state synthesis of solid solutions in the system with sufficiently large $KNbO_3$ content. Note that, since no *Rh* phases appear in the (Na,K)NbO_3 system [7], the regions of *R*(*M*2) + *Rh*, *Rh*, and *Rh* + *R*(*M*2) will probably be closed for large $KNbO_3$ concentrations.

Figure 2 shows the plots of various physical characteristics versus composition, including data for the relative permittivity of samples before ($\varepsilon/\varepsilon_0$) and after ($\varepsilon_{33}^T/\varepsilon_0$) polarization, planar electromechanical coupling coefficient (K_p), piezoelectric modulus (d_{31}), mechanical figure of merit (Q_M), sound velocity (V_R), Young's modulus Y_{11}^E, and sintering temperature (*T*) for the solid solutions with *z* = 2.5–10 mol %. Table 1 gives analogous characteristics for the solid solutions with *z* = 12.5–15.0 mol %. The observed nonmonotonic behavior is obviously related to the complicated shape of the phase diagram of this ternary system, featuring a large number of interphase boundaries. Inside the morphotropic region, this behavior is probably related to a change in the phase relationships involved in the composition variations accompanied by a nonmonotonic change in the structural parameters.

Table 2 indicates the main characteristics of some solid solutions of the (Na,Li,K)NbO_3 ternary system promising from the standpoint of practical (piezoelectric) applications. Compositions 1 and 2 are characterized by a very low value of $\varepsilon_{33}^T/\varepsilon_0$ and very high V_R in combination with sufficiently large (for these $\varepsilon_{33}^T/\varepsilon_0$) K_p and d_{31} and moderate Q_M. The V_R and $\varepsilon_{33}^T/\varepsilon_0$ values are advantageous for a high-frequency operation range of

Table 1. Compositions, physical characteristics, and sintering temperatures of the (Na,Li,K)NbO_3 solid solutions with z = 12.5 and 15 mol %

Composition	T, K	ρ, g/cm^3	T_c, K	$\varepsilon/\varepsilon_0$	$\varepsilon_{33}^T/\varepsilon_0$	ρ_v, Ω m (373 K)	K_p	d_{31}, pC/N	Q_M	V_R, km/s	$Y_{11}^E \times 10^{-11}$, N/m^2
$K_{0.125}Na_{0.865}Li_{0.01}NbO_3$	1398	4.346	553	299	179	1.5×10^{10}	0.232	15.4	242	5.73	1.36
$K_{0.125}Na_{0.850}Li_{0.025}NbO_3$	1313	4.409	573	272	165	4.2×10^{8}	0.229	14.6	303	5.71	1.37
$K_{0.125}Na_{0.835}Li_{0.040}NbO_3$	1298	4.397	520	273	168	0.7×10^{10}	0.229	15.2	248	5.50	1.26
$K_{0.125}Na_{0.815}Li_{0.06}NbO_3$	1303	4.368	537	245	173	2.7×10^{9}	0.224	15.3	146	5.39	1.19
$K_{0.125}Na_{0.785}Li_{0.09}NbO_3$	1373	4.425	536	210	141	2.6×10^{9}	0.274	16.2	205	5.50	1.22
$K_{0.125}Na_{0.7875}Li_{0.0875}NbO_3$	1373	4.475	558	236	170	1.0×10^{9}	0.186	11.8	409	5.68	1.34
$K_{0.125}Na_{0.7788}Li_{0.0962}NbO_3$	1353	4.54	563	219	169	0.6×10^{10}	0.134	9.0	251	5.31	1.19
$K_{0.125}Na_{0.7656}Li_{0.1094}NbO_3$	1273	4.319	532	184	145	2.8×10^{9}	0.206	15.2	67	4.67	0.90
$K_{0.125}Na_{0.7613}Li_{0.11370}NbO_3$	1273	4.320	553	740	710	2.5×10^{9}	0.254	17.4	164	5.06	1.0
$K_{0.125}Na_{0.7545}Li_{0.1205}NbO_3$	1223	4.410	548	1070	980	0.4×10^{10}	0.206	18.0	253	5.18	1.11
$K_{0.150}Na_{0.800}Li_{0.05}NbO_3$	1418	4.357	608	250	190	1.5×10^{9}	0.170	11.4	235	5.72	1.33
$K_{0.150}Na_{0.780}Li_{0.07}NbO_3$	1363	4.486	563	258	168	1.3×10^{9}	0.226	14.2	183	5.65	1.35
$K_{0.150}Na_{0.7650}Li_{0.085}NbO_3$	1388	4.333	505	223	154	0.8×10^{10}	0.268	16.9	222	5.47	1.19
$K_{0.150}Na_{0.7665}Li_{0.0935}NbO_3$	1353	4.500	553	184	133	2.5×10^{9}	0.236	16.0	190	4.66	0.90
$K_{0.150}Na_{0.74380}Li_{0.1062}NbO_3$	1373	4.451	546	353	258	1.6×10^{10}	0.129	10.1	447	5.68	1.33
$K_{0.150}Na_{0.7895}Li_{0.1105}NbO_3$	1273	4.327	547	269	143	9.1×10^{8}	0.202	13.7	141	4.82	0.92
$K_{0.150}Na_{0.7295}Li_{0.1205}NbO_3$	1253	4.452	548	650	420	0.4×10^{10}	0.240	14.2	170	5.34	1.15

Notes: T_c is the Curie temperature; ρ_v is the bulk resistivity (at 373 K).

Table 2. Compositions, physical characteristics, sintering temperatures, and densities of (Na,Li,K)NbO_3 solid solutions promising for the piezoelectric applications

No.	Composition	T, K	$\varepsilon_{33}^T/\varepsilon_0$	$K_p(K_t)$	d_{31}, pC/N (d_{33}, pC/N)	Q_M	V_R, km/s	$Y_{11}^E \times 10^{-11}$, N/m^2	T_c, K	ρ, g/cm^3
1	$K_{0.025}Na_{0.965}Li_{0.07}NbO_3$	1333	126	0.214	11.7	473	5.28	0.88	613	4.416
2	$K_{0.025}Na_{0.885}Li_{0.09}NbO_3$	1373	101	0.210	11.3	121	5.25	1.07	653	4.243
3	$K_{0.05}Na_{0.8625}Li_{0.1235}NbO_3$	1273	906	0.135	20.7	77	5.51	1.23	520	4.435
4	$K_{0.075}Na_{0.8047}Li_{0.1202}NbO_3$	1313	725	0.266	39.5	77	5.02	1.06	560	4.477
5	$K_{0.075}Na_{0.8094}Li_{0.1156}NbO_3$	1313	161	0.055 (0.352)	3.3 (21.1)	1093	5.71	1.4	577	4.566

Note: K_t is the electromechanical coupling coefficient of the transverse oscillation mode.

piezotransducers based on these compositions. In addition, the large V_R value allows a preset frequency to be obtained using thinner piezoelectric plates, which simplifies the manufacturing technology (by increasing the resonance size of devices). Another advantage is a decrease in the transducer capacitance. Finally, a low $\varepsilon_{33}^T/\varepsilon_0$ value facilitates matching of the transducer to both generator and load. The K_p and d_{31} values provide for a sufficiently high efficiency of the piezotransducer, while the moderate Q_M accounts for a sufficiently uniform amplitude–frequency characteristic and allows the use of short pulses. A low material density leads to a significant decrease in the device weight (a decisive factor in applications such as the aerospace technologies) and in the acoustic impedance (which is also important for proper matching to the acoustic load). The high Curie temperatures T_c of these materials increase the working temperature range of the transducers.

Compositions 3 and 4 (Table 2) possessing moderate $\varepsilon_{33}^T/\varepsilon_0$ values in combination with high d_{31} and V_R can be used as a base for the active piezoelectric materials operating in the medium frequency range. The high V_R values allow medium-frequency piezotransducers to be obtained that are capable of exciting metal resonators with high sound velocities. Composition 5, which possesses a low $\varepsilon_{33}^T/\varepsilon_0$ at a high Q_M, exhibits increased anisotropy of the piezoelectric properties (K_t/K_p and $d_{33}/d_{31} \geq 6$), which favors suppression of the spurious oscillations. Such a material can be employed in the transducers for ultrasonic defect detectors, acceleration sensors, thickness meters, and in the high-frequency instrumentation for nondestructive material monitoring and medical diagnostics.

Acknowledgments. This study was supported by the Russian Foundation for Basic Research, project no. 99-02-17575.

REFERENCES

1. E. G. Fesenko, L. A. Reznichenko, L. S. Ivanova, *et al.*, Zh. Tekh. Fiz. **55** (3), 601 (1985) [Sov. Phys. Tech. Phys. **30**, 354 (1985)].
2. L. A. Reznichenko, O. N. Razumovskaya, A. Ya. Dantsiger, *et al.*, in *Proceedings of the International Scientific and Practical Conference "Piezotechnology-97", Obninsk, 1997*, p. 197.
3. L. A. Reznichenko, O. N. Razumovskaya, L. A. Shilkina, *et al.*, Zh. Tekh. Fiz. **70** (11), 58 (2000) [Tech. Phys. **45**, 1432 (2000)].
4. L. A. Reznichenko, A. Ya. Dantsiger, O. N. Razumovskaya, *et al.*, Zh. Tekh. Fiz. **70** (11), 63 (2000) [Tech. Phys. **45**, 1437 (2000)].
5. L. A. Reznichenko, O. N. Razumovskaya, L. A. Shilkina, *et al.*, Zh. Tekh. Fiz. **71** (1), 26 (2001) [Tech. Phys. **46**, 24 (2001)].
6. É. Zh. Freĭdenfel'd, M. Ya. Dambekalne, and G. D. Yanson, in *Proceedings of the III Interinstitution Conference on Methods of Production and Analysis of Ferrite, Ferroelectric and Piezoelectric Materials and Related Raw Materials, Donetsk, 1970*, p. 3.
7. B. Jaffe, W. R. Cook, and H. Jaffe, *Piezoelectric Ceramics* (Academic, New York, 1971; Mir, Moscow, 1974).
8. L. A. Shilkina, L. A. Reznichenko, M. F. Kupriyanov, and E. G. Fesenko, Zh. Tekh. Fiz. **47** (10), 2173 (1977) [Sov. Phys. Tech. Phys. **22**, 1262 (1977)].
9. E. G. Fesenko, *Perovskite Family and Ferroelectricity* (Atomizdat, Moscow, 1972).
10. L. A. Reznichenko, L. A. Shilkina, O. N. Razumovskaya, *et al.*, in *Proceedings of the International Symposium "Phase Transformations in Solid Solutions and Alloys (Oma-II)," Sochi, 2001* (in press).
11. L. A. Shilkina, I. V. Pozdnyakova, L. A. Reznichenko, *et al.*, in *Proceedings of the 8th International Symposium on Physics of Ferroelectric-Semiconductors, Rostov-on-Don, 1998*, p. 190.
12. E. G. Fesenko, A. Ya. Dantsiger, L. A. Reznichenko, *et al.*, Zh. Tekh. Fiz. **52** (11), 2262 (1982) [Sov. Phys. Tech. Phys. **27**, 1389 (1982)].
13. H. D. Megaw, Ferroelectrics **7** (1–4), 87 (1974).

Translated by P. Pozdeev

Technical Physics Letters, Vol. 28, No. 2, 2002, pp. 87–89. Translated from Pis'ma v Zhurnal Tekhnicheskoĭ Fiziki, Vol. 28, No. 3, 2002, pp. 9–14.

The Effect of Turbulent Mixing on the Dynamics of a Liquid Layer Accelerated by a Compressed Air Flow

I. G. Zhidov, E. E. Meshkov, N. V. Nevmerzhitskiĭ, I. G. Pylev†, and E. A. Sotskov

Institute of Experimental Physics, Russian Federal Nuclear Center, Sarov, Russia

e-mail: root@gdd.vniief.ru

Received September 10, 2001

Abstract—The influence of a turbulent mixing (TM), developed at the unstable boundary of a liquid layer accelerated by a hot compressed gas flow, on the efficiency of the subsequent energy transfer from the accelerated liquid layer to a gas layer compressed by the liquid was experimentally studied. It was found that the TM development may significantly decrease the energy takeoff by the accelerated liquid layer, which is explained by cooling of the hot compressed gas as a result of the increased heat transfer from gas to liquid in the TM zone. The experimental data indicate that the gas energy losses can reach several tens percent. © *2002 MAIK "Nauka/Interperiodica".*

Zababakhin [1] demonstrated the possibility of an infinite energy accumulation for a shock wave propagating in a planar self-similar layered system comprising alternating bands of heavy and light substances. If the density of a substance in the light layers is very small, these layers are strongly compressed on moving between the neighboring heavy layers and the system motion resembles a series of collisions between heavy bands separated by elastic spacers. The results of our experiments described below showed that turbulent mixing (TM), developed as a result of the acceleration of boundaries between differential density regions in these cumulative band systems, may significantly influence the process of energy accumulation.

Previously [2], we reported on the experimental investigation of the TM effect upon the dynamics of a liquid layer accelerated by a compressed gas flow. The gas–liquid boundary in this system is unstable, featuring the Rayleigh–Taylor instability development [3], which leads to the formation and development of a TM zone. In the experiments described in [2], the flow was studied in a planar system comprising a hard wall, a compressed gas layer *1*, a liquid layer, and a gas layer *2* (air at normal pressure and room temperature). The gas in layer *1* (accelerating the liquid layer) represented either compressed helium at room temperature ("cold" gas) or strongly heated products of the explosion of an acetylene–oxygen mixture ("hot" gas). The liquid layer dynamics was compared for the samples containing equal amounts (by mass) of either water, or an aqueous gelatin solution (jelly) with a small concentration (C = 4/4%) and low strength (effective stress at break, $\sigma \approx$ 0.005 MPa),* or a high-density jelly (C = 35%) in which the mixing is fully suppressed ("stabilized" layers) by an increasing strength ($\sigma \approx 0.2$ MPa).

The system studied in [2] exhibited a relative increase in the velocity of water and jelly (C = 4.4%) driven with a cold gas and jelly (C = 4.4%) driven with a hot gas in comparison with stabilized layers, which was related to a decrease in the effective thickness of the liquid layer destroyed by the TM zone in the course of acceleration. In the experiments with water accelerated by the hot gas, the relative velocity of the liquid layer decreased as a result of the intensive heat transfer from gas to liquid in the TM zone.

Below we describe the results of experiments with a planar system comprising the first hard wall, a compressed gas layer *1*, a liquid layer *3*, a compressible gas layer *2*, and the second hard wall (Fig. 1). In our experiments, gas *1* represented the products of the explosion of an acetylene–oxygen mixture and gas *2* was the air at normal pressure and room temperature. The liquid layer was either water or jelly with C = 4.4% (for the comparison, the experiments were also performed with stabilized layers of a high-density jelly).

The layer of a condensed substance (water, jelly, or a stabilized layer) with a thickness of 1.8 cm was placed into a transparent vertical container (cup), which was accelerated in a transparent cylindrical channel with a diameter of 5 cm under the action of the products of an

† Deceased.

* A characteristic pressure of the products of the explosion of an oxygen–acetylene mixture ($P \sim 1$ MPa) is far in excess of this strength level and, as a result, the low-density jelly behaves as a liquid layer. However, even this low strength significantly influences the structure of the TM zone at the unstable layer boundary and decreases the TM zone penetration into the gas [2]. The depth of the TM zone penetration for water and jelly was the same.

1063-7850/02/2802-0087$22.00 © 2002 MAIK "Nauka/Interperiodica"

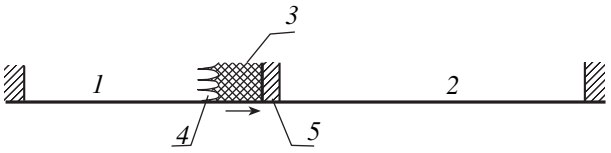

Fig. 1. A schematic diagram of the experiment on the air compression by a condensed layer accelerated by a hot compressed gas flow: (*1*) compressed gas; (*2*) compressible gas (air); (*3*) accelerated layer; (*4*) unstable gas–liquid boundary; (*5*) a layer with suppressed instability. Accelerated by the hot products of explosion of an acetylene–oxygen mixture, the container carrying the liquid layer compresses air in a closed channel.

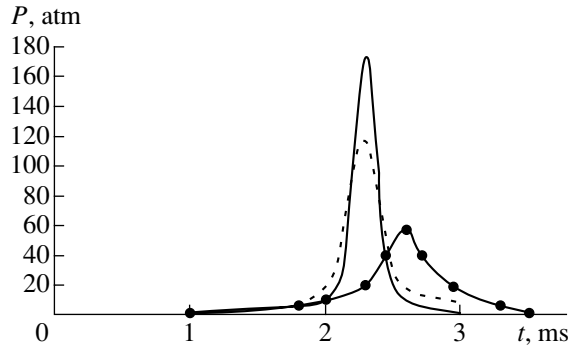

Fig. 2. Time variation of the output signals $P(t)$ of a pressure transducer in the experiments with stabilized layer (solid curve), low-density jelly (dashed curve), and water (solid curve with black circles).

explosion of a stoichiometric oxygen–acetylene mixture ($C_2H_2 + 2.5O_2$, $P \sim 1$ MPa). The total weight of the cup with a liquid layer was 60 g. In all experiments, the scatter of the liquid weight, container–wall friction force, and accelerating gas pressure did not exceed 0.1–0.2%. Each system was studied in several experimental runs. The process of the cup acceleration and stopping was monitored by a high-speed video camera.

A piezoelectric transducer mounted in the hard wall at the end of the channel monitored the pressure of the air (initially occurring under normal conditions) compressed by the moving cup. In addition, the air pressure was estimated using the $S(t)$ diagram of the cup motion determined by processing the record assuming that the gas compression proceeds under adiabatic conditions. The experimental procedure was thoroughly elaborated, and the results of the $S(t)$ determination were reproducible to within 1–2%.

Thus, in the first stage of our experiment, the energy of accelerating gas was converted into the energy of an accelerated liquid layer; in the stage of air compression by the moving cup, this energy was converted into the internal energy of the gas. Figure 2 shows the output signal of the piezoelectric transducer measuring the pressure of the air compressed by the cup carrying the accelerated layer of water, jelly, or a stabilized medium.

For liquid layers of the same type, the $P(t)$ curves obtained by different methods are close. The maximum degrees of compression achieved with various liquids are different. The highest compression ($P_{max} \approx 180$ atm) was obtained with a stabilized layer; a somewhat lower compression level ($P_{max} \approx 140$ atm) was achieved with jelly, and the minimum air compression ($P_{max} \approx 60$ atm) was provided by water. In addition, the time required for the maximum air compression by water was approximately 25% longer as compared to the values for the jelly and stabilized layers.

Let us estimate the energy transferred by an accelerated liquid layer to the compressed air. The relative energy gain is

$$k = (E_m - E_0)/E_0, \quad (1)$$

where E_m and E_0 are the final and initial energies of the compressed air, respectively. Considering air as the ideal gas, assuming the process to be adiabatic ($\gamma = 1.4$), and taking into account that

$$E = PV/(\gamma - 1) \quad \text{and} \quad PV^\gamma = \text{const},$$

we can express k as follows:

$$k = (P_{max}/P_0)^{(\gamma-1)/\gamma} - 1, \quad (2)$$

where P_0 is the initial air pressure.

The difference in the energy takeoff from the accelerating gas between the liquid layers featuring TM and the stabilized layer can be characterized by the factor δ_e showing the relative increase in the energy gained by the compressed air:

$$\delta_e = (\langle k \rangle_1 - \langle k \rangle_{2/3})/\langle k \rangle_1. \quad (3)$$

This quantity describes the relative energy "losses" as a result of the TM development. Here, the angle brackets denote averaging over experimental runs in the same system. The subscripts 1–3 refer to the results obtained in the experiments with different layers: stabilized layer, water, and jelly, respectively. In terms of this characteristic, the relative energy losses in our experiments with jelly and water layers were $\delta_e = 0.17 \pm 0.1$ and 0.34 ± 0.1, respectively. Similar to δ_e, we can determine a relative decrease in the amount of work performed by water and jelly on the compressed air (δ_A) and a relative decrease in the intensity of pressure pulses (δ_i). Calculated using our experimental data, these characteristics were $\delta_A = 0.22 \pm 0.13$, $\delta_i = 0.3 \pm 0.1$ for jelly and $\delta_A = 0.39 \pm 0.15$, $\delta_i = 0.4 \pm 0.1$ for water.

The results of our experiments showed that the intensive heat transfer from the hot gas to the dispersed liquid layer in the TM zone, as well as a reduction of the effective liquid layer thickness, lead to a significant

decrease in the energy subsequently transferred to the compressed air. Considerably greater losses observed for the water layer as compared to the jelly layer can be related to a higher degree of water dispersion: in the jelly, a minimum particle size in the TM zone, albeit very small, is still limited by a finite strength.

The whole body of the experimentally determined parameters indicates that turbulent mixing may significantly decrease the efficiency of the energy transfer in the chain (potential energy of a compressed hot gas) ⟶ (kinetic energy of a liquid layer) ⟶ (internal energy of a compressed gas). This decrease is related both to a decrease in the effective mass of the accelerated liquid layer and to a heat transfer from hot gas to liquid particles in the zone of turbulent mixing.

Acknowledgments. This study was supported by the Los Alamos National Laboratory (USA), contract no. B70040006-35 T3 018.

REFERENCES

1. E. I. Zababakhin, Zh. Éksp. Teor. Fiz. **49** (2), 721 (1965).
2. I. G. Zhidov, E. E. Meshkov, and N. V. Nevmerzhitskiĭ, Vopr. At. Nauki Tekh., Ser. Teor. Prikl. Fiz., Nos. 1–2, 20 (1996).
3. G. I. Taylor, Proc. R. Soc. London, Ser. A **201**, 192 (1950).

Translated by P. Pozdeev

Technical Physics Letters, Vol. 28, No. 2, 2002, pp. 90–92. Translated from Pis'ma v Zhurnal Tekhnicheskoĭ Fiziki, Vol. 28, No. 3, 2002, pp. 15–20.

The Electromagnetic Envelope Soliton Propagating in a Dielectric

A. N. Volobuev[a,*] and V. A. Neganov[b]

[a] *Samara State University, Samara, Russia*

** e-mail: volobuev@samaramail.ru*

[b] *State Academy of Telecommunications and Informatics, Samara, Russia*

Received September 5, 2001

Abstract—The interaction of electromagnetic radiation with a dielectric medium is described in terms of the Schrödinger equation with a logarithmic nonlinearity, and a single-soliton solution to this equation is found. It is shown that an envelope of the electromagnetic wave momentum varies according to the Gauss law. The wave momentum is calculated for certain values of the dielectric medium and the incident wave parameters. © *2002 MAIK "Nauka/Interperiodica".*

Let us consider the one-dimensional problem whereby the electromagnetic field interacts with a dielectric medium characterized by a certain number density n of centrosymmetric atoms (oscillators). A wave equation for the electric field component E can be written as

$$\frac{\partial^2 E}{\partial X^2} - \frac{1}{V^2}\frac{\partial^2 E}{\partial t^2} = \frac{n}{\varepsilon_0 V^2}\frac{\partial^2 P}{\partial t^2}. \quad (1)$$

Here, P is the polarization vector of a single atom, V is the phase velocity in the medium, ε_0 is the dielectric constant, X is the coordinate measured in the direction of wave propagation, and t is the current time.

According to Newton's second law for the oscillator motion [1],

$$\frac{\partial^2 P}{\partial t^2} + \omega_0^2 P = \frac{e^2}{m} NE, \quad (2)$$

where e and m are the electron charge and mass, respectively; N is the probability of excitation of the atom; and ω_0 is the fundamental frequency of the oscillator. Substituting the polarization derivative from (2) into (1), we obtain

$$\frac{\partial^2 E}{\partial X^2} - \frac{1}{V^2}\frac{\partial^2 E}{\partial t^2} = \frac{ne^2}{\varepsilon_0 m V^2} NE - \frac{n\omega_0^2 P}{\varepsilon_0 V^2} = \frac{1}{V^2}\left(\frac{ne^2}{\varepsilon_0 m} N - \omega_0^2 \chi\right) E, \quad (3)$$

where $\chi = \dfrac{nP}{\varepsilon_0 E}$ is the dielectric susceptibility.

Let us describe the electric field strength transformation by the formula

$$E(X, t) = \Phi(X, t)\exp(-i\omega_0 t), \quad (4)$$

where the function $\Phi(X, t)$ varies with time slower than does the field strength $E(X, t)$. Substituting expression (4) into Eq. (3) and ignoring small terms on the order of $1/V^2$, we arrive at

$$2i\frac{\omega_0}{V^2}\frac{\partial \Phi}{\partial t} + \frac{\partial^2 \Phi}{\partial X^2} = -\left(\frac{\varepsilon\omega_0^2}{V^2} - \frac{ne^2}{\varepsilon_0 m V^2} N\right)\Phi, \quad (5)$$

where $\varepsilon = 1 + \chi$ is the relative dielectric permittivity (the quantity ω_0 is on the order of V, $\omega_0 \sim V$).

When an electromagnetic wave is incident on the surface of a substance, the interaction of this wave with the medium obeys the Bouguer law

$$I = I_0 \exp(-\alpha l), \quad (6)$$

where α is the index describing the wave attenuation in the substance, l is the characteristic interaction length, and I_0 is the incident wave intensity. The electromagnetic wave absorption in the form of energy dissipation in the substance will be ignored: the wave is attenuated only due to the energy reradiation by atoms of the medium.

Since the wave intensity is proportional to the squared electric field strength, $I \sim E^2$, Eq. (6) can be written as

$$|E| = |E_0| \exp\left(-\frac{\alpha}{2} l\right). \quad (7)$$

The interaction index can be expressed as $\alpha = \sigma n$, where σ is the effective cross section of the wave–oscil-

lator interaction. This yields

$$\alpha l = \sigma n l = n V_{\text{ef}} = n V \frac{V_{\text{ef}}}{V} = M \frac{V_{\text{ef}}}{V} = MN, \quad (8)$$

where V_{ef} is the effective interaction volume. In deriving formula (8), we divided and multiplied the right-hand part by the geometric volume V containing M particles interacting with the wave. Then we took into account that $\frac{V_{\text{ef}}}{V} = N$, since the ratio of the effective interaction volume to the geometric volume characterizes the probability of interaction of the electromagnetic wave with particles in this volume, that is, the excitation probability.

Using relationships (4) and (7), we obtain

$$N = -\frac{2}{M}\ln\left|\frac{E}{E_0}\right| = -\frac{2}{M}\ln\left|\frac{\Phi}{\Phi_0^*}\right|, \quad (9)$$

where $E_0 = \Phi_0^* \exp(-i\omega_0 t)$. Since the polarization vector P in Eq. (1) refers to a single atom, we take $M = 1$.

Formula (9) requires some consideration. For $E < E_0$ (which reflects the process of wave absorption by an atom), we obtain $N > 0$ and the classical description of the electromagnetic wave interaction with the atom is acceptable. The case of $E > E_0$ implies reradiation of the wave, whereby $N < 0$ and this quantity can no longer be interpreted as the atomic excitation probability. The latter case requires a quantum-mechanical description of the process of wave interaction with a two-level atomic energy system. Here, the quantity N, called the average occupation number (since electrons are fermions, $-1 < N < 1$), serves as a measure of inversion of the system of radiating atoms [2]. For $N = -1$, all charges are in the ground state [1].

Substituting formula (9) into Eq. (5) and taking into account that $\varepsilon_a = \varepsilon\varepsilon_0$ is the absolute permittivity of the medium, we obtain

$$2i\frac{\omega_0}{V^2}\frac{\partial\Phi}{\partial t} + \frac{\partial^2\Phi}{\partial X^2} = -\left(\frac{\varepsilon\omega_0^2}{V^2} + \frac{2\varepsilon n e^2}{\varepsilon_a m V^2}\ln\left|\frac{\Phi}{\Phi_0^*}\right|\right)\Phi. \quad (10)$$

Introducing the notation

$$\omega_*^2 = \frac{2ne^2}{\varepsilon_a m}, \quad (11)$$

we arrive at the equation

$$i\beta\frac{\partial\Phi}{\partial t} + \frac{V_n}{k}\frac{\partial^2\Phi}{\partial X^2} = -\omega\left(\ln\left|\frac{\Phi}{\Phi_0}\right|\right)\Phi, \quad (12)$$

where $\beta = 2\frac{r}{k}$, r, and δ are constant quantities; $V_n = \frac{\omega}{k}$ is the group velocity of the wave packet; $|\Phi_0| = |\gamma\Phi_0^*|$; and $\gamma = \exp\left(-\frac{\omega_0^2}{\omega_*^2}\right)$.

A solution to Eq. (12) can be found in the following form [3]:

$$\Phi = |\Phi_0| f(kX - \omega t)\exp[i(rX - \delta t)]. \quad (13)$$

Substituting (13) into (12) and accomplishing simple transformations, we obtain

$$\Phi = |\Phi_0|\exp\left(\frac{r^2}{k^2} - 2\frac{\delta r}{\omega k} + \frac{1}{2}\right) \times \exp\left[-\frac{(kX - \omega t)^2}{4}\right]\exp[i(rX - \delta t)]. \quad (14)$$

Solution (14) describes a solitary wave with an envelope described by the Gauss law and the system parameters obeying the relationships

$$\frac{\omega}{rk} = \frac{V^2}{\omega_0}; \quad \frac{V_n}{r} = \frac{V^2}{\omega_0}; \quad \frac{\varepsilon\omega_*^2}{\omega_0} = \frac{\omega k}{r}; \quad \frac{\omega}{r} = \frac{\omega_* V\sqrt{\varepsilon}}{\omega_0}.$$

The simplest form of solution (14) corresponds to $V_n \approx V \approx c$, where c is the velocity of light in vacuum. This is valid for a rarefied dielectric medium where $\varepsilon \approx 1$. In this case, $r = \frac{\omega_0}{c}$, $\omega_* = \omega$, and $\frac{r}{k} = \frac{\omega_0}{\omega_*}$. Taking into account that $|\Phi_0| = |\gamma\Phi_0^*|$ and using the definition (4), we obtain

$$E = |E_0|\exp\left(\frac{1}{2} - 2\frac{\delta r}{\omega k}\right) \times \exp\left[-\frac{(kX - \omega t)^2}{4}\right]\exp[i(rX - \delta t - \omega_0 t)]. \quad (15)$$

For the filling wave and the whole wave packet propagating at the velocity c, the relationship $r = \frac{\omega_0}{c}$ yields $\delta = 0$. Then formula (15) simplifies to

$$E = |E_0|\exp\left(\frac{1}{2}\right) \times \exp\left[-\frac{(kX - \omega t)^2}{4}\right]\exp[i(rX - \omega_0 t)]. \quad (16)$$

Let us consider some numerical estimates. Modern lasers are capable of generating pulses with the durations T from 10^{-9} to 10^{-12} s [2, 4] and the corresponding cyclic frequencies ranging within $\omega = 2\pi/T = 6.28(10^9–10^{12})$ s^{-1}. Taking into account the definitions $\omega_* = \omega$ and (11), we can estimate the corresponding

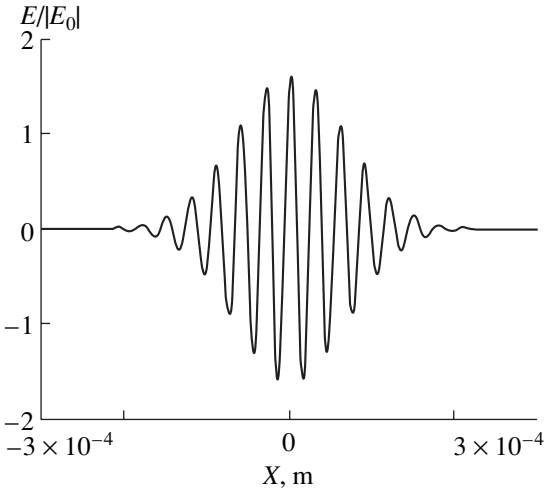

Figure.

number density as $n = 6.2(10^{15}–10^{21})$ m^{-3}. For the air under normal conditions, the number density of molecules is 2.7×10^{25} m^{-3} and, hence, the assumption of a rarefied dielectric medium is satisfied.

The estimated number density of atoms indicates that we may ignore the backscattering of electromagnetic waves (this is possible for $n < 10^{24}$ m^{-3} [2]). Therefore, Eq. (16) may describe a soliton appearing in the case of a self-induced transparency. For the calculation, we take $\omega = 6.28 \times 10^{12}$ s^{-1}, which corresponds to a wave packet length of $\lambda = 3 \times 10^{-4}$ m. The filling wave period is taken equal to $T = 10^{-13}$ s, which corresponds to a cyclic frequency of $\omega_0 = 6.28 \times 10^{13}$ s^{-1}; the corresponding wavenumbers are $k = \frac{\omega}{c} = 2.1 \times 10^4$ m^{-1} and $r = \frac{\omega_0}{c} = 2.1 \times 10^5$ m^{-1}. The plot of $E(X)/|E_0|$ calculated using formula (16) for the above constant parameters at $t = 0$ is presented in the figure.

The solutions (14)–(16) exhibit a soliton character. Unfortunately, a two-soliton solution to Eq. (12) is unknown. However, our recent numerical analysis [5] of the interaction of solitary waves described by Eq. (12) showed that the waves behave as solitons.

REFERENCES

1. M. J. Ablowitz and H. Segur, *Solitons and the Inverse Scattering Transform* (SIAM, Philadelphia, 1981; Mir, Moscow, 1987).
2. R. K. Dodd, J. C. Eilbeck, J. D. Gibbon, and H. C. Morris, *Solitons and Nonlinear Wave Equations* (Academic, London, 1984; Mir, Moscow, 1988).
3. G. B. Whitham, *Linear and Nonlinear Waves* (Wiley, New York, 1974; Mir, Moscow, 1977).
4. G. L. Lamb, *Elements of Soliton Theory* (Wiley, New York, 1980; Bibfizmat, Mogilev, 1997).
5. A. N. Volobuev, V. A. Neganov, and V. Yu. Bolochagin, Fiz. Volnovykh Protsessov Radiotekh. Sist. (Samara) **3** (1), 12 (2000).

Translated by P. Pozdeev

Technical Physics Letters, Vol. 28, No. 2, 2002, pp. 93–95. Translated from Pis'ma v Zhurnal Tekhnicheskoĭ Fiziki, Vol. 28, No. 3, 2002, pp. 21–28.

Features of the Electrodiffusion-Plastic Deformation of Silicon

M. A. Aliev, Kh. O. Alieva, V. V. Seleznev, B. G. Aliev, and Sh. R. Mutalibov

Institute of Physics, Dagestan Scientific Center, Russian Academy of Sciences, Makhachkala, Dagestan, Russia
e-mail: Kamilov@datacom.ru

Received August 22, 2001

Abstract—The effect of a change in the electron subsystem of a single crystal, caused by the electric-field-assisted transfer of impurity atoms, on the features of electroplastic deformation in silicon was studied. The new method of action upon the motion of dislocations revealed a considerable decrease in the yield point and an increase in the general plasticity as compared to those observed in the material deformed by traditional methods. Possible mechanisms explaining the observed effects are considered. © *2002 MAIK "Nauka/Interperiodica".*

The physical properties of a crystal in a preset direction can be modified only under nonequilibrium conditions, in particular, using various methods of plastic deformation [1]. Subject to various excitation factors, a plastically deformed crystal featuring mass and charge transfer represents a complicated self-organizing system [2].

Silicon belongs to the class of substances possessing maximum possible values of the theoretical tensile and shear strength, which is explained by a high degree of orientation of the covalent bonds between atoms. This factor accounts for a high resistance of the crystal lattice to the dislocation slippage even in the Si(111) plane. However, practical use of the high strength properties of atomic semiconductors is limited by low-temperature brittleness [3]. In connection with this, the development of methods for increasing the low-temperature plasticity and the study of the structure–property relationships of such crystals are important from the standpoint of both basic knowledge and practical applications. However, the separate study of diffusion, deformation, and dislocation motion phenomena in various crystals did not answer many questions encountered in the analysis of the structure-sensitive properties of these materials [4–6].

Using a technological approach, called electroplastic deformation [7], it is possible to combine the aforementioned physical phenomena in one experiment performed on a common setup. Recently [8], we have established that a new approach to crystal structuring can be even more informative and provide for a broader spectrum of influence on the physical properties of crystals as compared to the traditional methods, albeit at the expense of a rather complicated experimental technique.

As is known, an increase in the number of parameters acting on a deformed crystal leads to the formation of a greater number of defect structures possessing different properties [9]. An important factor in the generation of dislocations by means of electron bond breaking is the possibility of significantly reducing the temperature of deformation. Indeed, no paramagnetic centers were observed in silicon crystals strained at $T > 800$ K [10].

We have studied p-type silicon single crystals possessing a rectangular shape with dimensions $15 \times 10 \times 5$ mm, the edges of which coincided with the crystallographic directions [110], $[1\bar{1}0]$, and [112] deviating by 10° from the axis of deformation. The crystal was cut along the narrow side into two halves, anode and cathode, after which a diffusant (indium) was deposited onto the cleaned, cut, wide faces by thermal evaporation in high vacuum. Then the two halves with the diffusant layers were pressed against each other between plungers of a pressing deformation machine to form a diffusion source of the infinitely thin layer type. The electric-field-assisted diffusion was conducted in the [110] direction coinciding with the axis of compression. The current density in the sample varied, depending on the temperature of deformation, from 1.0×10^8 to 1.5×10^8 A/m^2, which corresponded to a voltage drop of 1.0–0.6 V. The current power dissipated in the sample reached up to 100 W.

The essence of a new method of plastic deformation of semiconductor crystals, called electrodiffusion-plastic deformation (EDPD), is as follows. Heating a sample by a high-density dc current and the electric field created in the sample lead to the electrodiffusion of impurity atoms along the field. In the case of the electroplastic deformation (EPD), the diffusion of the impurity proceeds from the side surface along the preferred dislocation yield direction, that is, across the applied electric field. The EDPD profess can be performed in either dynamic or static mode, with the parameters monitored using a two-coordinate recorder. The load is measured using a tensodynamometric transducer, while the displacements are measured with an inductive transducer.

1063-7850/02/2802-0093$22.00

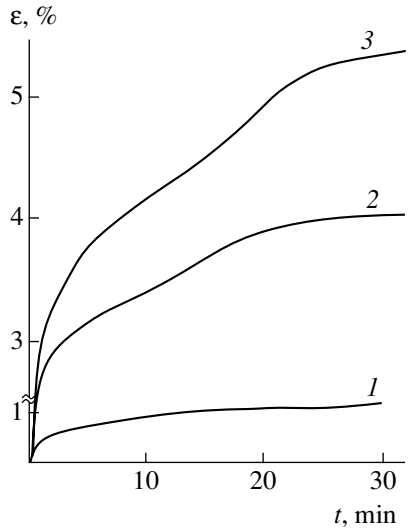

Fig. 1. Time variation of the deformation $\varepsilon(t)$ in silicon crystals loaded to $\tau = 30$ MPa at $T = 750$°C in the (*1*) TPD, (*2*) EPD, and (*3*) EDPD modes.

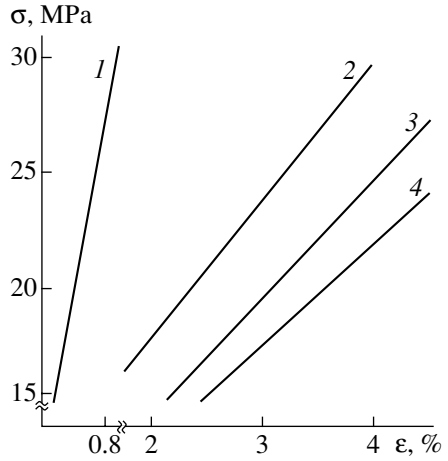

Fig. 2. The stress–strain plots $\sigma(\varepsilon)$ for silicon crystals loaded at $T = 750$°C in the (*1*) TPD, (*2*) EPD, (*3*) EDPD (cathode), and (*4*) EDPD (anode) modes.

Figure 1 shows typical curves of the shear deformation as a function of time $\varepsilon(t)$ measured in a sample deformed in three different modes: thermoplastic (TPD), electroplastic (EPD), and electrodiffusion-plastic deformation (EDPD). The TPD data were obtained using a sample deformed at a temperature of T_D = 800°C because the crystal heated to lower temperatures could not be deformed to any significant extent for the loads and times employed in the EDPD mode.

The initial linear portions regions of all $\varepsilon(t)$ curves describe the regime of loading in the course of deformation. The end points of these portions characterize the difference between various deformation modes. As can be seen from Fig. 1 (cf. curves *1–3*), the EDPD mode differs from the other regimes both by a greater deformation rate on loading and by the higher deformation level reached under otherwise equal experimental conditions. After the first five minutes of loading, all curves attain the state of stationary creep. The slope of curves *1–3* in Fig. 1 is evidence of the incomplete plastic flow in the samples studied.

In view of a considerable advantage of the EDPD mode over the other deformation regimes, it was of interest to study separately the contributions to plasticity in the anode and cathode parts of the loaded samples. For this purpose, the $\varepsilon(t)$ monitoring in the creep state of a sample deformed in the EDPD mode was accompanied by determination of the plasticity in the anode and cathode parts using the formula

$$\varepsilon = \frac{\Delta L}{L} \times 100\%, \qquad (1)$$

where ΔL is the difference between the sample lengths before and after deformation and L is the initial length of the sample. Data on the relative deformations of the anode and cathode parts calculated by formula (1) for the silicon crystals deformed in the EPD and EDPD modes are summarized in Table 1.

Figure 2 shows the stress–strain $\sigma(\varepsilon)$ plots constructed using several averaged points for various deformation modes. The process of deformation in the applied electric field accompanied by the electric-field-assisted diffusion of impurity (indium) atoms, which is much more effective as compared to the other regimes, is worthy of special attention. Note that each point in the $\sigma(\varepsilon)$ curves was determined upon deforming the sample for 30 min at a constant load. As can be seen from Fig. 1 (curves *1–3*), attaining the stationary creep state is characterized by different jumps and rates of the deformation. Note a difference in the behavior of $\sigma(\varepsilon)$ curves plotted for the anode and cathode parts of the

Table 1. Comparative data on the deformation of the anode and cathode parts of silicon crystals

No.	Deformation mode	Deformation temperature *T*, °C	Load, MPa	Relative deformation		
				total	anode	cathode
1	EPD	750	15	2.25	2.4	2.1
2	EPD	750	20	3.30	3.54	3.06
3	EDPD	750	25	4.35	4.66	4.04
4	EDPD	750	30	5.30	5.80	4.80

Table 2. The results of analysis of the experimental data in terms of formula (2)

No.	Deformation mode	Deformation temperature T, °C	Compliance coefficient K	Deformation ε*	Load interval, MPa
1	TPD	800	0.4	–0.6	15–30
2	EPD	750	1.66	–0.98	10–30
3	EDPD (anode)	750	2.3	–1.10	10–30
4	EDPD (cathode)	750	2.0	–0.90	10–30

samples. The anode part is deformed much more effectively than the cathode part.

An analysis of the linear plots *1–4* in Fig. 2 shows that the stress–strain relationship can be described by the formula

$$\varepsilon = K\sigma + \varepsilon^*, \quad (2)$$

where K is compliance coefficient and ε* is the effective deformation. By comparing the K and ε* values determined by fitting the experimental data to formula (2), we may trace a difference in the variation of plasticity. The results of this analysis of the experimental data are summarized in Table 2. As can be seen, the K value for the EDPD mode is large in comparison to the analogous parameters determined for the other regimes. Another interesting feature is the presence of large negative ε* values. In our opinion, the features in the plasticity behavior observed in silicon crystals deformed in the EDPD mode can be explained as follows.

When a crystal is deformed in the applied electric field, the charged dislocations are subject, besides the mechanical stresses, to an additional force e^*E, where e^* is the effective dislocation charge and E is the electric field strength [11]. Under the aforementioned experimental EDPD conditions, the following situation may take place: (i) the dislocations are charged and move in the preferred direction with a higher mobility as compared to that of the neutral dislocations [12]; (ii) the impurity ions may be redistributed in the vicinity of dislocations and act upon the latter as a result of the predominant diffusion toward the anode [13]. It should be also noted that all structural units involved in the diffusion-deformation process—including intrinsic and impurity atoms, charged carriers (holes), and the dislocations generated simultaneously with the holes—may interact with each other in the dynamic flow in a certain preferred direction.

Thus, a silicon crystal deformation in the EDPD mode is facilitated by an additional factor (electrodiffusion) perturbing the dislocation system. At a high current density stimulating the motion of charged defects in the samples, the deformation may be accelerated as observed in our experiments. Provided there is a certain level of the energy and mass flux intensity (doping impurity), the EDPD-deformed silicon crystals may feature processes maintaining the active regimes of self-consistent autocatalytic and coherent collective motions [14].

We believe that the proposed method of a multiparametric action upon the electron subsystem of a deformed crystal is a convenient means of controlling the structure and properties of semiconductor crystals.

REFERENCES

1. G. Nicolis and I. Prigogine, *Self-Organization in Non-Equilibrium Systems* (Wiley, New York, 1977; Mir, Moscow, 1979).
2. V. S. Ivanova, A. S. Balankin, and I. Zh. Bunin, *Synergetics and Fractals in Materials Science* (Nauka, Moscow, 1994).
3. V. I. Trefilov, Yu. V. Mil'man, and I. V. Gridneva, Izv. Akad. Nauk SSSR, Neorg. Mater. **20** (6), 958 (1984).
4. Yu. V. Kornyushin, *Transport Phenomena in Real Crystals in External Fields* (Naukova Dumka, Kiev, 1986).
5. G. M. Makushok, *Self-Organization of Deformation Processes* (Nauka i Tekhnika, Minsk, 1991).
6. *Thin Films: Interdiffusion and Reactions*, Ed. by J. M. Poate, K. Tu, and J. Meier (Wiley, New York, 1978; Mir, Moscow, 1982).
7. M. A. Aliev and V. V. Seleznev, *Electroplastic Deformation of Semiconductor Crystals*, Preprint, IF DNTs RAN (Institute of Physics, Dagestan Scientific Center, Russian Academy of Sciences, Makhachkala, 1989).
8. M. A. Aliev, Kh. O. Aliev, and V. V. Seleznev, Fiz. Tverd. Tela (St. Petersburg) **41** (6), 1028 (1999) [Phys. Solid State **41**, 936 (1999)].
9. G. A. Malygin, Usp. Fiz. Nauk **69** (9), 979 (1999).
10. F. D. Wohler, H. Alexander, and W. Sander, J. Phys. Chem. Solids **31**, 1381 (1970).
11. G. A. Kontorova, Fiz. Tverd. Tela (Leningrad) **9** (4), 1235 (1967) [Sov. Phys. Solid State **9**, 961 (1967)].
12. E. E. Vdovin and A. Yu. Kasumov, Fiz. Tverd. Tela (Leningrad) **30** (1), 311 (1988) [Sov. Phys. Solid State **30**, 180 (1988)].
13. B. I. Boltaks, *Diffusion and Point Defects in Semiconductors* (Nauka, Leningrad, 1972).
14. A. I. Olemskiĭ and I. A. Sklyar, Usp. Fiz. Nauk **162** (6), 29 (1992) [Sov. Phys. Usp. **35**, 455 (1992)].

Translated by P. Pozdeev

Technical Physics Letters, Vol. 28, No. 2, 2002, pp. 96–98. Translated from Pis'ma v Zhurnal Tekhnicheskoĭ Fiziki, Vol. 28, No. 3, 2002, pp. 29–35.

Investigation of the Frequency Characteristics of Solid-State Layer Heterostructures in Charge-Coupled Devices

V. P. Zayarny

Volgograd State University, Volgograd, Russia

e-mail: rrn2000@mail.ru

Received July 5, 2001

Abstract—The effect of charge transfer processes, induced by an SHF electric field in solid-state layer heterostructures of the metal–polycrystalline silicon–dielectric–semiconductor type, on the frequency characteristics of related charge-coupled devices (CCDs) was studied. Using the experimental plots of charge transfer inefficiency versus charging characteristics of the solid-state structures studied, it is possible to judge the ability of CCDs to operate in the SHF and EHF frequency range. Factors determining the low-frequency boundary of the working range of CCDs were not studied. © *2002 MAIK "Nauka/Interperiodica".*

Charge-coupled devices (CCDs) based on layer heterostructures [in our case, of the metal (Al)–polycrystalline silicon (Si*)–dielectric (SiO_2)–semiconductor (Si) type] represent a periodic sequence of such layers to which phase-shifted pulses of the electric field are applied so as to transfer the charge packets [1]. For CCDs operating in a high-frequency range, it is necessary to provide for the needed frequency of signals transferring the charge packets and to ensure the corresponding rate of charging processes in the heterostructure.

It was established [1] that the high-frequency properties of CCDs are determined by the following physical mechanisms. For relatively small charge packets, the dominating charge transfer mechanism is thermal diffusion. In this case, the total charge exponentially decreases with a time constant of $\tau = 4L^2/\pi^2 D_n$, where L is the transfer electrode length and D_n is the coefficient of diffusion of the minority charge carriers.

The transfer of relatively large charge packets proceeds by self-induced drift in a longitudinal electric field proportional to the gradient of the signal charge surface density. However, even in the absence of a signal charge, there exists a longitudinal (edge) electric field at the dielectric boundary under the transfer electrode. This field favors accelerated charge transport in the last transfer stage, when the self-induced field strength is smaller than that of the edge field [2–4].

Thus, the high-frequency characteristics of CCDs can be improved by reducing the gate length L or by using semiconductors with maximum charge carrier mobility, the best of which is gallium arsenide. The GaAs-based CCDs are capable of operating at a frequency of up to 500 MHz for the charge transfer inefficiency of $\varepsilon_{ss} \approx 10^{-4}$. It was demonstrated [2] that, by enhancing the edge electric field, it is possible to increase the working frequency range up to 1 GHz. The possibility of further increasing the CCD operation rate was not studied. Assuming that the CCD structures at extremely high frequencies possess the properties of microstrip (coplanar [5]) lines and using the electrodynamic properties of such systems, we can significantly enhance the effect of the edge fields on the charge packet transfer in the longitudinal direction and, hence, increase the CCD operation rate. However, this is only possible provided that the influence of charging processes in the allowed states of monoenergetic levels in the forbidden band of the semiconductor is minimized.

Figure 1 presents data on the charge packet transfer inefficiency ε_{ss} (experimentally determined as

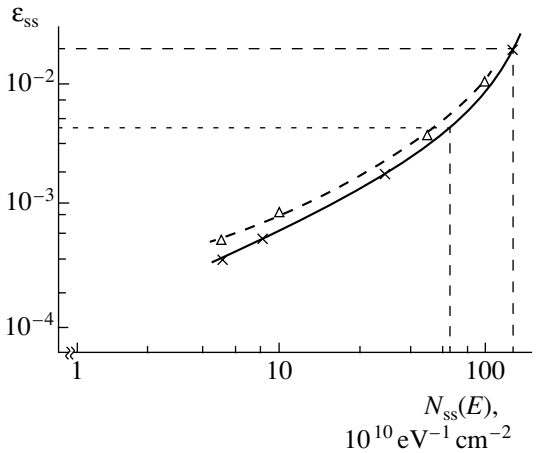

Fig. 1. Charge packet transfer inefficiency ε_{ss} versus the average density $N_{ss}(E)$ of surface states in the linear CCDs studied: (solid curve) experiment; (dashed curve) theory.

1063-7850/02/2802-0096$22.00 © 2002 MAIK "Nauka/Interperiodica"

described in [1]) for the linear CCDs studied. The ε_{ss} value is plotted versus the average density $N_{ss}(E)$ of surface states in the semiconductor at the boundary with the dielectric. Here, the best and worst charge transfer inefficiencies are observed for the maximum and minimum average $N_{ss}(E)$ values, respectively. The $N_{ss}(E)$ values were determined at a constant clock frequency ($f = 10^5$ Hz) used for the formation of charge transfer pulses and at a constant number of charge packets ($n = 32$) transferred in the CCD array. It was found that CCDs satisfactorily operate in the regime of image signal formation up to a boundary value of the charge transfer inefficiency on the order of $\varepsilon_{ss1} = 5 \times 10^{-3}$. In Fig. 1, the ε_{ss1} value corresponds to an average density $N_{ss}(E)$ of surface states in the CCD heterostructures studied $N_{ss1}(E) = 6.5 \times 10^{11}$ eV^{-1} cm^{-2}. In the logical signal processing mode, the CCDs can operate up to $\varepsilon_2 = 2 \times 10^{-2}$, which corresponds to $N_{ss2}(E) = 1.1 \times 10^{12}$ eV^{-1} cm^{-2}.

The corresponding theoretical relationship is as follows [2]:

$$\varepsilon_{ss} = (qkTN_{ss}/C_dV_g)\ln(p+1), \qquad (1)$$

where q is the elementary charge, k is the Boltzmann constant, T is the absolute temperature, C_dV_g is the surface density of the signal charge, and p is the number of CCD phases. In our case, the theoretical curve calculated for $C_d \approx 110$ pF, $V_g = 10$ V, and $p = 3$ is depicted by the dashed line in Fig. 1. Some discrepancy between the experimental and theoretical curves is explained by certain methodological uncertainties related to the use of relationship (1).

The charge packet transfer inefficiency related to the presence of surface states in the semiconductor at the boundary with the dielectric decreases with increasing clock frequency. Figure 2 shows the experimental plots of ε_{ss} versus f for various densities of the surface states. The decrease in the charge transfer inefficiency is explained by the fact that an increase in f leads to a decrease in the relative concentration of active traps. The shapes of the experimental curves in Fig. 2 indicates that the higher the N_{ss} value, the greater the rate of ε_{ss} decrease with increasing clock frequency; above 10^7 Hz, the variation of ε_{ss} is very weak.

At still higher frequencies, only charging processes related to the presence of monoenergetic levels in the near-surface region of the semiconductor are significant. For these, the frequency factor can take a value above 10^7 Hz (and may even reach 10^{12} Hz [5]). Figure 3 shows the experimental curves of ε_{ss} versus f for various values of the effective frequency factor ω_e (the order of kinetics m in all cases is close to unity). As can be seen from these data, an increase in f in the microwave range is accompanied by a certain increase in ε_{ss} (due to the monoenergetic levels with $\omega_e > 10^7$ Hz), which detrimentally affects the CCD performance. For smaller ω_e values, a growth in the charge transfer inefficiency takes place at lower frequencies and vice versa. This is explained by the fact that a part of the trapped charge cannot leave traps during the charge transfer pulse action. The higher the clock frequency, the lower the probability of charge emission from the traps. This is manifested by an increase in ε_{ss}.

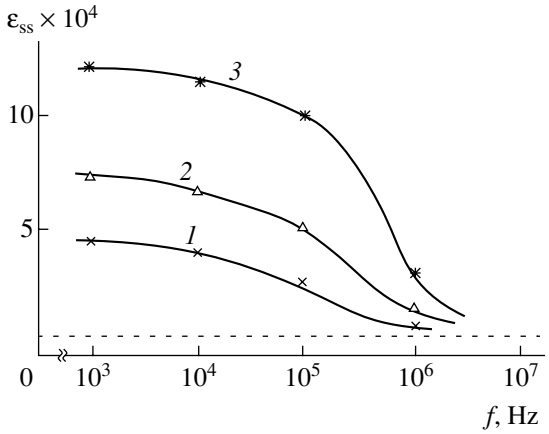

Fig. 2. Experimental curves of the charge transfer inefficiency ε_{ss} related to the surface states at the dielectric–semiconductor interface versus clock frequency f for $N_{ss} = 5 \times 10^{10}$ (*1*), 8×10^{10} (*2*), and 3×10^{11} eV^{-1} cm^{-2} (*3*).

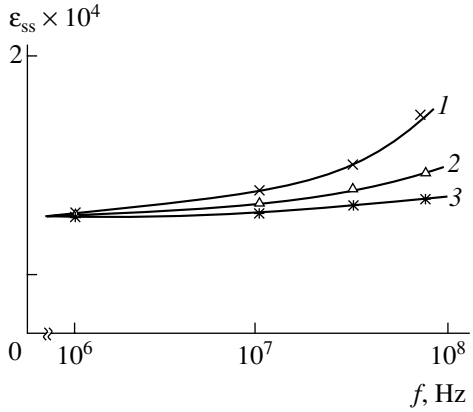

Fig. 3. Experimental curves of the charge transfer inefficiency ε_{ss} related to the surface states at the dielectric–semiconductor interface versus clock frequency f for various values of the effective frequency factor $\omega_e = 10^8$ (*1*), 10^9 (*2*), and 10^{10} s^{-1} (*3*).

The character of the experimental curves is well consistent with the empirical relationships derived using the following considerations. Let the charge packet transfer inefficiency be determined by the ratio of the residual trapped charge to the total charge in the packet. The maximum of the thermostimulated depo-

larization (TSD) current $I(T)$ for a given monoenergetic level at $m = 1$ is given by the expression [5]

$$I(T) = -(q\omega_e r^2/2L_0)(1 - r/L_0)n_{t0} \times \exp\left[-E_t/kT - \int_{T_0}^{T}(\omega_e/\beta)\exp(-E_t/kT')dT'\right], \quad (2)$$

where r is the thickness of the space charge localization region; L_0 is the sample thickness; n_{t0} s the initial concentration of charge carriers localized on traps; β is the sample heating rate; E_t is the activation energy of the monoenergetic level; T_0 and T are the initial and current temperatures, respectively; and T' is the integration parameter.

Using formula (2) and taking into account the number of charge packet transfers, the charge transfer inefficiency can be determined as follows:

$$\varepsilon_{ss} \approx n\left[kT_m\int_{T_0}^{T_k} I(T)/\beta dt\right] \Big/ \{E_t C_d V_g \exp[1 - \ln(f/\omega_e)]\},$$

where T_m and T_k are the temperature positions of the TSD current peak maximum and end; E_t is the activation energy of traps on the given monoenergetic level.

The frequency characteristics were determined for CCDs based on the heterostructures possessing a maximum effective frequency factor of $\omega_e = 10^{10}$ s^{-1}, which is by no means a limiting value. Therefore, an increase in ω_e will probably further expand the CCD frequency range. When the clock frequency increases above the ω_e value, we may expect a decrease in the activity of traps related to the given monoenergetic level.

As can be seen from the obtained frequency dependences of the characteristics determining the charged state of the heterostructures and the related CCDs, the influence of the surface states is significant up to a frequency on the order of a few megahertz. At still higher frequencies, the role of these states is negligibly small. In the microwave range, the frequency properties of CCDs are influenced only by the presence of monoenergetic levels. CCD operation deteriorates because of the monoenergetic levels possessing smaller effective frequency factors ω_e. At the same time, the presence of levels with higher ω_e values may produce virtually no effect on CCD operation. It should be noted that CCD performance at a higher charge transfer frequency increases with the decreasing order of kinetics, that is, with less pronounced retrapping of the charge carriers.

The above results indicate that CCDs poorly operating at lower frequencies may offer high performance in the microwave range. This circumstance is especially important for creating CCDs intended for the operation in volume integrated circuits for the SHF/EHF range [3].

REFERENCES

1. *Charge-Coupled Devices*, Ed. by D. Barbe (Springer-Verlag, Berlin, 1980; Mir, Moscow, 1982).
2. S. Sze, *Physics of Semiconductor Devices* (Wiley, New York, 1981; Mir, Moscow, 1984).
3. V. I. Gvozdev and E. I. Nefedov, *3-dimensional Integral Microwave Circuits* (Nauka, Moscow, 1985).
4. V. A. Neganov, S. B. Raevskiĭ, and G. P. Yarovoĭ, *Linear Macroscopic Electrodynamics*, Ed. by V. A. Neganov (Radio i Svyaz', Moscow, 2000), Vol. 1.
5. Yu. A. Gorokhovatskiĭ and G. A. Bordovskiĭ, *Thermoactivated Current Spectroscopy of High-Resistance Semiconductors and Dielectrics* (Nauka, Moscow, 1991).

Translated by P. Pozdeev

Technical Physics Letters, Vol. 28, No. 2, 2002, pp. 99–101. Translated from Pis'ma v Zhurnal Tekhnicheskoĭ Fiziki, Vol. 28, No. 3, 2002, pp. 36–41.

Charge Carrier Generation in a KBr Crystal under the Action of a Pulsed Sub-Breakdown Electric Field

V. D. Kulikov

Tomsk Polytechnical University, Tomsk, Russia

e-mail: kulikov@list2.epd.tpu.edu.ru

Received September 11, 2001

Abstract—Free charge carrier production in an ionic crystal (KBr) under the action of an external pulsed electric field with a strength of ~4.6×10^4 V/cm is studied. Under these conditions, the color centers (*F*-centers) appear at the positively charged electrode. It is suggested that the free electrons are produced due to the Auger transition cascades in the valence band of the dielectric crystal. © *2002 MAIK "Nauka/Interperiodica".*

The phenomenon of *F*-center production in KBr crystals was studied in samples exposed to a pulsed sub-breakdown electric field. The experiments were performed with KBr single crystals grown from a melt of special-purity grade salt. A strong electric field was induced by a pulsed beam of accelerated electrons possessing a maximum energy of ~0.3 MeV, a full width at half-maximum of $t_i \sim 18$ ns, and a beam current density of $J \sim 100$ A/cm^2, which served simultaneously as the source of X-ray radiation. The X-ray radiation was generated in a 1-mm-thick Al target with a diameter of 17 mm. A crystal sample was situated between the Al plate and a grounded electrode to form a capacitor in which a negative charge was accumulated in the bottom Al electrode and an induced positive charge in the top electrode. In order to eliminate the charge leak, the Al disk was mounted in an insulating support. The sample assembly was irradiated in vacuum (0.13 Pa) at room temperature.

The electric field strength in a dielectric crystal was determined using a method based on the linear electrooptical effect. The electrooptical crystal was represented by a high-resistivity cubic ZnSe crystal plate with a thickness of $d_1 = 6$ mm and a cross section of 10×15 mm [1]. The setup had a threshold sensitivity of ~2×10^3 V/cm and a time resolution of ~3 ns. The maximum field strength E_1 in ZnSe varied rather slightly with the beam current density (from 1.8×10^4 V/cm for $J = 1.4$ A/cm^2 to 2.3×10^4 V/cm for $J = 100$ A/cm^2), while the leading front steepness of the field pulse significantly increased. A maximum rate of the field strength buildup, ~10^{13} V/(cm s), was observed for $J =$ 100 A/cm^2. Figure 1a shows the typical kinetics of the

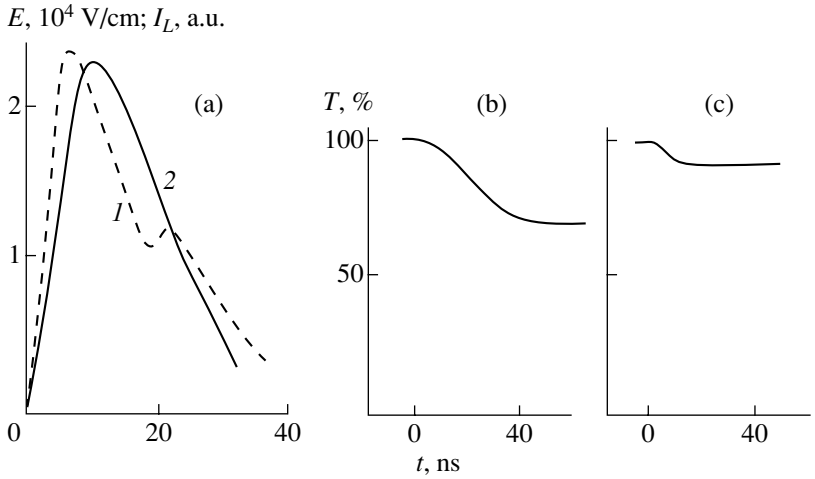

Fig. 1. (a) Typical kinetics of (*1*) the electric field strength E and (*2*) the X-ray-induced luminescence I_L in a ZnSe crystal; (b, c) oscillograms of the optical transmission at a wavelength of 0.63 μm in an X-ray-irradiated KBr crystal (b) on the negative electrode side in the absence of an electric field and (c) on the positive electrode side in the presence of the field. Electron beam current density ~100 A/cm^2.

1063-7850/02/2802-0099$22.00

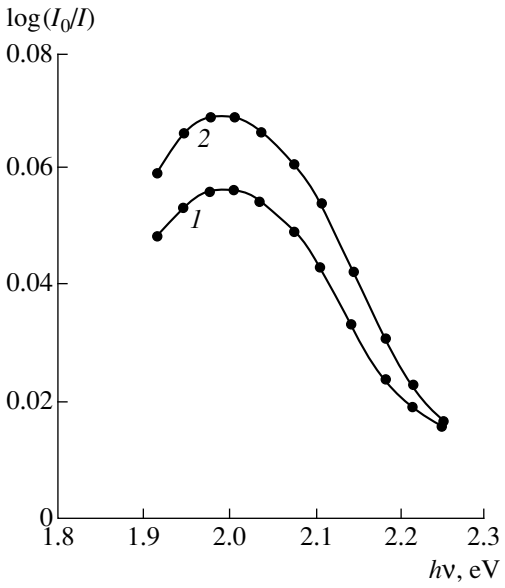

Fig. 2. Optical absorption spectra of the *F*-centers in a KBr crystal observed (*1*) in the absence and (*2*) in the presence of an induced electric field.

electric field strength E (curve *1*) and the X-ray-induced luminescence I_L (curve *2*) in the ZnSe crystal.

In the quasistationary approximation, a relationship between the charge Q accumulated in the capacitor electrodes and the beam current density can be described as $Q = J\tau$, where $\tau = RC$ is the charge relaxation time, R is the leak current, $C = \varepsilon\varepsilon_0 s/d_2$ is the capacitance of a sample assembly with electrodes, s is the electrode area, d_2 is the KBr sample thickness, and $\varepsilon\varepsilon_0$ is the absolute permittivity. The quasistationary approximation is valid under the condition $t_i > \tau$, which is satisfied in the experiment. Taking into account that $Q = \varepsilon\varepsilon_0 E$, the average volume field strength E_2 in the crystal studied can be evaluated as $E_2 = E_1 d_1/d_2$.

An incomplete breakdown (with a breakdown channel length below the sample thickness) was observed in KBr crystals with $d_2 \sim 2$ mm, which corresponded to a field strength of $E_2 \sim 6.9 \times 10^4$ V/cm.

In order to provide for a sub-breakdown regime, the optical absorption of the field-induced color centers was studied in a KBr plate with a thickness of $d_2 \sim 3$ mm (for $E_2 = 4.6 \times 10^4$ V/cm). Under these conditions, no incomplete breakdown channels were observed in the samples. The electric field effect on the *F*-center absorption band (*F*-band) was determined in two regimes: (i) in the absence of the field, whereby the Al electrode was grounded, and (ii) with the applied field. In both cases, the X-ray radiation intensity was determined by the accelerated electron beam current density (with a scatter between pulses not exceeding 5–7%).

The optical absorption due to the *F*-centers formed in the sample volume was probed by a He-Ne laser. In the absence of the field, almost no absorption in the *F*-band was observed at the positive electrode; the region of maximum absorption was situated near the negative electrode (Fig. 1b). In contrast, the maximum electric-field-induced absorption was observed near the edge of the positively charged top electrode, amounting to $\log(I_0/I) \approx 0.033$ at a depth of 0.5–0.7 mm from the upper face of the sample (Fig. 1c). A comparison of the initial stages of the kinetics (cf. Figs. 1b and 1c) shows that the optical absorption intensity under X-ray irradiation increases during the whole pulse, whereas in the presence of an applied electric field, the growth in the *F*-center concentration is restricted to a time period of ~10 ns. The time constants of relaxation of the induced absorption in the two cases are close.

The absorption spectrum of *F*-centers was also studied in the KBr samples probed with light over the whole volume. Figure 2 shows the relative absorption spectra measured at the instant of the pulsed electron beam action in the absence (curve *1*) and in the presence of the field (curve *2*). As can be seen, application of the electric field with a strength of $\sim 4.6 \times 10^4$ V/cm increases the absorption intensity by a factor of 1.22. The absorption band peaked at 1.98 eV agrees in both spectral position and halfwidth with the published data on the optical absorption of *F*-centers in KBr [2]. No changes in the optical absorption outside the *F*-band were observed. The total concentration of the X-ray-radiation-induced *F*-centers calculated using the optical absorption data by the Smakula formula was $\sim 10^{14}$ cm^{-3}, and that in the vicinity of the positive electrode was $n_F \approx 2 \times 10^{13}$ cm^{-3}.

The main mechanism of the *F*-center production in alkali-halide crystals is via the nonradiative decay of localized excitons. The excitons are generated when free conduction electrons are trapped in the free states of localized holes [3]. Therefore, the observed effect of *F*-center production is most probably related to the electric-field-induced electron–hole pairs.

Taking into account the above results and considerations, the process of the free carrier production in the electric field has the following specific features:

(i) A high electric field strength: $E > 10^5$ V/cm. This is indicated by the region of intense carrier production being close to the electrode edges and by a carrier production time limited by the width of the field strength maximum (Fig. 1a).

(ii) A relatively high average carrier concentration: $n_F \eta^{-1} \approx 2 \times 10^{14}$ cm^{-3}, where $\eta = 0.093$ is the yield of *F*-centers per electron–hole pair in KBr [2]. This electron concentration can provide for a current density of ~ 1.6 A/cm^2 for $E = 10^4$ V/cm.

(iii) A rather short characteristic time of the carrier production process: $<10^{-9}$ s. As can be seen from Fig. 1c, the *F*-centers are formed within a time period shorter than the field pulse width (3×10^{-8} s). Some estimates can be obtained by considering the charge

carrier production as an initial stage of the breakdown channel formation. It was reported [4] that the onset of the optical emission from discharge plasma in the breakdown channel coincides (to within the experimental time resolution) with the moment of field application. In [5], the breakdown channel with a length of ~9.5 cm was obtained in a KCl sample upon application of a voltage pulse with a duration of ~5 ns.

The appearance of free charge carriers in the conduction band of a dielectric can be related to the Zener effect, the carrier generation by impact [6]. Probably, the electron–hole pairs are formed by mechanism of the Auger transition cascades in the valence band of the dielectric crystal, with the electrons excited to the conduction band [7]. This mechanism can account for the anodic and crystallographic orientation of the breakdown development. According to [7], the energy band bending over the interatomic distance must be not less than the bandgap width, which corresponds to $E \sim 10^8$ V/cm. A high rate of the field strength buildup excludes a shunting effect of the surface currents, so that the field strength near the electrode edges can be significantly greater than the average field value in the bulk. This is confirmed by the data reported in [5], where breakdown in the KCl and NaCl samples was observed for a voltage of 2.5×10^5 V at a voltage growth rate of $\sim 10^{15}$ V/s, while the average field strength did not exceed $(2.6–3.8) \times 10^4$ V/cm.

Thus, the pulsed electric field with a strength of $\sim 5 \times 10^4$ V/cm and a leading front steepness of $\sim 10^{13}$ V/(cm s) produces *F*-centers in KBr crystals. *F*-center formation in a sub-breakdown electric field is indicative of the existence of an effective mechanism of primary electron production. These electrons are necessary for the impact ionization process involved in the breakdown of solid dielectrics.

REFERENCES

1. V. D. Kulikov, Izv. Vyssh. Uchebn. Zaved., Fiz., No. 5, 26 (1995).
2. V. M. Lisitsyn, V. I. Korepanov, and V. Yu. Yakovlev, Izv. Vyssh. Uchebn. Zaved., Fiz., No. 11, 5 (1996).
3. R. T. Williams, J. N. Bredford, and W. L. Faust, Phys. Rev. B **18** (12), 7038 (1978).
4. V. M. Lisitsyn and V. I. Oleshko, Pis'ma Zh. Tekh. Fiz. **9** (1), 15 (1983) [Sov. Tech. Phys. Lett. **9**, 6 (1983)].
5. A. L. Mironov, A. I. Zubarev, V. G. Shpak, and V. V. Bykov, Zh. Tekh. Fiz. **60** (11), 203 (1990) [Sov. Phys. Tech. Phys. **35**, 1354 (1990)].
6. G. I. Skanavi, *Physics of Dielectrics (Strong Field Region)* (Fizmatgiz, Moscow, 1958).
7. V. D. Kulikov, Pis'ma Zh. Tekh. Fiz. **26** (4), 77 (2000) [Tech. Phys. Lett. **26**, 170 (2000)].

Translated by P. Pozdeev